

AD-A149 805

STRESS CORROSION CRACKING AND OXIDATION CHARACTERISTICS
OF BORIDE-STRENGTH (U) OHIO STATE UNIV RESEARCH
FOUNDATION COLUMBUS C MOBLEY ET AL. 22 OCT 84

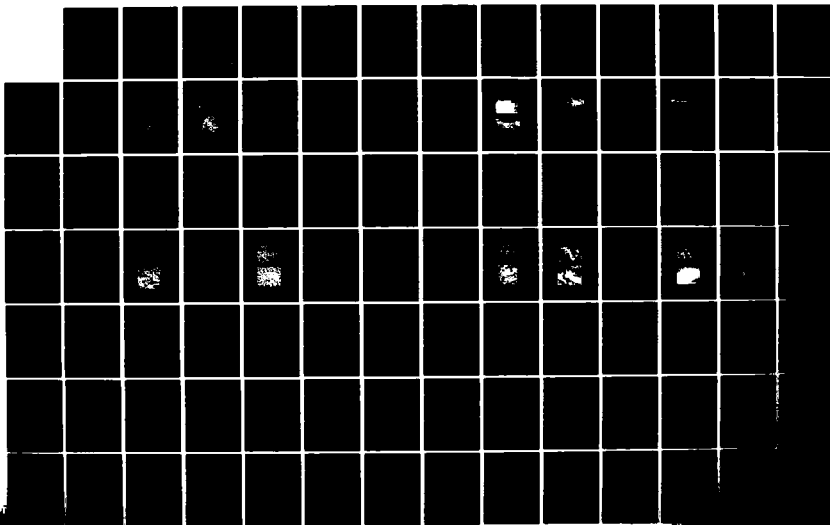
14

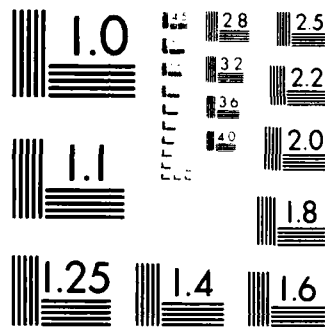
UNCLASSIFIED

OSURF-TR-2 N00014-82-K-0485

F/G 11/6

NL





MICROCOPY RESOLUTION TEST CHART
NATIONAL BUREAU OF STANDARDS-1963-A

AD-A149 805

12

RF Project 763166/714640
Annual Report

STRESS CORROSION CRACKING AND OXIDATION CHARACTERISTICS OF
BORIDE-STRENGTHENED MICROCRYSTALLINE IRON AND NICKEL BASED ALLOYS

C. Mobley, R. Hoagland, S. Smialowska, R. Rapp,
M. Straszheim, S. Wade, T. Chen, and H.G. Park

Department of Metallurgical Engineering

For the Period
July 1, 1983 - June 30, 1984

OFFICE OF NAVAL RESEARCH
Materials Division
Arlington, Virginia 22217

Contract No. N00014-82-K-0485

DTIC
ELECTE
JAN 24 1985
B

DISTRIBUTION STATEMENT A
Approved for public release;
Distribution Unlimited

October 22, 1984

OSU

**The Ohio State University
Research Foundation**

1314 Kinnear Road
Columbus, Ohio 43212

85 01 14 006

Technical Report Number 2
Contract N00014-82-K-0485
NR-653-014/4-13-82 (430)

STRESS CORROSION CRACKING AND OXIDATION CHARACTERISTICS OF
BORIDE-STRENGTHENED MICROCRYSTALLINE IRON AND NICKEL BASED ALLOYS

C. Mobley, R. Hoagland, S. Smialowska, R. Rapp,
M. Straszheim, S. Wade, T. Chen, and H.G. Park

Department of Metallurgical Engineering
The Ohio State University
Columbus, Ohio 43210

October 22, 1984

Annual Report for Period Two (July 1, 1983 to June 30, 1984)

Office of Naval Research
Materials Division
800 North Quincy Street
Arlington, Va. 22217

DTIC
ELECTE
JAN 24 1985
S B

DISTRIBUTION STATEMENT A

Approved for public release;
Distribution Unlimited

Unclassified

SECURITY CLASSIFICATION OF THIS PAGE

REPORT DOCUMENTATION PAGE

1a. REPORT SECURITY CLASSIFICATION NA		1b. RESTRICTIVE MARKINGS None	
2a. SECURITY CLASSIFICATION AUTHORITY NA		3. DISTRIBUTION/AVAILABILITY OF REPORT Approved for public release; distribution unlimited.	
2b. DECLASSIFICATION/DOWNGRADING SCHEDULE			
4. PERFORMING ORGANIZATION REPORT NUMBER(S) 714640/763166 763166/714640		5. MONITORING ORGANIZATION REPORT NUMBER(S)	
6a. NAME OF PERFORMING ORGANIZATION The Ohio State University	6b. OFFICE SYMBOL (If applicable)	7a. NAME OF MONITORING ORGANIZATION Office of Naval Research	
6c. ADDRESS (City, State and ZIP Code) Research Foundation 1314 Kinnear Road Columbus, Ohio 43212		7b. ADDRESS (City, State and ZIP Code) Code 612A:RAC 800 North Quincy Street Arlington, Virginia 22217	
8a. NAME OF FUNDING/SPONSORING ORGANIZATION Office of Naval Research	8b. OFFICE SYMBOL (If applicable) ONR	9. PROCUREMENT INSTRUMENT IDENTIFICATION NUMBER N00014-82-K-0485	
8c. ADDRESS (City, State and ZIP Code) Code 612A:RAC 800 North Quincy Street Arlington, Virginia 22217		10. SOURCE OF FUNDING NOS.	
11. TITLE (Include Security Classification) *		PROGRAM ELEMENT NO.	PROJECT NO. NR 653-014/ 4-13-82 (430)
		TASK NO.	WORK UNIT NO.
12. PERSONAL AUTHOR(S) C. Mobley, R. Hoagland, S. Smialowska, R. Rapp, M. Straszheim, S. Wade, T. Chen, and H. G. Park - Department of Metallurgical Engineering			
13a. TYPE OF REPORT Annual	13b. TIME COVERED FROM 7/1/83 TO 6/30/84	14. DATE OF REPORT (Yr., Mo., Day) October 22, 1984	15. PAGE COUNT 108
16. SUPPLEMENTARY NOTATION			
17. COSATI CODES		18. SUBJECT TERMS (Continue on reverse if necessary and identify by block number)	
FIELD	GROUP	SUB. GR.	
		microcrystalline, iron-based alloys, nickel-based alloys, mechanical properties, fracture toughness, oxidation.	
19. ABSTRACT (Continue on reverse if necessary and identify by block number) *STRESS CORROSION CRACKING AND OXIDATION CHARACTERISTICS OF BORIDE-STRENGTHENED MICROCRYSTALLINE IRON AND NICKEL BASED ALLOYS This report summarizes the microstructures, room and elevated temperature mechanical properties, fracture toughness, oxidation, general corrosion and stress corrosion cracking characteristics of two iron-based and two nickel-based microcrystalline alloys. These microcrystalline alloys appear suitable for a number of intermediate temperature (i.e., 500 to 800 C) applications.			
20. DISTRIBUTION/AVAILABILITY OF ABSTRACT UNCLASSIFIED/UNLIMITED <input type="checkbox"/> SAME AS RPT <input checked="" type="checkbox"/> DTIC USERS <input type="checkbox"/>		21. ABSTRACT SECURITY CLASSIFICATION Unclassified	
22a. NAME OF RESPONSIBLE INDIVIDUAL	22b. TELEPHONE NUMBER (Include Area Code)	22c. OFFICE SYMBOL	

TABLE OF CONTENTS

	<u>Page</u>
I. INTRODUCTION AND BACKGROUND	1
II. ALLOYS IDENTIFICATION AND STRUCTURE	2
III. MECHANICAL PROPERTY CHARACTERIZATIONS	19
IV. OXIDATION CHARACTERISTICS	32
V. CORROSION CHARACTERIZATION.	59
VI. SUMMARY AND FUTURE WORK	103
VII. REFERENCES.	104

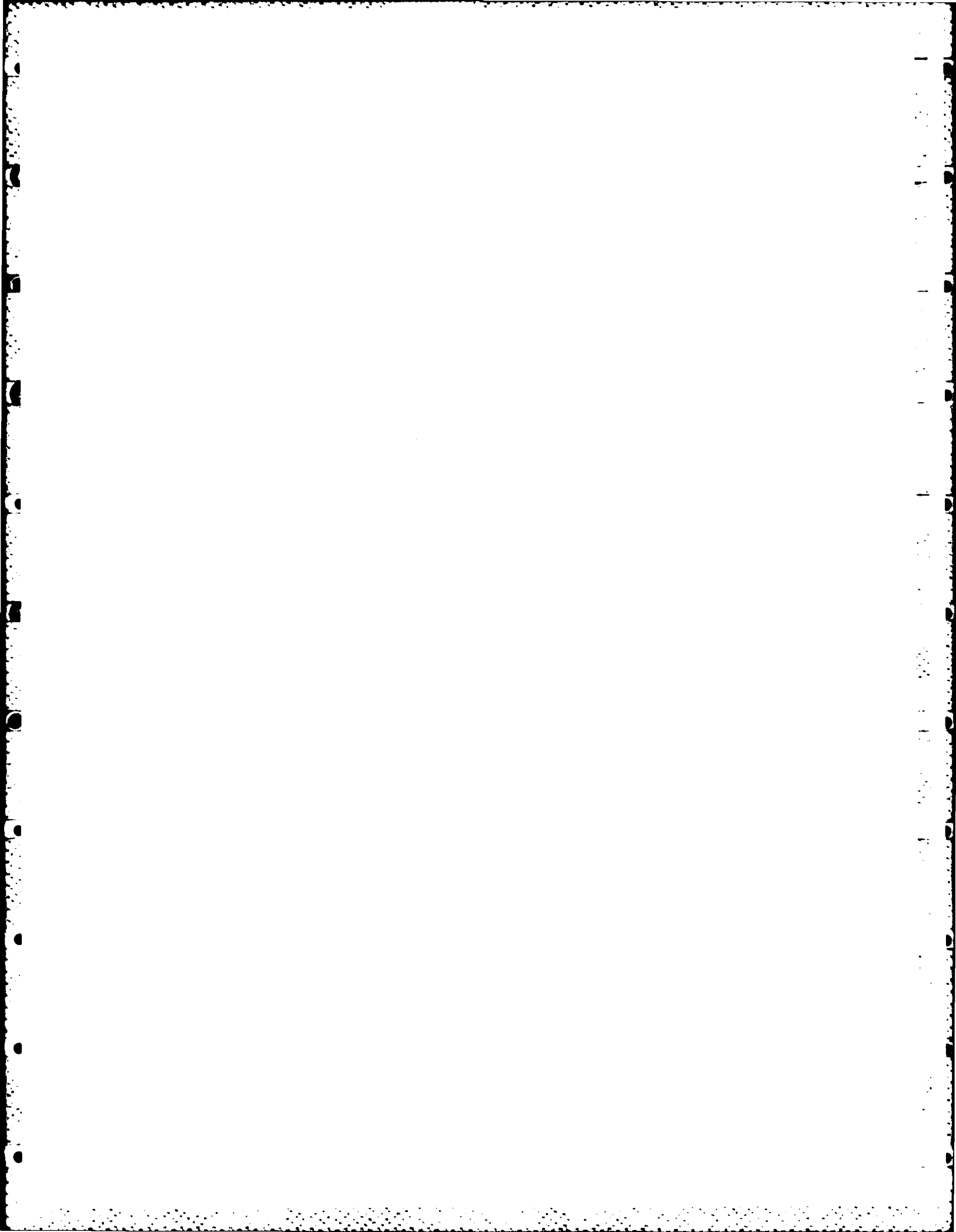
Accession For	
NTIS GRA&I	<input checked="" type="checkbox"/>
DTIC TAB	<input type="checkbox"/>
Unannounced	<input type="checkbox"/>
Justification	
PER CALL JC	
By	
Distribution/	
Availability Codes	
Dist	Avail and/or Special
A-1	



PREFACE

This is the second annual report prepared on Contract Number N00014-82-K-0485, NR-653-014/4-13-82 (430) covering the period of work from July 1, 1983 to June 30, 1984. The program is sponsored by the Department of the Navy, Office of Naval Research. Dr. Donald Polk is the ONR Technical Representative monitoring the program and Morris S. Soloman is the Contracting Officer.

Dr. Carroll Mobley is the Principal Investigator on this study with major research inputs from Drs. Robert Rapp (high temperature oxidation), Richard Hoagland (fracture characteristics and stress corrosion cracking) and Susan Smialowska (corrosion). The Graduate Research Assistants on this program were Mark Straszheim (oxidation), Scott Wade (mechanical properties and fracture characteristics) Hyun-Gyoon Park (mechanical properties and stress-corrosion cracking) and Liberty Chen (corrosion properties). The program is administered and monitored by the Ohio State University Research Foundation and is identified as OSURF Project Number 714640. Dr. Tom Miller was the OSURF Development Officer and Mr. Les Stout is the Principal Administrator on this program.



I. INTRODUCTION AND BACKGROUND

A number of laboratory and pilot plant studies have demonstrated that alloys produced by rapid solidification processes exhibit improved corrosion resistance and mechanical properties relative to their conventionally-processed equivalents^{(1-4)*}. Improvements in corrosion resistance and mechanical properties are generally attributed to one or more of the following characteristics of the rapidly quenched materials: (a) small cell or grain size microstructures, (b) extended solid solubility limits, and (c) the occurrence of metastable (including the amorphous) phases. The chemical homogeneity of the rapidly quenched materials and the ability to control their microstructural features through subsequent thermomechanical treatments make this class of alloy attractive for many applications. One such relatively new class of alloys based upon the rapid solidification processes are the microcrystalline alloys. As described by Ray⁽⁴⁻⁶⁾, ultrafine grain size (0.2 to 0.3 μm) Fe, Ni, and/or Co-based alloys containing 0.1 to 0.2 μm size intermetallic phases, (such as borides), can be obtained by (i) producing glassy Fe, Ni, or Co-based alloy containing 5 to 14 atomic percent metalloid, such as B, via a rapid quench process, and (ii) devitrifying the glassy alloy (i.e., crystallizing it in the solid state) using controlled thermal or thermomechanical treatments.

Preliminary evaluations of the Fe, Ni, and Co-based microcrystalline alloys containing borides indicated that they offered good corrosion resistance and oxidation resistance coupled with good mechanical properties⁽²⁻⁴⁾. This research program was undertaken to provide a more complete characterization of the corrosion, oxidation, and fracture characteristics of four selected iron and nickel-based microcrystalline alloys which contained dispersed intermetallic borides.

* References are listed on page 104.

II. ALLOY IDENTIFICATION AND STRUCTURES

II-1. Compositions and Preparation

The four microcrystalline alloys of this study were prepared and supplied by Marko Materials, Inc.* The compositions of the alloys, as determined by optical emission spectrographic (OES) analysis, are given in Table 1. The alloy designations 1,2,3 or 4 for the four microcrystalline alloys will be used throughout this report. The compositions of five selected wrought alloys included for comparison are also given in Table 1.

As indicated in Table 1, the sum of the individual weight percentages of the alloying elements, as determined by OES, is between 95.48 and 99.96%. Failure to sum to 100% is attributed to lack of "equivalent alloy" standards with which to precalibrate the OES unit. The major error in the reported alloying element percentages is associated with the base element (i.e., nickel in alloys 1 and 2, and iron in alloys 3 and 4).

Each of the four microcrystalline alloys was processed in similar ways. Each alloy was induction melted and chill block melt spun to form amorphous ribbon. The ribbons were ball milled to produce -100 mesh powders. The resultant powders were placed in low-carbon steel cans which were hot extruded to produce the microcrystalline alloys in bar form. Alloys 1 and 4 were hot extruded at a temperature of 1120 C with an extrusion ratio of 20:1. As both alloys 1 and 4 exhibited microporosity and alloy 4 evidenced some grain growth during hot extrusion, alloys 2 and 3 were consolidated in a two step process. The canned alloys were first upset forged at a temperature of 975 C and then were hot extruded at a temperature of 1000 C with an extrusion ratio of 20:1. During hot extrusion, all these alloys were above their crystallization temperatures and devitrified to produce fully crystalline materials.

* Marko Materials, Inc., 144 Rangeway Road, North Billerica, Mass., 01862

TABLE 1: COMPOSITIONS OF ALLOYS TESTED, WEIGHT % (ATOM. %)

Alloy	Ni	Fe	Cr	Mo	B	Other*	Σ
1	45.40	5.56	26.71	16.41(10)	1.43(7.8)	--	95.51
2	48.70	4.70	17.37	23.61(15)	1.10(6.4)	--	95.48
3	16.61	57.37	19.71	5.04(3)	1.23(6.1)	--	99.96
4	5.43	48.16	28.74	11.22(7)	1.65(8.6)	--	95.20
316 S.S.	10-14	63-67	16-18	2-3	--	2Mn, 1Si	--
330 S.S.	34-37	41-45	17-20	--	--	2Mn, 1Si	--
333 S.S.	32.0	44-45	21.5	--	--	1Mn, .5Si	--
Hastelloy X	44-48	17-20	20-23	8-10	.01	1Mn, 1Si	--
Inconel 600	76.0	8.0	15.5	--	--	.3Cu, .5Ti	--

*Compositional limits for stainless steels: .045P, .03S; for Hastelloy X: .04P, .03S, 1.5Co, 1W.

Carbon contents are less than 0.1 wt% for all alloys.

II-2. Microstructures

The microstructures of alloys 1 through 4, in both the as-received and heat treated conditions, were characterized using optical metallographic techniques. As one of the goals of this program was to determine the stability of these alloys with respect to exposure to elevated temperatures, discs of the four alloys were heated to controlled temperatures between 900 and 1000 C for periods up to 20 hours in argon and then cooled to room temperature. Such heat treated (i.e., exposed to elevated temperatures) samples were examined to assess changes in the microstructure and hardness.

As all four of these microcrystalline alloys were relatively corrosion resistant, it was necessary to identify appropriate etchants to reveal the phase boundaries. Etchants which were used to prepare these alloys are listed in Table 2, with the best etchants and etching conditions for each alloy given in Table 3. Although the etchants given in Table 3 were the best found, some difficulties were still encountered in revealing the matrix phase boundaries.

Optical micrographs of all four microcrystalline alloys are shown in Figures 1 through 4. These are transverse and axial sections of the as-received extruded rods and only axial sections of the materials after heat treatment. All axial sections were taken near the ends of the extruded rods. The transverse sections were taken from the middle of the rods to check for microstructural variations along the length of the rod. Each alloy was multiphase with the size of the second phases increasing from alloy 1 to alloy 4. The phase sizes could not be determined from the optical micrographs of some alloys because either the microstructure was too fine to be resolved or the etchant did not reveal the boundaries. In those cases in which optical microscopy did not reveal the phase sizes, transmission electron microscopy (TEM) was used to determine the phase sizes. The measured phase sizes are

TABLE 2: ETCHANTS TRIED IN OPTICAL MICROSCOPY WORK ON MICROCRYSTALLINE ALLOYS.

A	5ML HNO_3 ; 95ML Methanol
B	20ML Acetic; 30 ML HNO_3
C	5GM FeCl_3 ; 75ML HCl ; 100ML H_2O
D	5 ML HNO_3 ; 1ML HF (48%) ; 44 ML H_2O
E	10GM Oxalic Acid ; 100 ML H_2O
F	20 ML HNO_3 ; 5ML HCl ; 20ML Ethanol
G	10 ML HNO_3 ; 20ML HCl ; 40ML Glycerin
H	'G' + 20ML H_2O_2 (30%)

TABLE 3: PREFERRED ETCHANT(S) FOR EACH MICROCRYSTALLINE ALLOY.

Alloy	Heat Treatment	Best Etchant
1	as received (A.R.)	A: 6 Volts, 5-10 sec. or C: immerse 3-5 min.
	1000 20 hours	same as above
2	A.R.	A: 6 Volts, 8-15 sec.
	1000 20 hours	same as above
3	A.R.	G: swab on 10-15 sec. or A: 6 Volts, 10-15 sec.
	1000 20 hours	same as above
4	A.R.	C: Immerse 30 sec. - 1 min.
	1000 20 hours	A: 6 Volts, 10-15 sec. or C: swab, 5-15 sec.

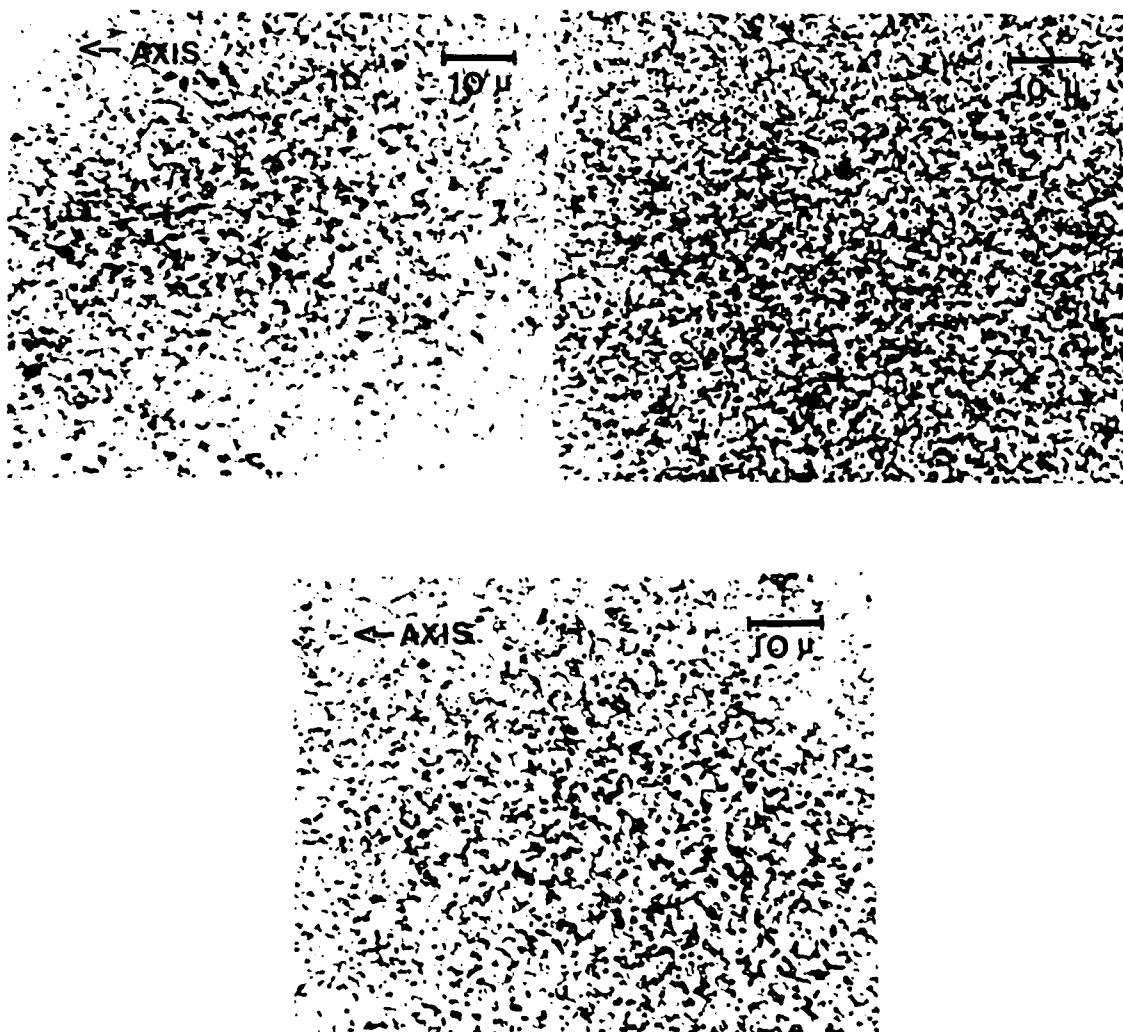


Figure 1: Axial (a) and transverse (b) sections of alloy 1 before heat treatment along with an axial section (c) after heat treatment at 1000°C for 20 hours. All photos at 1000X.



Figure 2: Axial (a) and transverse (b) sections of alloy 2 before heat treatment along with an axial section (c) after heat treatment at 1000°C for 20 hours. All photos at 1000X.

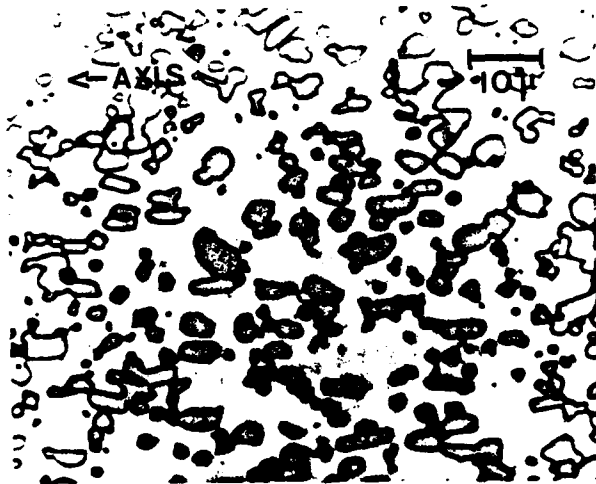
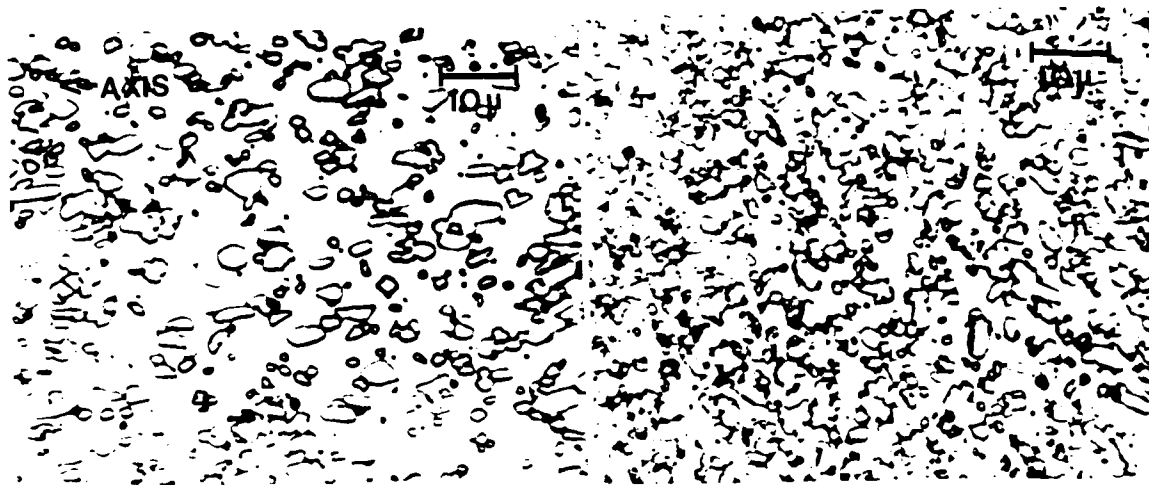


Figure 3: Axial (a) and transverse (b) sections of alloy 3 before heat treatment along with an axial section (c) after heat treatment for 1000°C for 20 hours. All photos at 1000X.

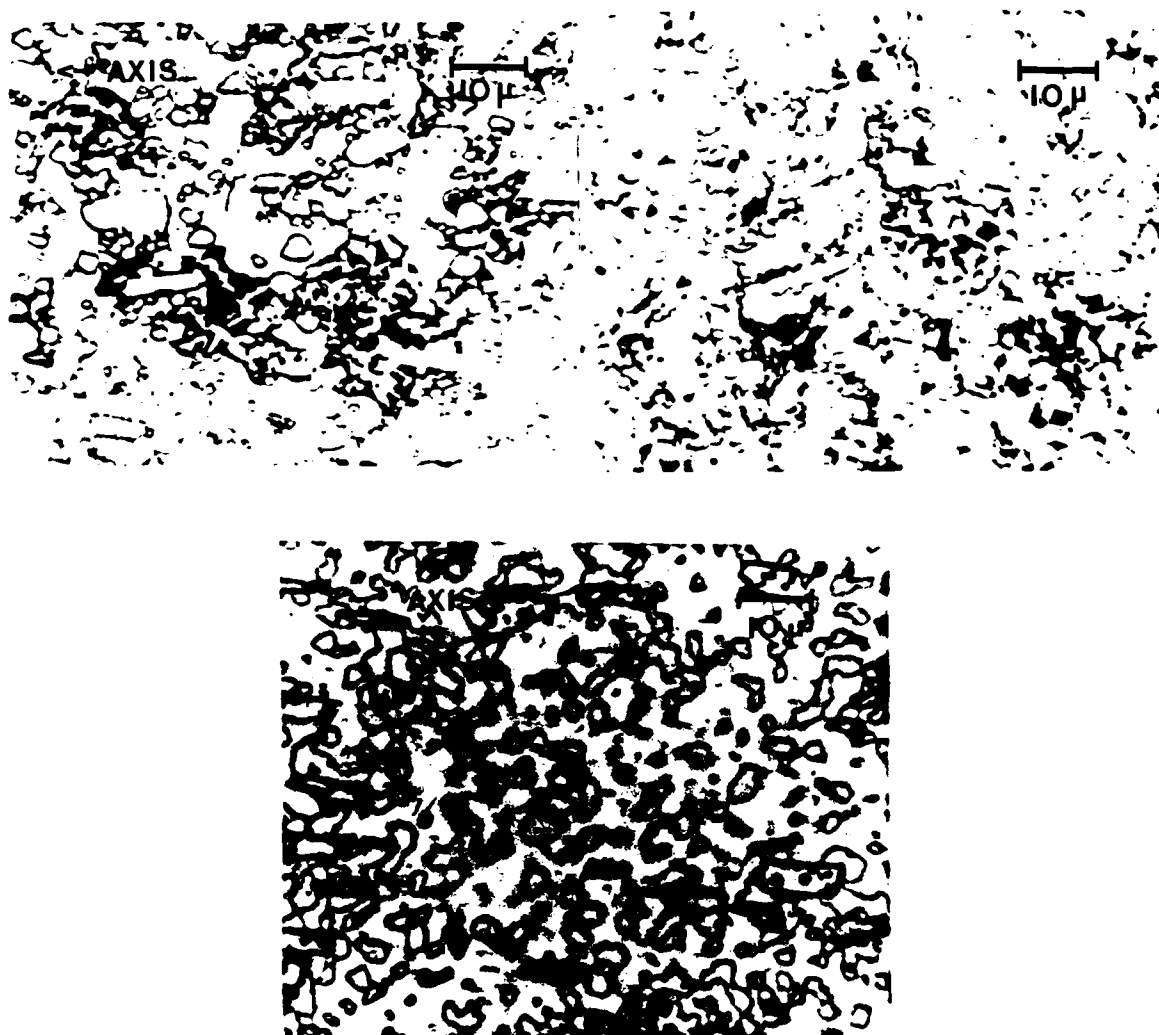


Figure 4: Axial (a) and transverse (b) sections of alloy 4 before heat treatment along with an axial section (c) after heat treatment at 1000°C for 20 hours. All photos at 1000X.

given in Table 4. Also, particle spacing and volume fraction calculations were done for particles with sizes greater than 1 μm and the results are given in Table 5. As can be seen from the Tables 4 and 5 alloys 1 and 2 have the smallest grain sizes with alloy 2 containing a small volume fraction of large (2-3 μm) second phase particles. Alloys 3 and 4 had coarser phase dimensions but were generally less than 8-10 μm .

Even though many of the grain boundaries in Figures 1 through 4 were not revealed by etching, there is evidence of texture or elongation of some of the phases present in the four alloys. Texture is important in terms of the anisotropy of the mechanical properties.

Examining the optical micrographs of alloy 1 shown in Figure 1, the microstructure in the as-received condition is found to consist of a very homogeneous light matrix material dispersed with dark second phases. X-ray diffraction of this alloy yielded peaks which matched the matrix to a f.c.c. Ni-Fe-Cr solid solution with MoB_4 present as a second phase. If all the B is assumed to be present as MoB_4 the theoretical volume fraction of MoB_4 is .23 which is close to that given in Table 5.

Some abnormalities were found to exist in the microstructure of alloy 1 as shown in Figures 5 and 6. Figure 5 shows some unknown composition stringers that were found in the microstructure. These stringers run parallel to the axis of the extruded rod and should therefore have little effect on mechanical testing due to their orientation in the specimens. Banding, is shown in Figure 6, also was evidenced in alloy 1. Observation of these bands in the Scanning Electron Microscope (SEM) indicated the presence of cavities between many of the bands. Measurements taken on the dimensions of the bands were found to match those that would be obtained after deforming 150 μm particles such as those used in production of the microcrystalline alloys. Using this

TABLE 4: PHASE SIZES THAT COULD BE DETERMINED FOR EACH MICROCRYSTALLINE ALLOY.

Alloy	heat treatment	grain size,um	particle sizes,um
1	as received	.3-1.0	.1 - 1.5
	1000 °C 20 hours	-	up to 2.5
2	as received	.3 - 2.0	.3 - 2.5
	1000 °C 20 hours	-	up to 4.0
3	as received	3.0-8.0	.3 - 9.0
	1000 °C 20 hours	3.0-10.0	.3 - 10.0
4	as received	-	up to 5
	1000 °C 20 hours	-	up to 7

TABLE 5: PARTICLE SPACINGS AND VOLUME FRACTION PHASES THAT COULD BE DETERMINED FOR EACH MICROCRYSTALLINE ALLOY.

Alloy	Heat Treatment	Particle Spacing	Volume Frac. Particles
1	As Received (A.R.)	—	—
	1000°C 20 hours	.96 μm	.275
2	A.R.	2.10 μm	.063
	1000°C 20 hours	1.95 μm	.096
3	A.R.	3.23 μm	.112
	1000°C 20 hours	3.00 μm	.133
4	A.R.	—	—
	1000°C 20 hours	—	—

information, plus the fact that all other sections taken of alloy 1 had microstructures similar to those in Figure 1, it was determined that the section shown in Figure 6 was taken from an end of the extruded rod where the amorphous powder did not consolidate well.

The microstructure of alloy 1 after heat treatment (Figure 1-c), exhibits larger second phase particles than in the as-received alloy. There are many particles with sizes greater than 1 μm and the particle spacing has also increased in the samples exposed to elevated temperatures.

The microstructure of the second-nickel based alloy (alloy 2) was found to be somewhat different than in alloy 1. There is a matrix of fine grained material dispersed with submicron particles as before, but there are also 2-3 μm dispersed second phases particles. X-ray diffraction analysis of alloy 2 indicated the presence of the same phases as matrix found in alloy 1. Therefore the microstructure of alloy 2 consists of a Ni-Fe-Cr solid solution dispersed with two different sizes of MoB_4 particles. There was little change in the alloy 2 microstructures with heat treatment as shown in Figure 2-c. The volume fraction of large particles increased by 3.6% while the particle spacing decreased by .15 μm .

Some centerline cracking, porosity and banding is also observed in alloy 2 samples, as shown in Figure 7. Some cracks found in alloy 2 were several millimeters wide and long. Porosity with pore sizes ranging up to 20 μm was also observed in the vicinity of the cracks. These two defects are often encountered in powder consolidated materials but the banding phenomenon is not. The bands were matrix materials devoid of dispersed second phase. Microhardness testing resulted in a value of Knoop 282 for the bands and Knoop 410 for the bulk. No explanation for the bands formation is known.

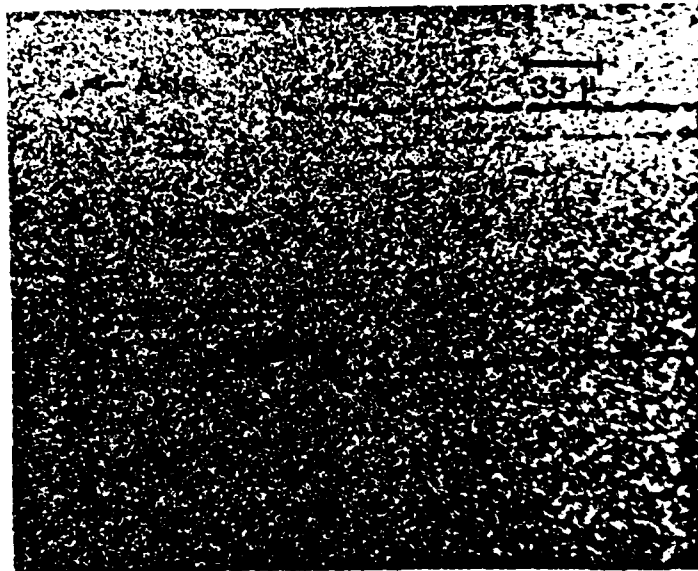


Figure 5: Stringers found in the matrix of alloy 1 (300X).



Figure 6: Banded microstructure found in alloy 1 (400X).

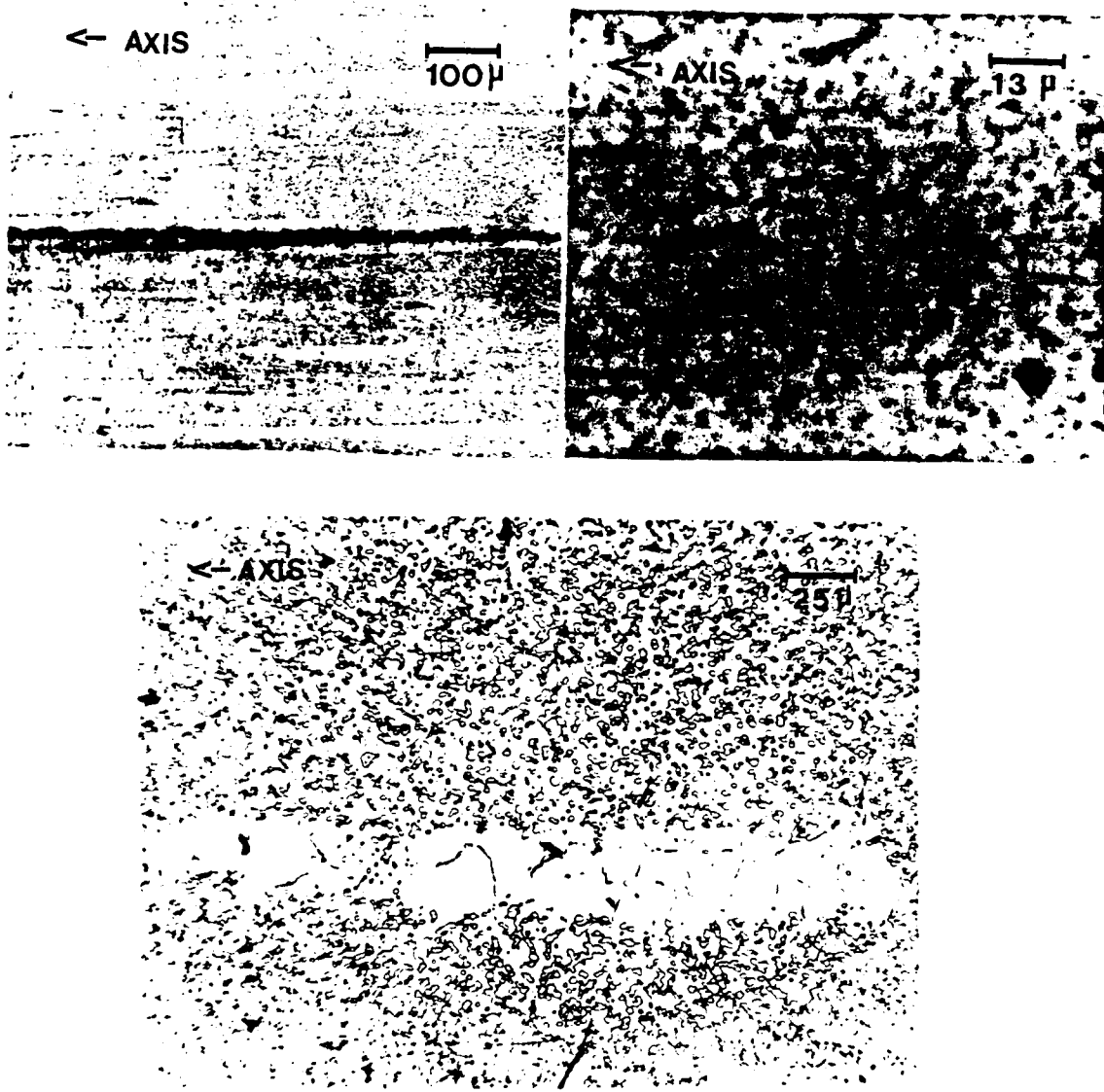


Figure 7: Centerline cracking (a), porosity (b) and banding (c) found in alloy 2.

The microstructure of alloy 3 was similar to that of alloy 2. Alloy 3 has a matrix phase dispersed with two size second phase particles. Many of the large particles ranged up to 10 μm , while the smaller particles were less than 1 μm in size. X-ray diffraction analysis of alloy 3 in the 'as-received' condition indicated the presence of three phases, a f.c.c. Fe-Cr-Ni solid solution matrix dispersed with MoB_4 and MoFe_2B_4 particles.

Heat treatment of alloy 3 produced only small changes in the microstructure. The volume fraction of large ($>1 \mu\text{m}$) second phase particles increased by 2.1% while their spacing decreased by .23 μm .

Regions of centerline cracking and porosity were also found in alloy 3. The cracks were not as large as those found in alloy 2 but were still large as shown in Figure 8-a. Figure 8-b shows some of the porosity present in the material. Many of these pores were 3-5 μm in diameter. Another characteristic feature observed in alloy 3 were large isolated particles 8 is shown in Figure 8-c. These particles, which ranged between 125 - 225 μm in size, were randomly dispersed throughout the matrix. They were apparently harder than the bulk material, as the bulk material has flowed around this particle during high temperature consolidation. The composition of these isolated particles were undetermined.

The microstructure of alloy 4 (See Figure 4) is quite different from the three preceding alloys. The matrix of the as-received alloy appeared to have a larger grain size (up to 10 μm) with rod and spherical-shaped second phase particles present along with dark areas that appeared to be a grain boundary precipitate. X-ray diffraction of this alloy indicated a b.c.c. Fe-Cr-Ni solid solution matrix containing CrB_2 and MoFe_2B_4 second phases. Many of the large particles appearing in Figure 4-a are actually conglomerates of many smaller grains (2-3 μm).

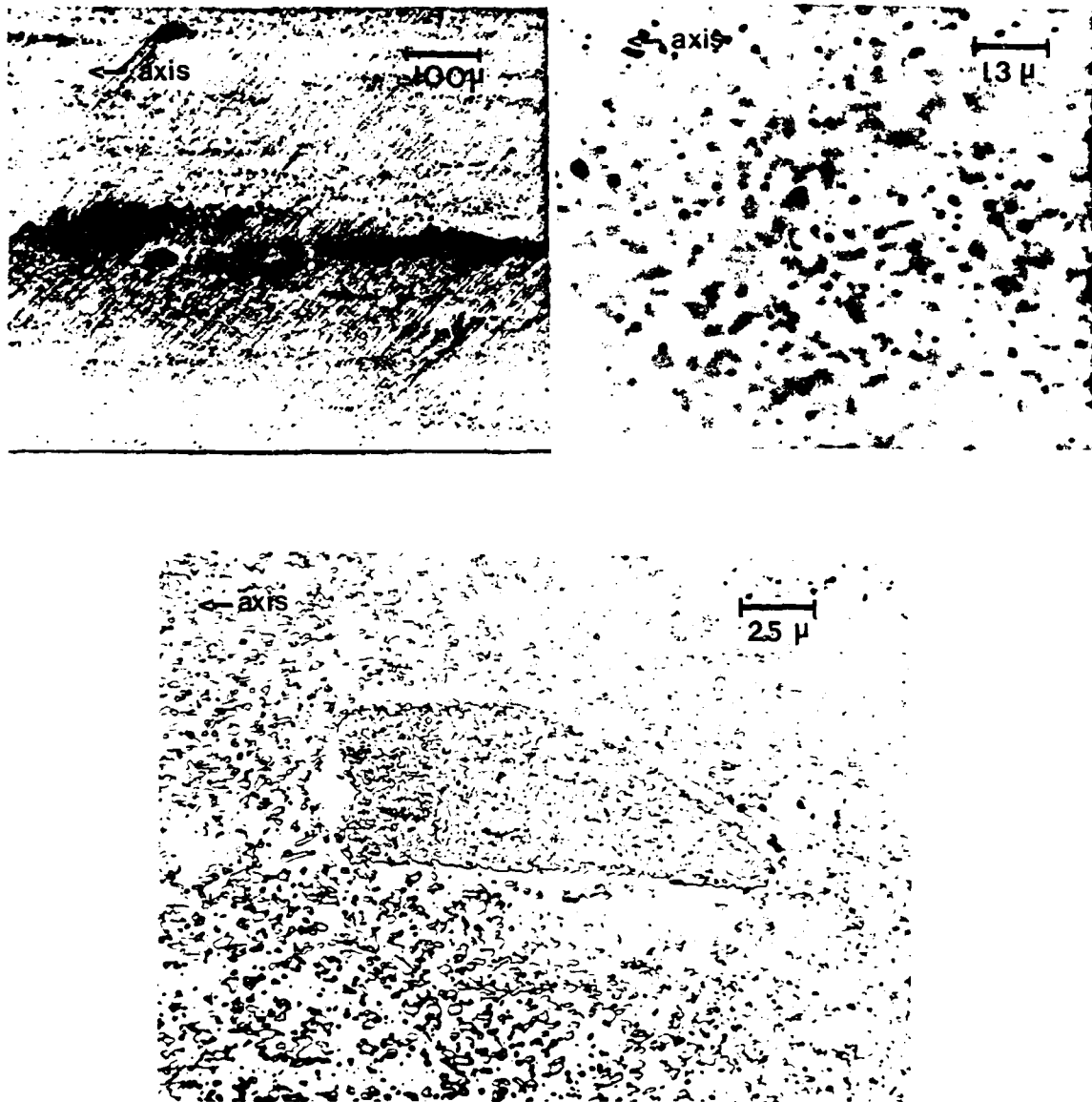


Figure 8: Centerline cracking (a), porosity (b) and large particles (c) found in alloy 3.

After heat treatment, the microstructure of alloy 4 changed drastically with a reorganization of all the phases present except the spherical particles. X-ray diffraction analysis of the heat treated alloy 4 indicated the precipitation of several different boride phases and a σ -phase within the b.c.c. solid solution matrix. As will be shown later, heat treatment of the alloy 4 material increases its hardness and makes it brittle.

Alloy 4 also contains some stringers and microporosity. Figure 9 shows example unknown composition stringers in the as-received alloy 4. It should be noted that alloys 1 and 4 were produced at the same time, while alloys 2 and 3 were produced at a significantly later date. Alloys 1 and 4 contain some stringers and a small amount of porosity, while alloys 2 and 3 contain no stringers but do exhibit centerline cracks and porosity.

III. MECHANICAL PROPERTY CHARACTERIZATIONS

III-1. Hardness Data

Hardness tests were performed on all four alloys in the as-received and heat treated conditions. The hardness data are given in Table 6. As indicated, there were no changes in the hardness of alloys 1 through 3 with the heat treatments, consistent with the constancy of the microstructures of these alloys before and after heat treatments. In contrast alloy 4, exhibits an increase of 20 points on the R_c scale after exposure to temperatures greater than 700°C. This is most likely due to the formation of σ -phase during heat treatment. Heat treated samples of alloy 4 were quenched and furnace cooled from the heat treatment temperature to room temperature to ascertain if the hardness increase was due to a cooling rate effect. However, both samples still had a hardness increase to R_c 60 indicating the quench rate during cooling was not the major factor causing the hardness increase. When heat treated at 500°C there was no hardness change for periods up to 10 hours.

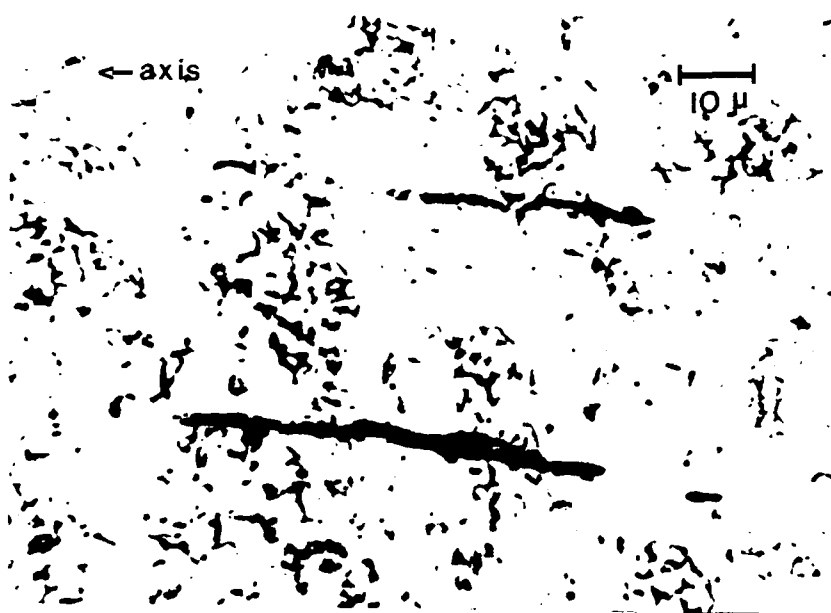


Figure 9: Stringers found in alloy 4 (1000X).

TABLE 6: HARDNESS DATA (R_C) OBTAINED FOR THE MICROCRYSTALLINE ALLOYS.

Alloy	As Received	500°C 10 hrs.	700°C 10 hrs.	900°C 10 hrs.	900°C 20 hrs.	1000°C 10 hrs.	1000°C 20 hrs.
1	40.7	—	—	41.1	41.3	42.2	39.9
2	35.7	—	—	37.0	37.6	36.4	36.6
3	23.4	—	—	21.2	23.3	20.8	21.5
4	39.0	43.4	63.6	60.2	61.4	61.1	59.1

III-2. Tensile Testing

Uniaxial tensile tests were performed on the as-received and heat treated microcrystalline materials. All four alloys were tested in the 'as-received' condition and alloys 1, 2 and 3 were also tested after heat treatments at 1000°C for ten and twenty hours.

Specimen dimensions of the tensile bars used are shown in Figure 10. Substandard dimension specimens were used so that four specimens could be machined per unit length of material whereas only one per unit length could have been machined with the typical 0.505 inch gage dimensions. Machining of the tensile specimens was done by Metcut Research Associates*.

Tensile testing was done on an Instron Machine using a 0.5 inch (1.27 cm) gage length extensometer to monitor the extension. The nominal crosshead speed used in most tests was .05 cm/min although strain rate sensitivity was checked by switching to a crosshead velocity of .005 cm/min at different times throughout the test. The measured data included a load elongation curve which was used to calculate yield strength, ultimate strength, modulus of elasticity, strain hardening exponent and strain rate sensitivity.

The measured tensile properties for the four microcrystalline alloys and four compositionally similar iron and nickel-based conventional alloys (i.e., Hastelloys C-276 and G, Inconel 625 and 304 stainless steel) are given in Table 7. As can be seen from the Table 7 data the room temperature strengths of alloys 1 and 2, the nickel-based microcrystalline alloys, were 2 to 3 times greater than the strengths of Hastelloy C-276 and G and Inconel 625. However, the ductilities exhibited by alloys 1 and 2 were much less than that of the

*Metcut Research Associates, Cincinnati, Ohio.

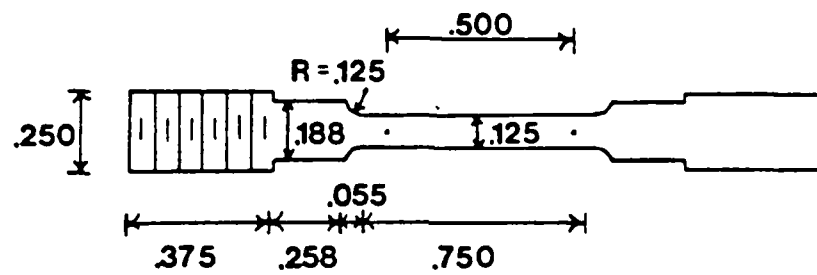


Figure 10: Tensile specimen dimensions.

TABLE 7: TENSILE PROPERTIES FOR THE MICROCRYSTALLINE ALLOYS AND SELECTED COMPARISON ALLOYS.

Alloy	Heat Treatment	E ($\times 10^6$ psi)	σ_y (ksi)	σ_u (ksi)	% Elong	n	m
1	As Received	33.8	116	196	9.0	.16	.004-.005
	1000°C-10 hrs.	32.5	132	220	12.6		
	1000°C-20 hrs.	33.6	133	220	9.0		
2	As Received	29.9	102	178	8.1	.21	.005-.006
	1000°C-10 hrs.	30.0	107	203	9.2		
	1000°C-20 hrs.	30.0	103	191	8.5		
3	As Received	24.2	68	122	18.0	.20	.007-.008
	1000°C-10 hrs.	25.0	63	135	18.4		
	1000°C-20 hrs.	25.5	70	136	14.4		
4	As Received	30.9	159	190	1.2	+	+
Hast. C-276	Sol'n treat at 1120°C	29.8	52	115	61		
Incon 625	—	30	71	124	50		
Hast. G	Sol'n treat at 1100°C	28.0	46	102	61		
304 S.S.	—	28.0	32	80	35		

+ could not be determined

comparison nickel-based alloys listed. Even though the ductility was much lower in the microcrystalline alloys, the failure elongation, was about 10% which indicates moderate ductility.

Heat treatments of the two nickel-based microcrystalline alloys produced only small changes in their tensile properties. Alloy 1 had about a 10% increase in strength while maintaining its ductility. Alloy 2 exhibited only slight changes in strength and little or no change in ductility.

Alloy 3, the face centered cubic iron-base alloy, had room temperature strength levels approximately equal to 304 stainless steel, but its ductility was also lower than that of the 304 stainless steel. This lesser ductility could be due to the presence of a large volume fraction of hard second phase particles. Alloy 3 was also stable with heat treatment with only slight changes in the tensile properties after exposure to elevated temperatures.

Alloy 4, was only tested in the as-received condition. Alloy 4 has very high strength levels (159 Ksi yield strength, and 190 Ksi ultimate tensile strengths) but the elongation was only about 1%. The limited elongation prevented measurement of the strain hardening and strain rate sensitivity coefficients because the sample would break before any appreciable degree of plastic deformation was obtained.

Elevated temperature tensile tests were also performed on alloys 1 through 4. The room temperature (25°C), 525°C and 700°C tensile data obtained for each microcrystalline alloy are summarized in Table 8.

The trends of reduced strengths and increased failure elongations are similar to those associated with conventional iron and nickel-based alloys, such as the Hastelloys, Inconels and austenitic stainless steels.

Based on the room and elevated temperature tensile data, these

TABLE 8: TENSILE DATA FOR ALLOYS 1-4 AT VARIOUS TEMPERATURES

Alloy #	Temperature, °C					
	25		525		700	
	σ_{uts} (Ksi)	ϵ (%)	σ_{uts} (Ksi)	ϵ (%)	σ_{uts} (Ksi)	ϵ (%)
Alloy 1	196	9.0	168	13.5	114	26.9
Alloy 2	178	8.1	141	12.3	122	17.9
Alloy 3	122	>15.5	95	13.8	70	20.2
Alloy 4	190	1.2	146	7.6	113	12.8

microcrystalline alloys appear satisfactory for a number of intermediate temperature applications.

III-3. Fracture Toughness Data

Three point bend specimens with the dimensions shown in Figure 11 were used for toughness testing. The specimens were machined with the crack propagation direction perpendicular to the axis of the extruded rod. The specimen dimensions were kept small to reduce material usage and waste relative to the supplied bar stock. The alloys were tested in the same heat treated conditions as in the tensile testing with the exception that alloy 4 was also tested after being heat treated at 900°C for two hours.

Fatigue precracking of alloys 1 through 3 was done using a cantilever bending arrangement. Alloy 4 could not be precracked as it would break before the fatigue crack initiated. The load, p' , applied to the fixed end of the bar due to the cyclic displacements, was measured with a load cell and was cycled between 0 and P_{max} . P_{max} ranged from 25 kilograms up to 60 kilograms in a given test depending on the alloy and fatigue crack length. As the crack length, a , approached $.6W$, the maximum load had to be decreased to limit plastic zone size (7).

After the first set of toughness tests, it was found that alloys 1 through 3 did not satisfy the size requirement criteria set forth in ASTM E-399 (7) and given by

$$b > 2.5(K_{IC}/Y)^2 \quad [1]$$

Here, b = specimen thickness (.148"), K_{IC} = measured fracture toughness and Y = uniaxial yield strength. Alloy 4 did, however, because of its low toughness and high strength meet this requirement. Since the dimensions of the test specimens did not meet the size

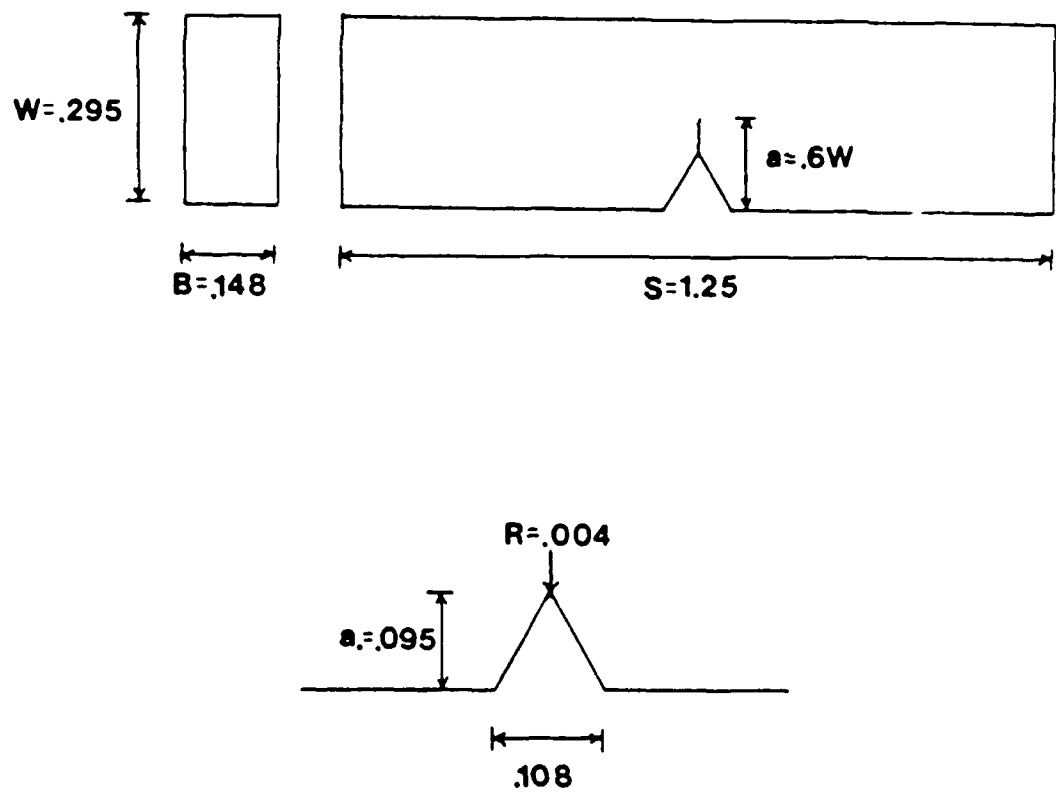


Figure 11: Three point bend test specimen dimensions.

requirements of ASTM E-399 in alloys 1 through 3, the toughness tests were done according to ASTM E-813 where J_{IC} values were measured. Therefore, the only changes that had to be made to meet the E-813 fatigue precracking requirements was that the fatigue precrack had to be slightly longer ($a = .6W$ instead of $.5W$).

To determine J_{IC} , the areas under the load - load point displacement curve (up to crack initiation) were measured. Specimens precracked to the appropriate length (with the exception of alloy 4) were loaded in three point bending. The load point displacement speed used in all the toughness tests was .05 cm/min.

With the exception of alloy 4, K_{IC} 's were determined by measuring J_{IC} and then calculating K_{IC} using Equation 2

$$K_{IC} = \sqrt{J_{IC} E} \quad [2]$$

where E = Young's modulus (7).

The data obtained from testing of all four microcrystalline alloys in the 'as-received' and heat treated conditions are given in Table 9. The toughness listed are averages of two values except for alloy 4 in the heat treated condition where only one value was obtained. The toughness values of all the microcrystalline materials are fairly low when compared to conventional alloys of similar composition. Of the two nickel based alloys, alloy 1 had the lower toughness and this value did not change with heat treatment. Alloy 2 had a slightly higher toughness than alloy 1 (as would be expected by comparing yield strengths) and it also increased by 20% after aging at 1000°C, most likely due to coarsening of the second phase particles present in the matrix.

Alloy 3 had the highest fracture toughness of all four microcrystalline in the 'as-received' condition with $K_{IC} = 73.2 \text{ MPa}\sqrt{\text{m}}$. Upon heat treatment this

TABLE 9: FRACTURE TOUGHNESS RESULTS OBTAINED FOR THE MICROCRYSTALLINE ALLOYS. ALL K_{IC} VALUES IN $\text{MPa}\sqrt{\text{m}}$.

Alloy	Heat Treatment	K_{IC} LEFM	J_{IC} [J/m ²]	K_{IC} (by J_{IC})
1	As Received	—	8454 8859	44.0
	1000°C - 10 hrs	—	6597 12348	48.5
	1000°C - 20 hrs.	—	8589 12357	46.0
2	As Received	—	13990 —	53.7
	1000°C - 10 hrs.	—	20276 17368	62.4
	1000°C - 20 hrs.	—	16516 26518	66.0
3	As Received	—	32140 —	73.2
	1000°C - 10 hrs.	—	12828 22920	54.0
	1000°C - 20 hrs.	—	12212 19056	50.7
4	As Received	27.0	—	—
	1000°C - 20 hrs.	17.5	—	—

toughness dropped about $50 \text{ MPa}\sqrt{\text{m}}$. This was unexpected based on the tensile data for this alloy.

As expected from examining the ductility data obtained during tensile testing, alloy 4 had the lowest toughness of all four microcrystalline alloys. The K_{IC} value obtained for the 'as-received' material was only $27.0 \text{ MPa}\sqrt{\text{m}}$. After heat treating the toughness decreased even further to a level of $17.5 \text{ MPa}\sqrt{\text{m}}$ most likely due to the increase in boride content and σ -phase formation during the heat treatment.

The general trends found in the toughness data were typical of most metals and alloys. As yield strength increased and ductility decreased, the toughness was also found to decrease.

III-4. Stress Corrosion Cracking

Stress corrosion cracking behavior was investigated in 1N-NaCl solution at room temperature, boiling 42% MgCl_2 solution at 130°C , and 0.1N- $\text{Na}_2\text{S}_2\text{O}_3$ solution at room temperature, using fatigue-cracked, disk-shaped, compact-tension DC(T) specimens loaded under constant displacement conditions. The crack plane and crack propagation direction of the DC(T) specimens were parallel to the extrusion axis and perpendicular to the extrusion axis, respectively. The geometry of the DC(T) specimen conforms to that given by E-399 (7). The thickness of the DC(T) specimens were 7.06 mm.

All results obtained in the stress corrosion cracking SCC experiments for the as-received alloys are summarized in Table 10. The experiments were conducted under fixed grip conditions during which the crack velocity can be calculated from the rate of load drop and, in our experiments, a velocity as small as $6 \times 10^{-10} \text{ m/s}$ could be detected with certainty. The remarkable consequence of these experiments is that, to within the limits of our ability to sense a crack length change, crack velocity was not detected in any of the

alloys at open circuit potentials in 1N NaCl at room temperature, in 42% boiling MgCl_2 (at 145°C), or in 0.1N $\text{Na}_2\text{S}_2\text{O}_3$ solution also at room temperature. Also, no cracking was observed in 1N NaCl at applied potentials somewhat more positive or more negative than the open circuit potentials.

The excellent SCC resistance displayed by these alloys, while intriguing, should be regarded with some caution. The reason for the lack of cracking in the chloride and thiosulfate solutions is not clear and certainly other environments could be much more aggressive. However, the observations do suggest that these relatively high strength materials possess a unique resistance to environmentally-assisted cracking.

IV. OXIDATION CHARACTERISTICS

The oxidation rates of the four microcrystalline alloys and several comparison iron and nickel-based alloys were measured with a Cahn R-100 recording microbalance mounted above a vertical furnace. All oxidation tests were performed in air with the specimen lowered into a hot furnace and suspended on the balance at the start of each run. A schematic drawing of the oxidation apparatus is shown in Figure 12. The microcrystalline alloy specimens were disks with dimensions 12 x 1.5 mm. The dimensions of coupons cut from wrought sheets of other alloys were about 10 x 10 x 1 mm. All samples were ground to a 600-grit metallographic finish. The oxidation products were analyzed by X-ray back-diffraction of the intact scale, by scanning electron microscopy, and by scanning Auger microscopy.

The isothermal oxidation characteristics of the four microcrystalline alloys 1-4, were studied in air at 800°, 900°, 1000°, and 1100°C. The oxidation kinetics in air of selected wrought high-temperature alloys were also established at 900° and 1100°C.

TABLE 10. STRESS CORROSION CRACKING RESPONSE OF MICROCRYSTALLINE ALLOYS

Solution	Alloy	Applied Stress Intensity ^(a)	Applied Potential (mV SCE)	Results
1N-NaCl at room temp.	Alloy 1	0.80 K_{Ic}	0	No ^(c)
			O.C.P ^(b) (-280)	No
			-380	No
	Alloy 2	0.64 K_{Ic}	0	No
			O.C.P (-315)	No
			-420	No
	Alloy 3	0.66 K_{Ic}	-150	No
			O.C.P (-410)	No
			-510	No
Boiling 43% MgCl ₂ (130°C)	Alloy 4	0.76 K_{Ic}	-100	No
			O.C.P (-320)	No
			-420	No
	Alloy 1	0.78 K_{Ic}	O.C.P	No
	Alloy 2	0.61 K_{Ic}	O.C.P	No
	Alloy 3	0.60 K_{Ic}	O.C.P	No
	Alloy 4	0.75 K_{Ic}	O.C.P	No
0.1N Na ₂ S ₂ O ₃ at room temp.	Alloy 1	0.80 K_{Ic}	O.C.P	No
	Alloy 2	0.61 K_{Ic}	O.C.P	No
	Alloy 3	0.64 K_{Ic}	O.C.P (-210)	No
			-100	No
	Alloy 4	0.75 K_{Ic}	O.C.P (-170)	No
			-70	No

(a) All DC(T) specimens were fatigue pre-cracked prior to testing.

(b) O.C.P: Open circuit potential.

(c) No: Crack velocity was less than 6.0×10^{-10} m/s, the limit of detection.

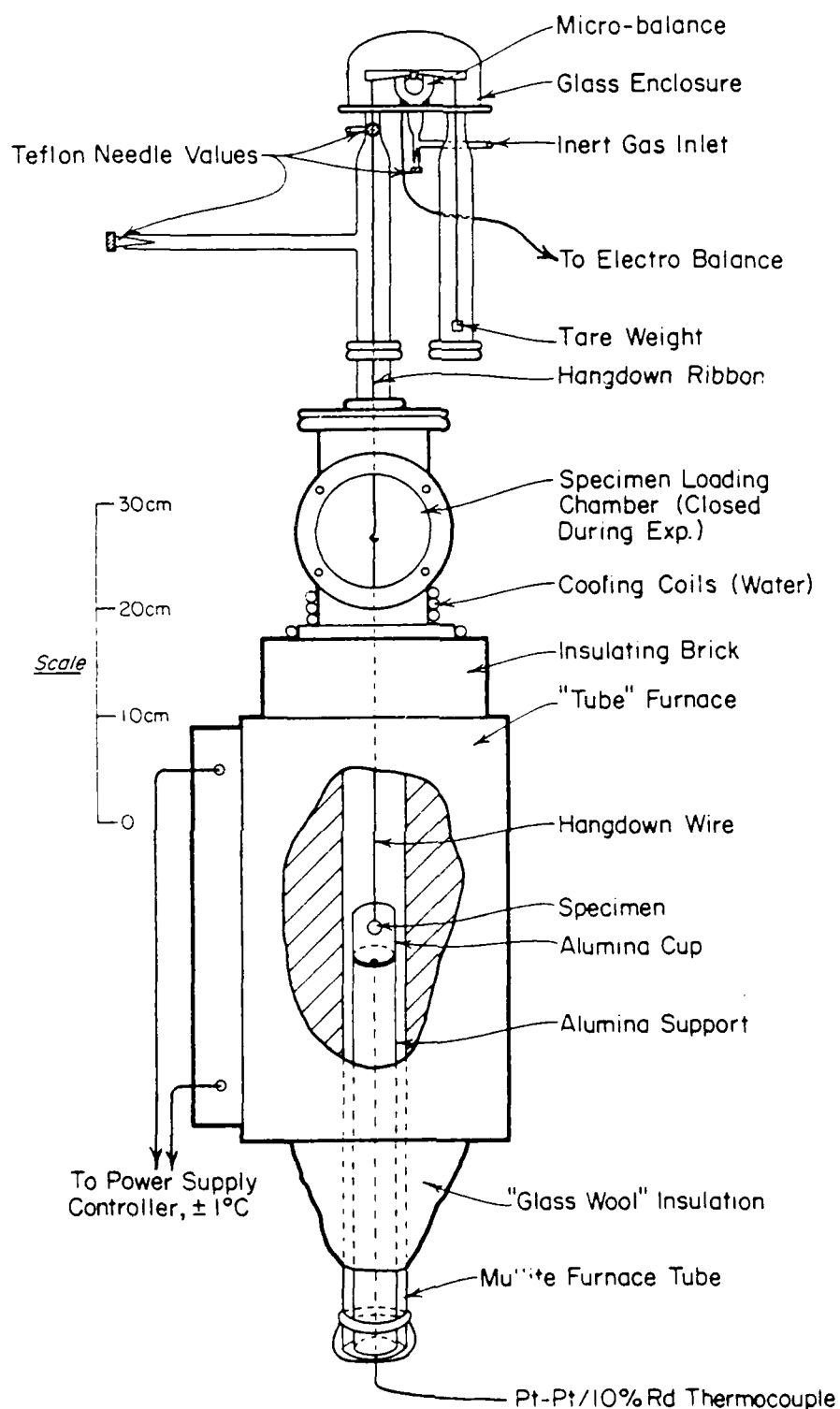


Figure 12: Schematic of Oxidation Furnace-Balance System.

Gravimetric data for the oxidation of the microcrystalline alloys at 800°C are shown in Figure 13. Initially, alloys 1, 3, and 4 oxidized rapidly but all alloys achieve virtually zero steady-state growth rates after 40 to 60 minutes. The oxides on all four alloys were thin, adherent (found by scratching the surface with a tungsten probe), and fine-grained (as shown in Figure 14).

Figure 15 shows the gravimetric data for the microcrystalline alloys at 900°C. Initially, all four alloys oxidized rapidly but this was followed by very low steady-state growth rates. The "stepped" kinetics for alloys 1, 3, and 4 indicates a local breakdown and healing of the protective scale. Inhomogeneous alloy composition or structure or variable specimen preparation, e.g., deep scratches or other surface abnormalities, may have been involved. A repeated run for alloy 1 did not demonstrate the same "stepped" behavior, but it did achieve the same overall weight gain/area after 18 hours.

Morphologically, the scales formed at 900°C are similar to those formed at 800°C as seen in Fig. 16. Although alloys 2 and 4 differed in composition and oxidation kinetics, their protective scale morphologies were similar. This kind of nodular morphology was observed by Yurek et al. (8) on fine-grained 303 stainless steel made from rapidly solidified powder.

Figure 17 shows the gravimetric data for the oxidation of Hastelloy X, Inconel 600, and 316, 330, and 333 stainless steels at 900°C. The initial parabolic oxidation kinetics for Inconel 600, 330, and 333 stainless steels are followed by low steady-state scale growth rates. Hastelloy X and 316 stainless steel oxidize more rapidly initially but exhibit very low growth rates after 4 to 8 hours.

Nickel-base alloys 1 and 2 exhibit oxidation kinetics different from the iron-base alloys 3 and 4 at 1000°C. As shown in Figure 18, alloys 1 and 2

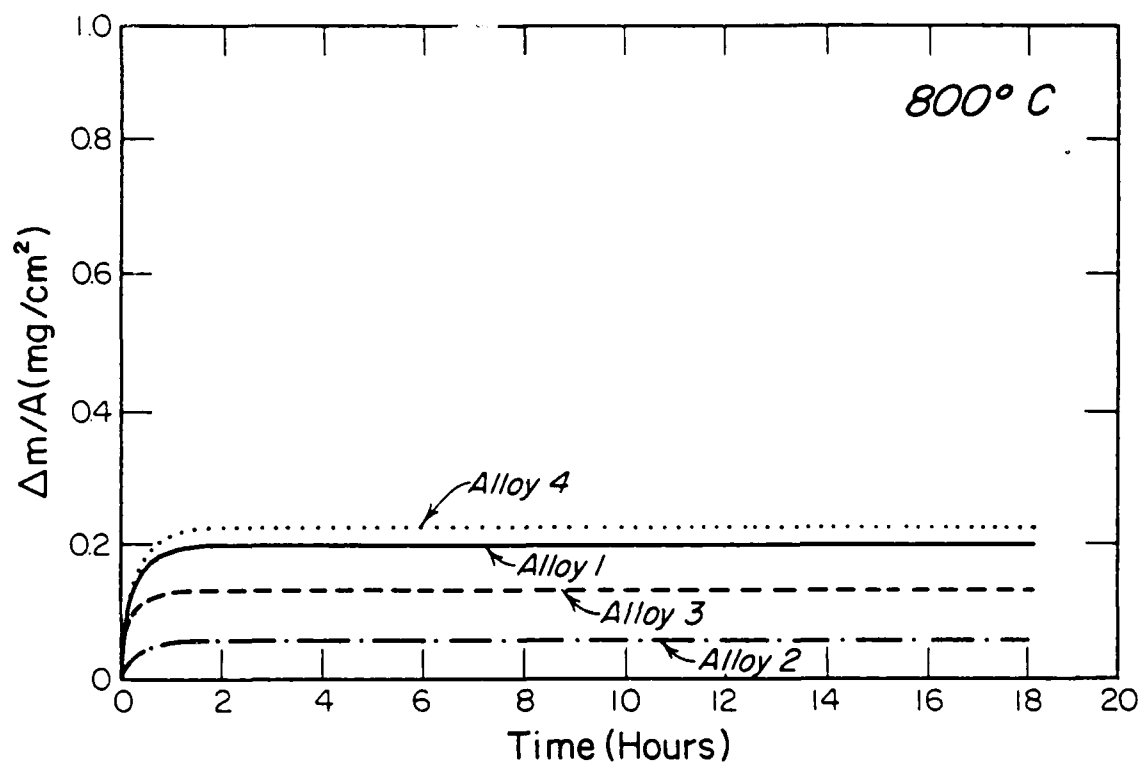


Figure 13: Weight gain of microcrystalline alloys oxidized in air at 800°C.

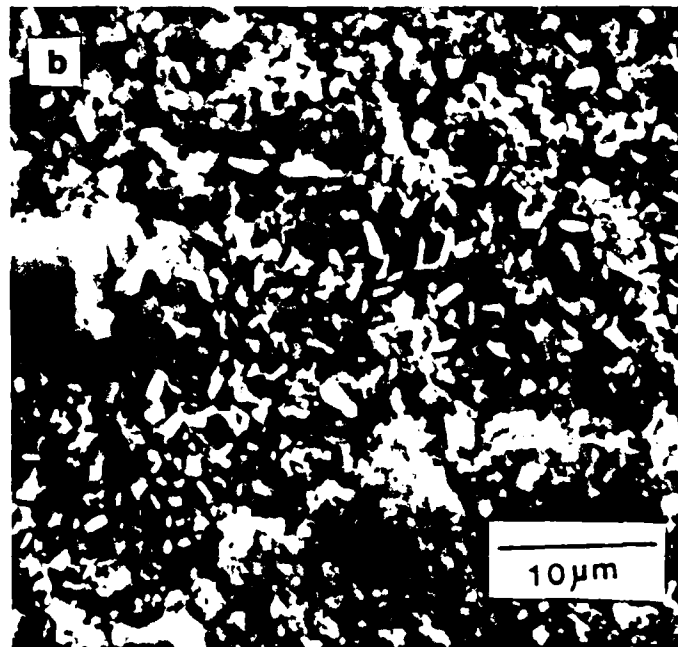
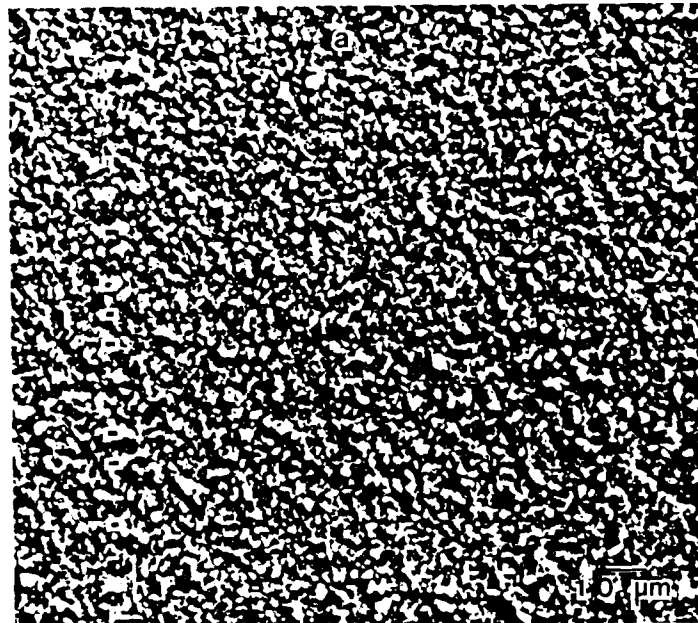


Figure 14: Scale morphology of alloy 1 after 18 hours oxidation in air at 800°C; (a) 550X, (b) 2000X.

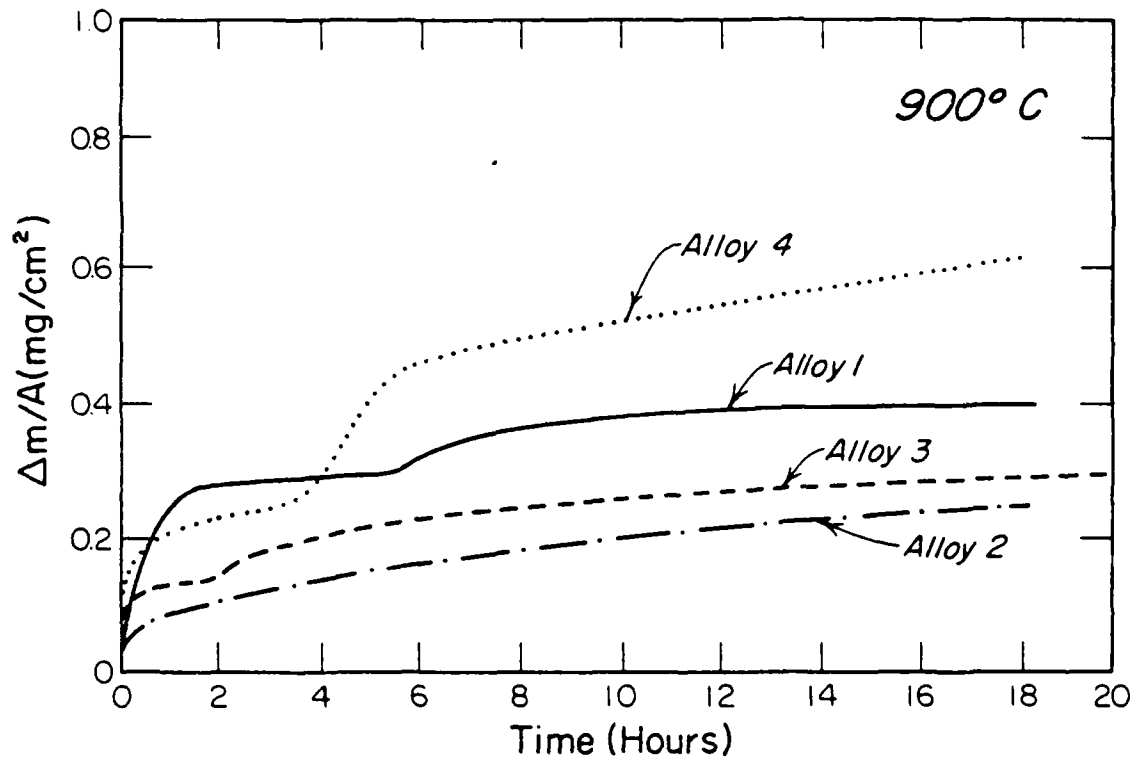


Figure 15: Weight gain of microcrystalline alloys oxidized in air at 900°C.

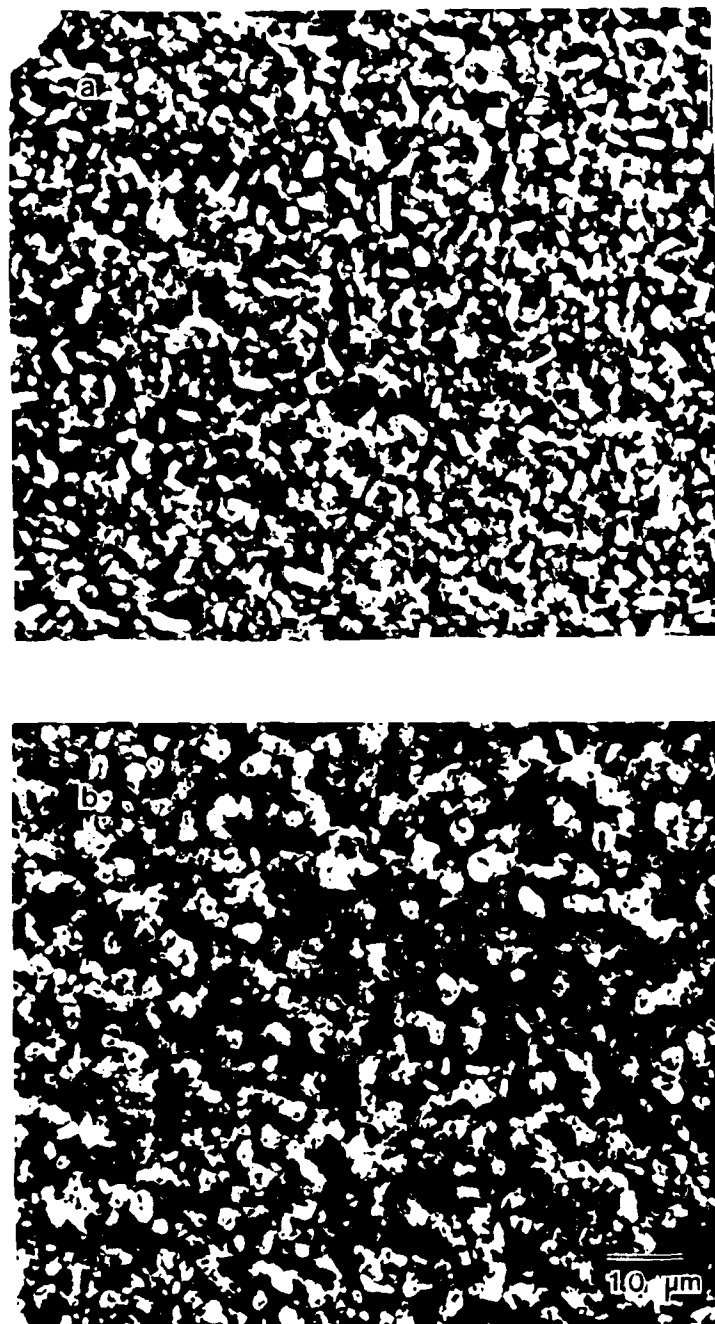


Figure 16: Scale morphologies after 18-20 hours oxidation in air at 900°C; (a) alloy 2, 1000X, (b) alloy 4, 1000X.

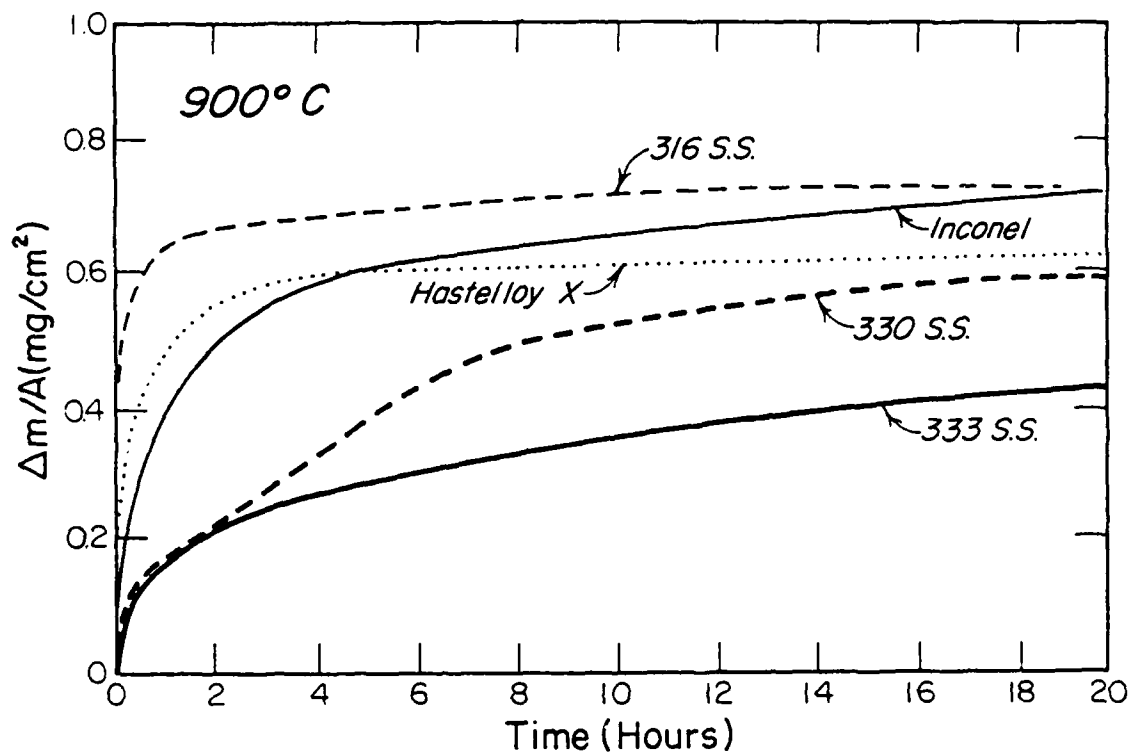


Figure 17: Weight gain of comparison alloys oxidized in air at 900°C .

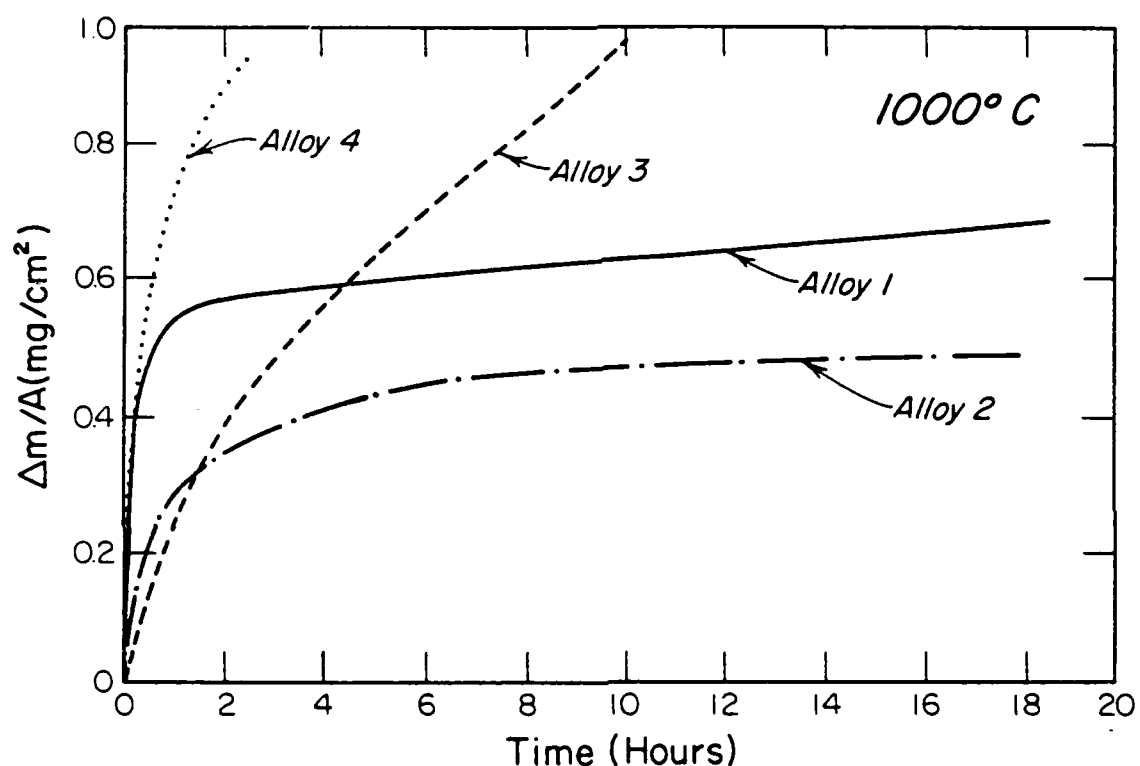


Figure 18: Weight gain of microcrystalline alloys oxidized in air at 1000°C.

achieve slow, linear growth rates after 2 and 6 hours, respectively. Alloys 3 and 4 oxidized rapidly and did not achieve a slow growth regime during the duration of the experiment. Their scales had a rough morphology and were cracked at the periphery of the specimens.

The scale morphology of alloy 2, as observed with SEM, is shown in Figure 19. The scale has a porous, nodular outer layer and a dense, smooth protective layer underneath. An area covered by pyramids (Fig. 19 (c), center) is a common morphological feature for scales of NiO grown on pure nickel at high temperatures (9), on rapidly solidified 303 stainless steel (8), and on 330 stainless steel (see Fig. 19 (d)). An EDAX analysis of these pyramids showed a high concentration of nickel, supporting the hypothesis that they are nickel oxide.

Gravimetric data for the oxidation of the microcrystalline alloys at 1100°C are shown in Fig. 20. Alloys 1 and 2 exhibit slow approximately parabolic growth rates but alloys 3 and 4 oxidize catastrophically. The scales on alloys 1 and 2 were relatively smooth and compact and did not spall immediately upon cooling but did flake off at the edges during subsequent handling and analysis. The scale morphology of the nickel-base alloy 1 after 1.5 hours oxidation at 1100°C shown in Fig. 21 exhibits the typical "convoluted" appearance of Cr_2O_3 as found by other authors (8, 9). The ridges shown in Figure 21 b have not previously been reported. Whiskers have grown in the "valleys" between convolutions where the scale is attached to the substrate (10).

As shown in Fig. 22, the iron-base microcrystalline alloys were oxidized through after exposure of about 20 hours. The appearance of the alloys is similar to alloys with high-Mo contents that experience catastrophic oxidation (10, 11). A powdery film, identified by X-ray diffraction as MoO_3 , was

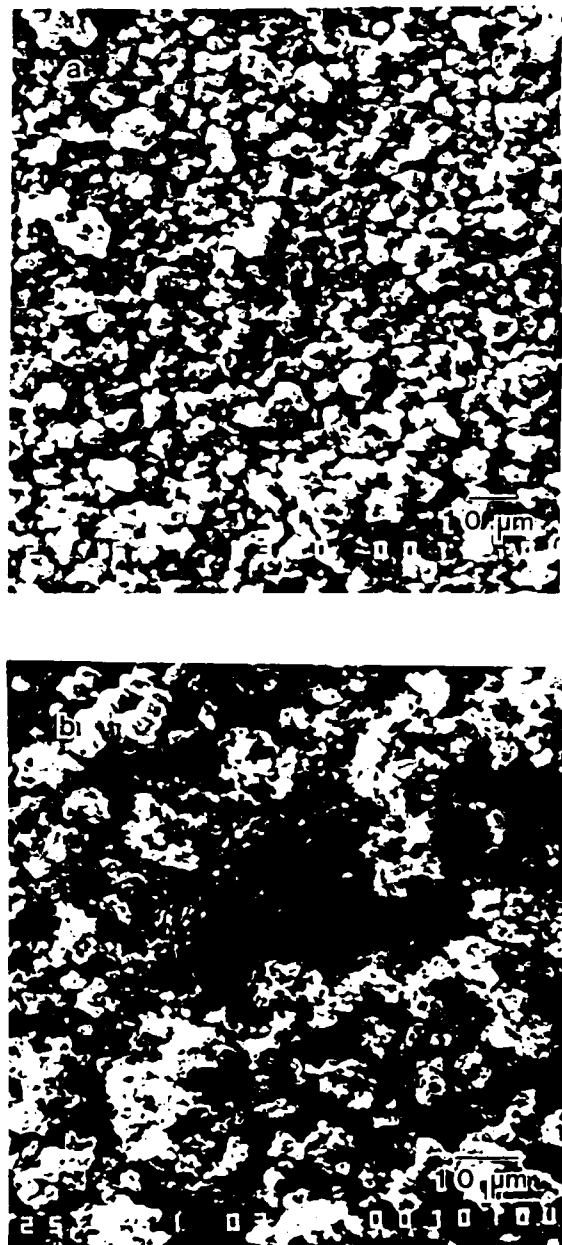


Figure 19: Scale morphology and features of alloy 2 after 8 hours oxidation in air at 1000°C; (a) porous outer layer, (b) protective inner scale.

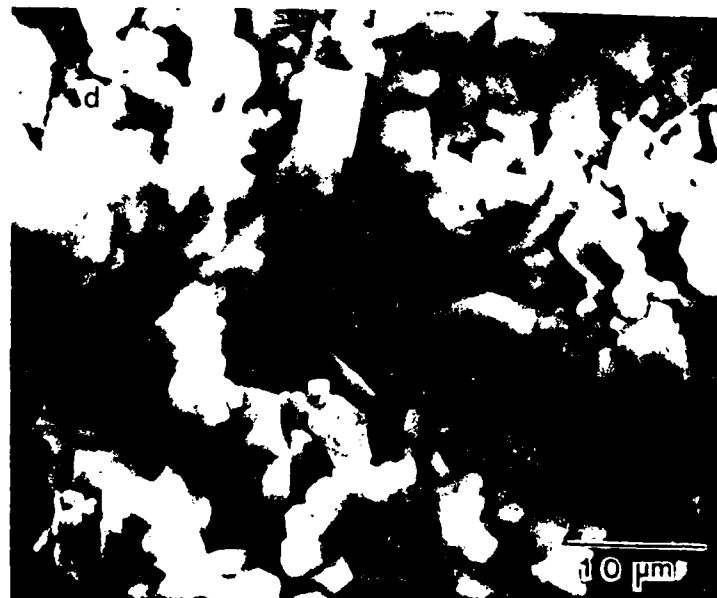
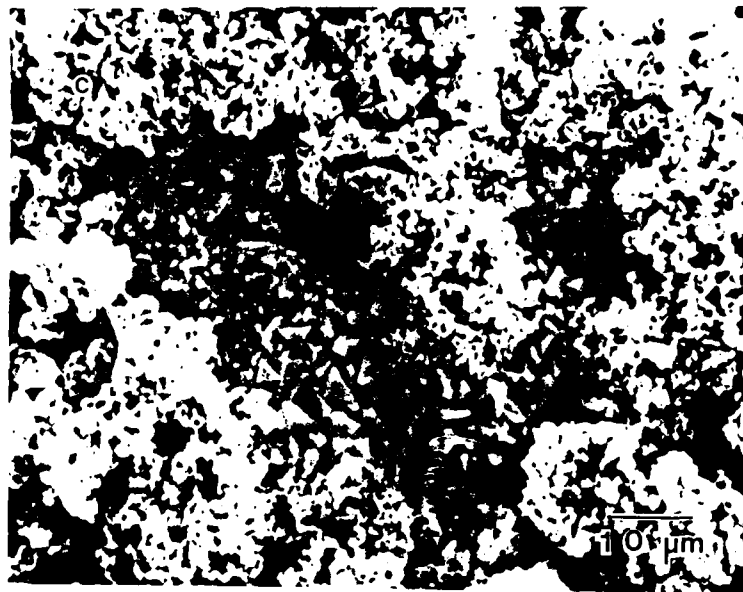


Figure 19: (Cont'd) (c) pyramids 1000X, (d) pyramids on 330 stainless steel 2000X.

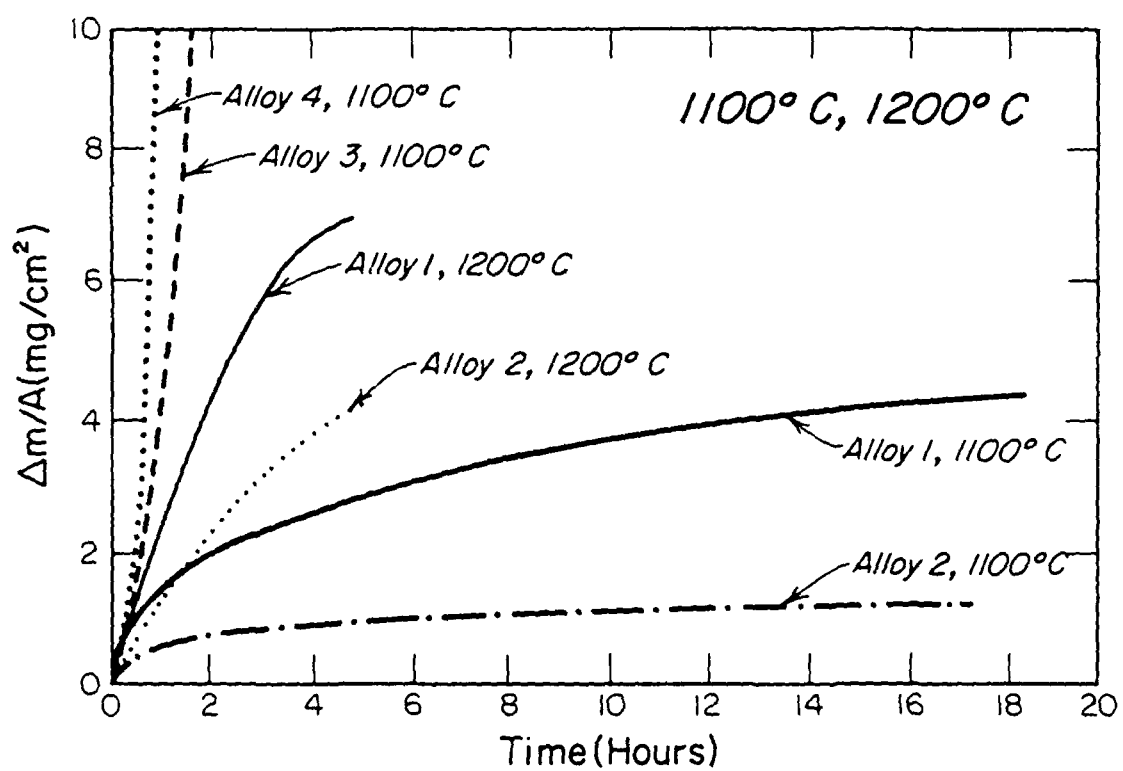


Figure 20: Weight gain of microcrystalline alloys oxidized in air at 1100 and 1200°C.

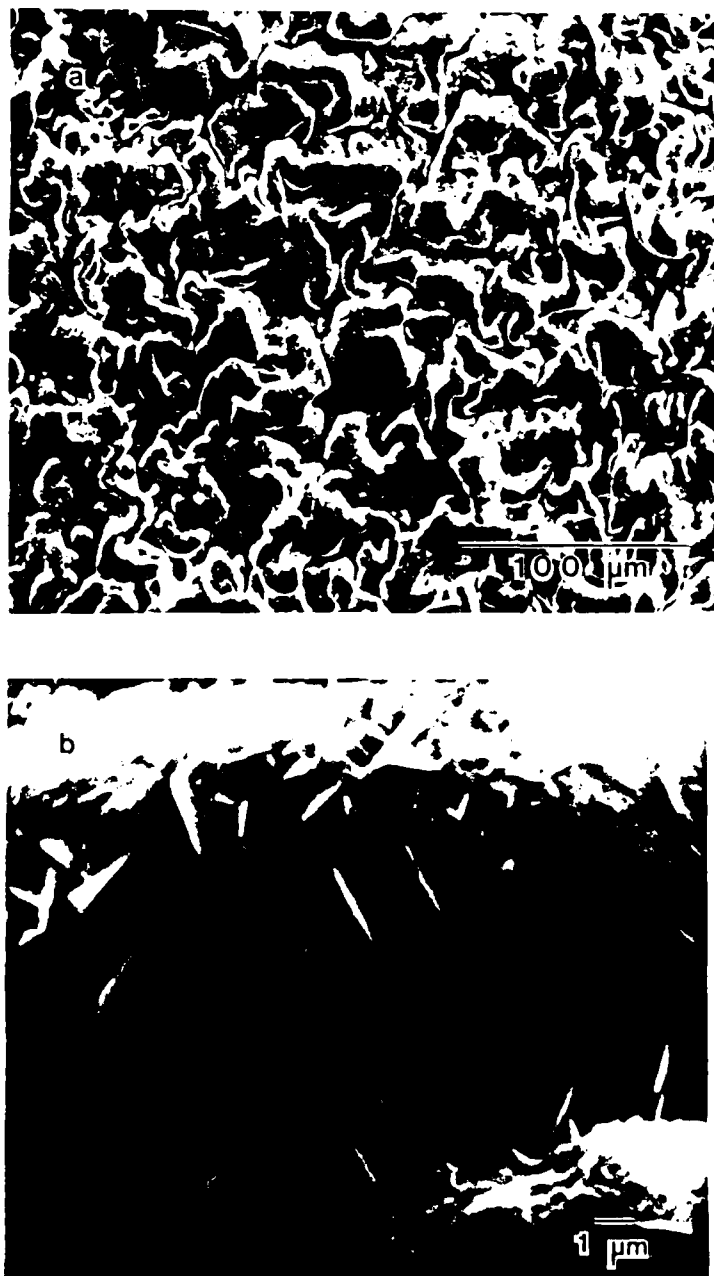


Figure 21: Scale morphology of alloy 1 after short time (1.5 hours) oxidation at 1100°C; (a) convoluted appearance at 300X, (b) ridges on convolutions at 5000X. EDAX analysis: all Cr.



Figure 22: Visual appearance of alloys 3 and 4 after rapid oxidation at 1100°C; (a) alloy 3, (b) alloy 4.

deposited on the inside surfaces of the apparatus during those experiments. Molten MoO_3 would act as a hot corrosion agent (a very acidic fused salt) in contact with the alloy or the scale. Although the bulk concentrations of Mo in alloys 3 and 4 were only 5.04 wt% and 11.22 wt%, respectively, the local enrichment of Mo resulting from chromium depletion beneath a Cr_2O_3 scale would place the alloy composition at the alloy/scale interface in a regime where rapid attack is likely (12).

The gravimetric data obtained for the nickel-base alloys 1 and 2 at 1200°C are also shown in Fig. 20. After five hours oxidation, the scales were smooth and protective at temperature, but spalled considerably upon cooling.

Figure 23 shows the gravimetric data for the other high-temperature, chromia-forming alloys after oxidation in air at 1100°C . Although Hastelloy X, Inconel 600, and 330 stainless steel displayed desirable kinetic behavior for high-temperature use, only Hastelloy X retained an adherent scale upon cooling and handling.

Cyclic oxidation studies from 900°C to room temperature were also conducted for the microcrystalline alloys. As shown in Figure 24, a small weight loss, resulting from scale spalling, was observed on each cycle. In cyclic oxidation studies at 1100°C and higher, the iron-base alloys oxidized catastrophically and alloy 2 exhibited a net weight loss on each cycle. The weight gain of alloy 1 was similar to the isothermal oxidation of the alloy.

X-ray Diffractometry

The oxides positively identified by X-ray diffraction on specimens oxidized for 18 hours or more are presented in Table 11.

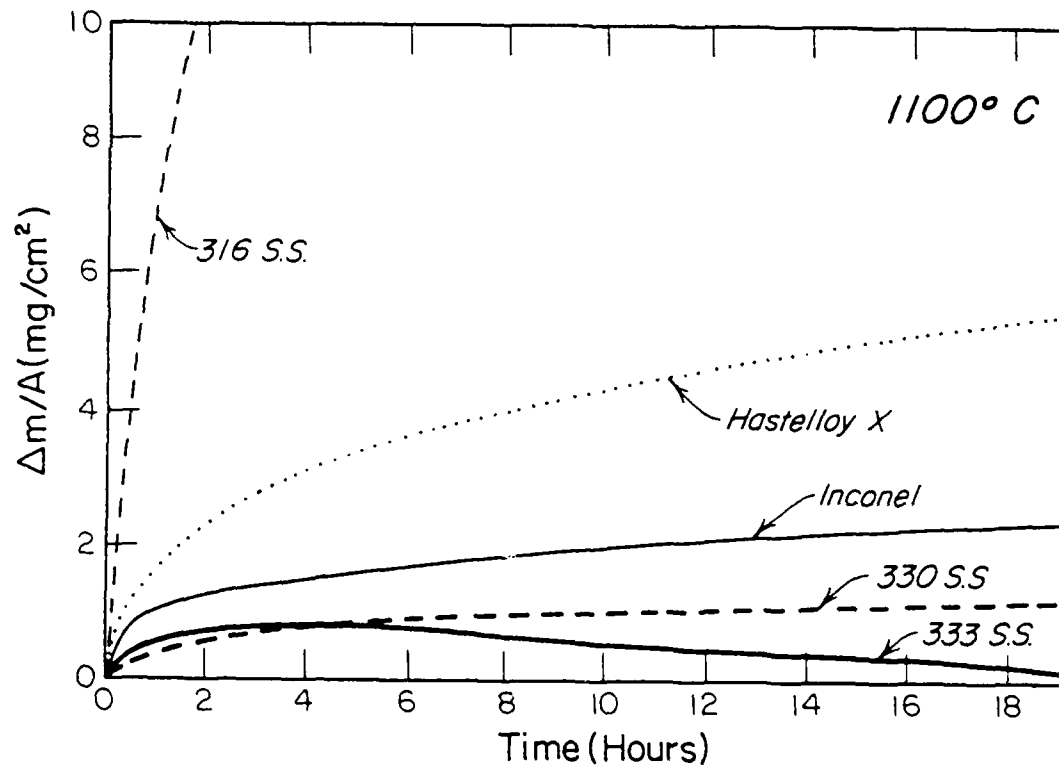


Figure 23: Weight gain of comparison alloys oxidized in air 1100°C.

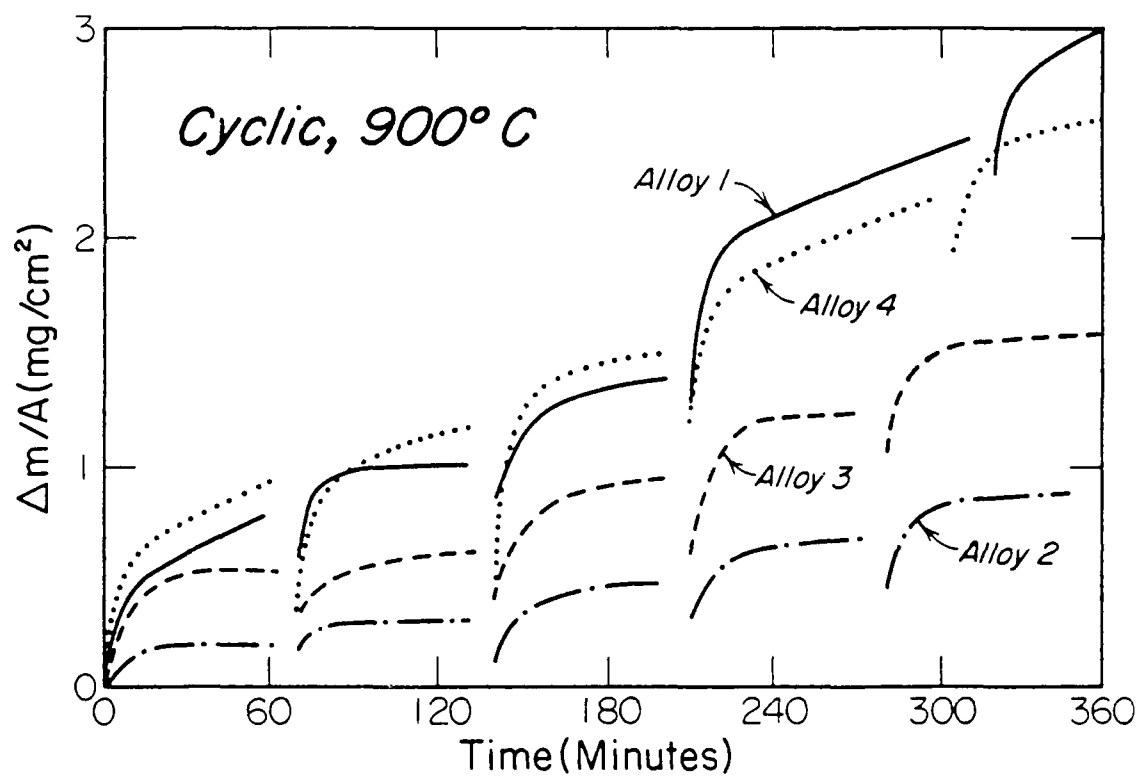


Figure 24: Weight gain for microcrystalline alloys during cyclic oxidation from 900°C.

TABLE 11: OXIDES IDENTIFIED BY X-RAY DIFFRACTION ON SPECIMEN
OXIDIZED FOR 18 HOURS IN AIR

Alloy	Temperature, °C			
	800	900	1000	1100
1	Cr ₂ O ₃	Cr ₂ O ₃	Cr ₂ O ₃	Cr ₂ O ₃
2	Cr ₂ O ₃	Cr ₂ O ₃	Cr ₂ O ₃	Cr ₂ O ₃
3	Cr ₂ O ₃	Cr ₂ O ₃	Cr ₂ O ₃ /Fe ₂ O ₃ /NiO	Fe ₂ O ₃ /NiO
4	Cr ₂ O ₃	Cr ₂ O ₃	Cr ₂ O ₃ /Fe ₂ O ₃ /NiO	Fe ₂ O ₃ /NiO

From the weight-gain versus time plots, the oxidation kinetics of the microcrystalline alloys are comparable to wrought high-temperature, chromia-forming alloys. The scale morphologies consist of an outer layer of the base metal oxide over a protective layer of chromia as expected for alloys such as Ni-20Cr and Fe-20Cr. Thin layers of spinel may also be present and help in the oxidation resistance, but only Cr₂O₃ was detected by x-ray diffraction. Generally, the commercial wrought alloys studied exhibited similar behavior. The products NiO or Fe₂O₃ were not detected by X-ray diffraction of the protective Cr₂O₃ scales formed on the microcrystalline alloys, nor was Fe or Ni found in the scales by EDAX.

The nickel-base alloy 2 and the iron-base alloy 3 exhibit the lowest overall weight gains at 800 and 900°C of all the alloys studied (see Figs. 13, 15, and 17). Interestingly, they have the lowest Cr and B contents of the microcrystalline alloys. Oxidation of the nickel-base alloys 1 and 2 at 1000, 1100, and 1200°C showed that the lower Cr, lower B alloy 2 exhibited less overall weight gain and therefore a slower growth rate. Other specific compositional dependencies were not obvious.

Alloy 2 has the best isothermal oxidation characteristics of the alloys studied. However, when cycled from 1100°C to room temperature a net weight loss results from poor scale adhesion.

The oxidation kinetics of the alloys studied may be described by one or more parabolic or parabolic functions of time. Although a parabolic growth rate was not exactly obeyed, a series of parabolas with different constants may be applied to the data in a best-fit manner. The data are linear when plotted in this parabolic manner, and the slopes of the lines provide the instantaneous parabolic (gravimetric) rate constants according to the expression $k_p = d(\Delta m/A)^2/dt$. The data will be compared further through these constants.

Steady-state rate constants calculated for times of 8 to 20 hours are shown graphically in Fig. 25. The rate constants for 316 stainless steel are not included on Fig. 25 because they lie above the scale shown. The constants for 333 stainless steel reflecting a weight loss (see Fig. 23) are not shown.

A linear dependence for the logarithm of the rate constant versus inverse temperature indicates that one rate-limiting diffusion step dominates. For chromia scales, the rate limiting step is the diffusion of chromium ions, probably over scale grain boundaries, to the scale/gas interface. The departure from linearity at 900°C (see Fig. 26) may be caused by dopants which could affect the rate of grain boundary diffusion across the scale.

The steady-state rate constants for the iron-base alloys 3 and 4 are higher than those for Hastelloy X. The rate constants for the nickel-base alloys 1 and 2, however, are lower. Rate constants for alloys 1 and 2 are lower than those for Inconel 600 and 330 stainless steel at 900°C but higher at 1100°C. Caplan and Sproule (13) have compiled the parabolic rate constants for the oxidation of pure chromium. Their composite data centers about one order of magnitude lower than 330 stainless steel with about the same slope.

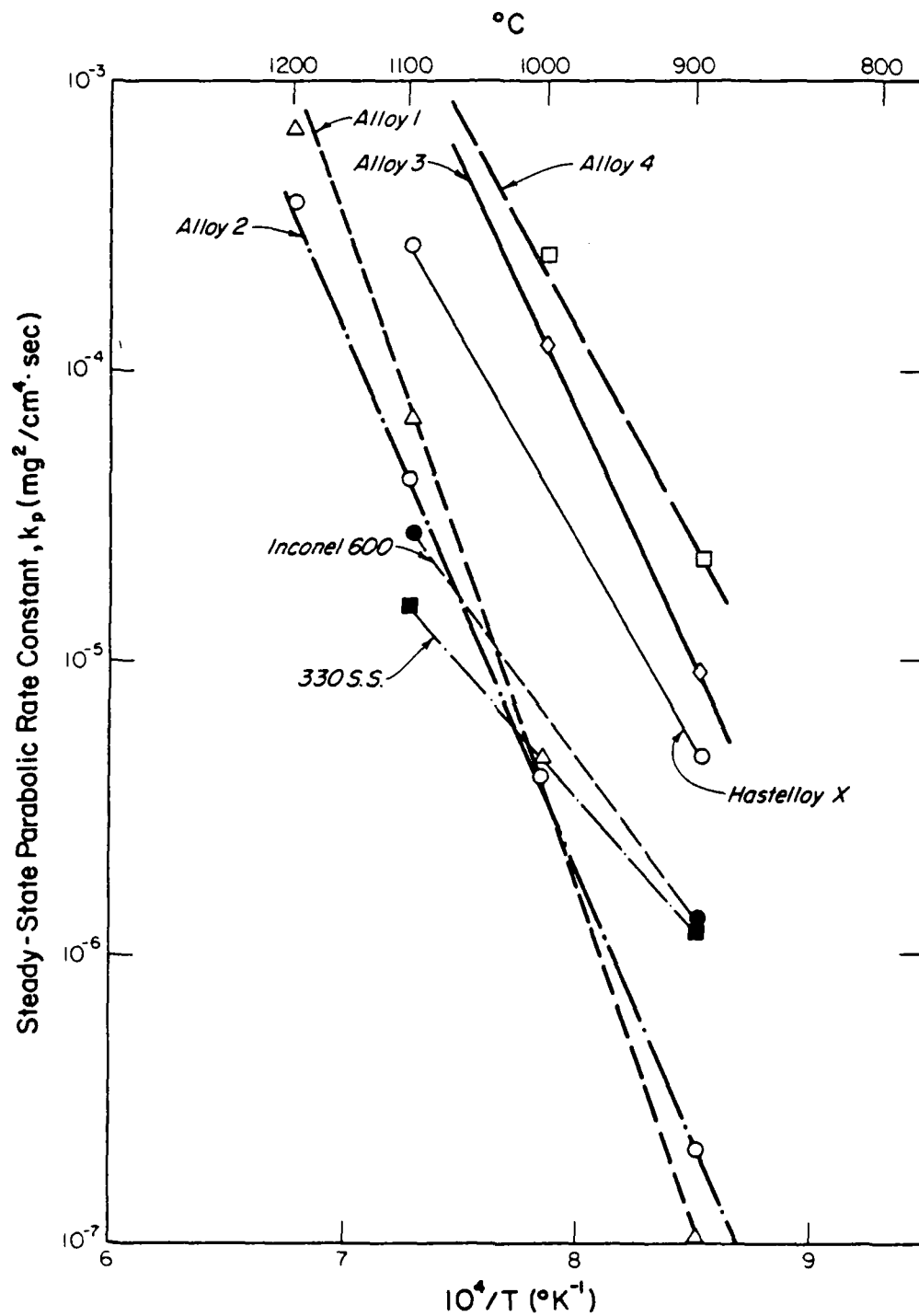


Figure 25: Steady-state (8-20 hours) parabolic rate constants for alloys studied.

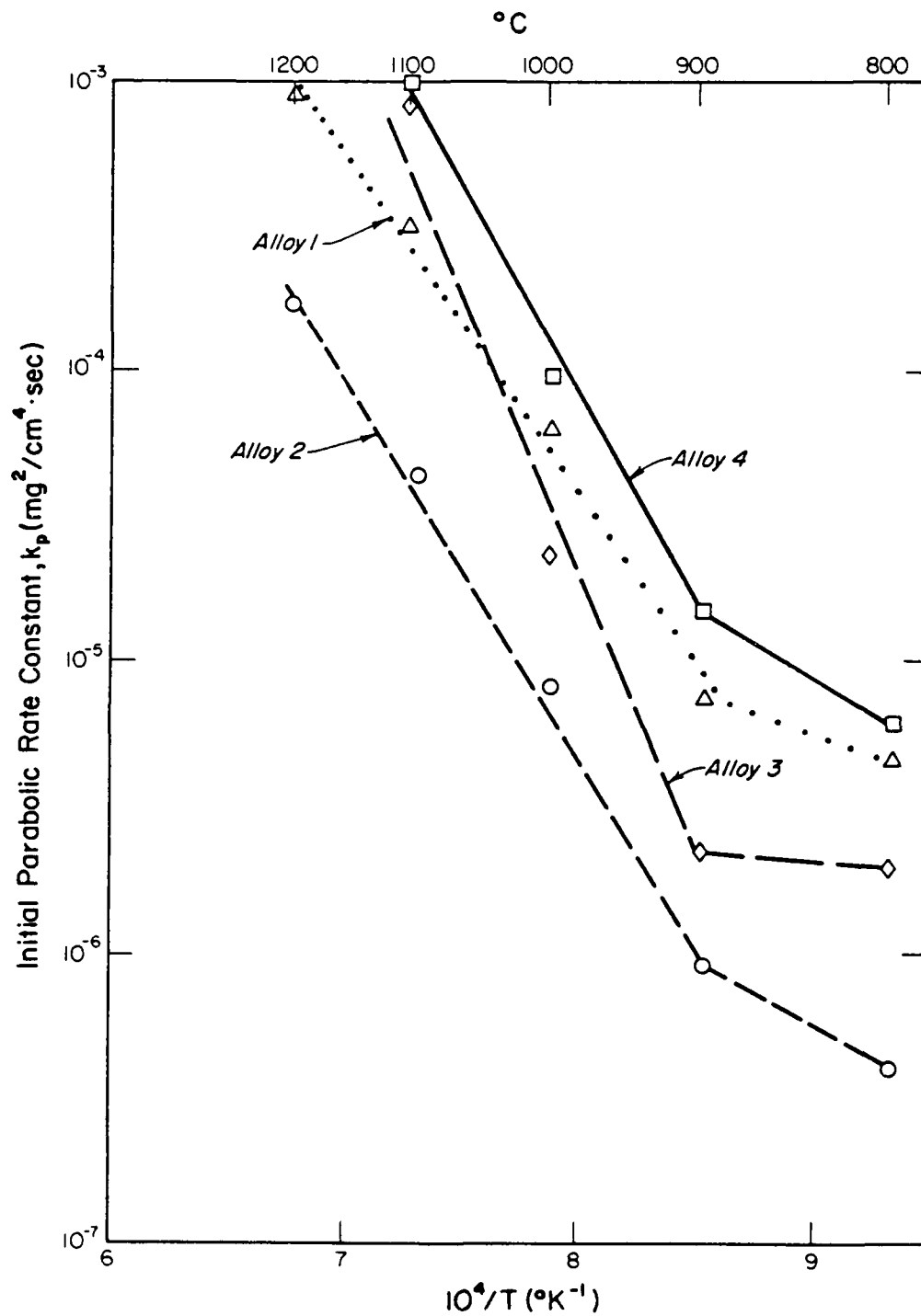


Figure 26: Initial parabolic rate constants for the oxidation of microcrystalline alloys.

To interpret the differences in slopes on Fig. 25, activation energies, Q , for steady-state parabolic scaling were calculated and are listed in Table 12. The microcrystalline alloys display much higher activation energies both initially and for long time (ca. 20 hours) oxidation.

The component(s) that oxidized initially could account for the long time behavior. A plot of initial parabolic rate constants for the microcrystalline alloys (Fig. 26) and for the comparison alloys (Fig. 27) clearly shows the higher slopes, i.e., activation energies, for the microcrystalline alloys. According to Table 12, the values fall between those for the oxidation of Cr(13) and B(11). Initially, the oxidation of the microcrystalline alloys involves the oxidation of both chromium and boron.

As shown schematically in Fig. 28, the following model for protective scale formation is proposed:

- 1) Initially a liquid B_2O_3 ($T_m = 723K$) film forms that inhibits the oxidation of iron or nickel.
- 2) Chromia nucleates at the B-depleted alloy/scale interface and grows either by oxygen diffusion through the liquid film or by a displacement reaction between Cr in the alloy and the B_2O_3 .
- 3) The slow growing chromia eventually forms a continuous scale that stops the further oxidation of boron.
- 4) The initial B_2O_3 film must either remain at the outer surface of the scale, dissolve into the growing chromia, or evaporate. The vaporization of the B_2O_3 film is not expected because BO_2 , the predominate vapor species at high P_{O_2} , still has a relatively low vapor pressure at 900 and 1100°C.

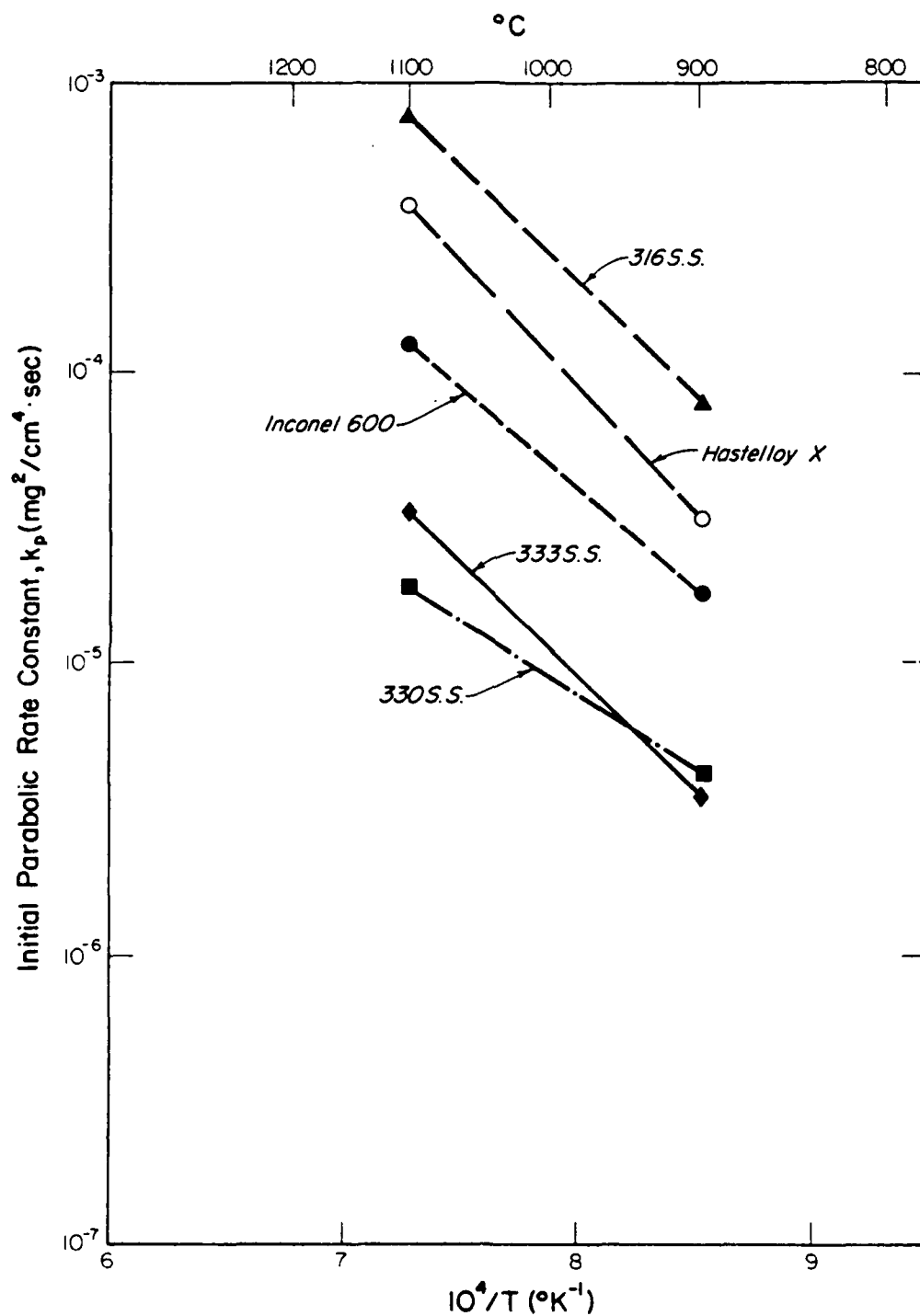
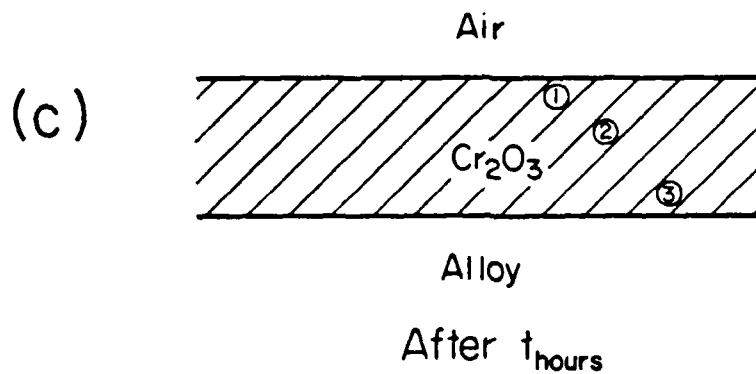
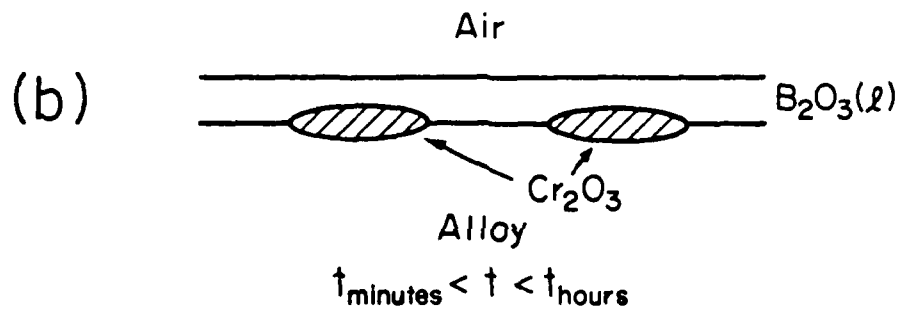
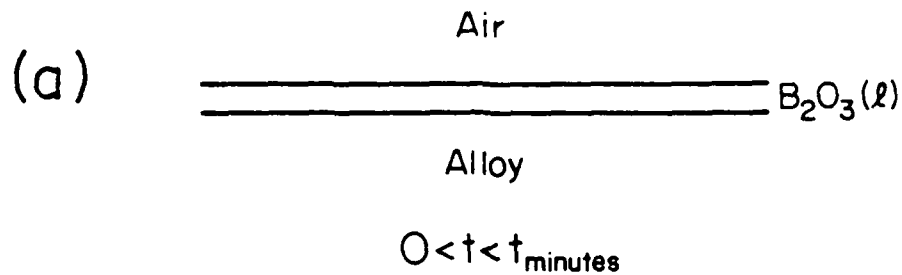


Figure 27: Initial parabolic rate constants for the oxidation of comparison alloys.

TABLE 12: ACTIVATION ENERGIES FOR VARIOUS METALS AND ALLOYS, kcal/mol

Metal/Alloy	Q steady-state	Q initial	Reference
Cr	58		13
Cr (single xl oxide)	55		16
Ni	40		17
B, T>900°C	77		11
B, T<900°C	12		11
Alloy 1	93	65	This Work
Alloy 2	86	68	" "
Alloy 3	82	72	" "
Alloy 4	92	70	" "
330 Stainless Steel	40	23	" "
Hastelloy X	64	39	" "
Inconel 600	49	32	" "



Boron Detected : ① Lea, Lloyd, et al
 ② None Detected
 ③ This Research

Figure 28: Oxidation model for boride strengthened microcrystalline alloys.

Boron oxide, B_2O_3 , is the thermodynamically most stable condensed oxide in this alloy system. Because of the high concentration of boron in these alloys (6.1 to 8.6 atomic %) selective oxidation should result in simultaneous nucleation of B_2O_3 and Cr_2O_3 . After Cr_2O_3 covers the alloy, some further reaction between Cr_2O_3 and boron in the alloy should form an underlying boron oxide film and further oxidation of boron would depend upon the slow diffusion in both Cr_2O_3 and B_2O_3 .

Lea (14) and Lloyd et al (15) have studied the oxidation-inhibiting effects of boron by oxidizing an Fe-10Cr alloy in a boron oxide vapor. Using Auger spectroscopy they detected B in the outer 10-20 nm of the chromia scale. They proposed a model whereby a network of boron and oxygen formed at the surface of the scale which inhibits the oxidation of the alloy. In the present model (Figure 19), the boron source is Fe-Mo-B precipitates within the alloy. Scanning Auger Microprobe (SAM) analysis of the protective scales on alloys 1 and 2 formed at 1100°C showed an enrichment of boron at the scale/alloy interface.

If a continuous B_2O_3 film is present on the alloy initially, it does not remain on the surface of the scale after extended oxidation. The Auger data support a scale growth model which involves the simultaneous nucleation of B_2O_3 and Cr_2O_3 where the B_2O_3 is either dissolved into the chromia (at high temperature) or evaporated.

V. CORROSION CHARACTERIZATION

The general objective of this task is to study the general, localized, and galvanic corrosion characteristics of four iron and nickel based micro-crystalline alloys under static or controlled hydrodynamic conditions.

Current Progress

The general corrosion tests for alloys 1 and 4 have been carried out at three rotation speeds (rpm = 600, 1200, 1800) in the rotating cylinder system at room temperature in deaerated 1 N hydrochloric acid.

Experimental Details

The design of the rotating cylinder system was previously reported (18). Tubular specimens were machined from the supplied 1" rod to the following dimensions:

Outside Diameter = 0.750", Inside Diameter = 0.625", Length = 0.500".

Three specimens were used for each rotation speed studied and were polished with SiC paper through grade 600. They were supported on the heavy wall 304 stainless steel tubing shaft and were electrically insulated from each other by Delrin spacers. For the specimens counted from top to bottom, the first specimen was used for measuring the polarization resistance using small amplitude cyclic voltammetry (SACV) and AC impedance techniques, the second specimen was used for recording the variation of corrosion potential with time and for potentiodynamic polarization studies, and the third specimen was used for direct weight loss measurement using a microbalance. A concentric, stationary, outer 316 stainless steel tubing (inside diameter = 1.5") was used as the counter electrode. Three holes (0.75" in diameter) were drilled on both the top side-surface and the bottom side-surface of the counter electrode to ensure the circulation of the solution. All potential measurements were made against a saturated calomel electrode (SCE) through a L-shape Luggin probe inserted into the gap between the outer stationary counter electrode and the inner rotating specimens through one hole on the top side-surface of the counter electrode. A mercury slip-ring was

used for the electrical contact. The shaft was driven by a DC motor with the rotation speed controlled by a speed controller to within ± 15 rpm of the desired values. A magnetic sensor was used for the digital read-out of a tachometer.

Results and Discussions

Corrosion Rate Measurements

Small Amplitude Cyclic Voltammetry (SACV)

SACV data were obtained by imposing a small amplitude (20 mV peak-to-peak) triangular potential excitation across the interface at the corrosion potential. Voltage sweep rates ranging from 0.1 to 10 mV/sec. were used, and the current/voltage curves were recorded with an X-Y recorder to calculate the polarization resistance (R_p). A typical small amplitude cyclic voltammogram is given in Fig. 29. Macdonald (19) has emphasized that any time dependent signal can be used to evaluate the impedance of a system if transformation of both the perturbation and response into Laplace space can be accomplished. He assumed an equivalent circuit of Fig. 30 and derived the apparent ($1/R_{app}$) and diagonal ($1/R_d$) conductances for a small-amplitude triangular perturbation (Fig. 31) as follows:

$$1/R_{app} = 1/(R_s + R_p) + 2R_p/[R_s (R_s + R_p)(1 + e^{aE_m/vb})] \quad [3]$$

$$1/R_d = 1/(R_s + R_p) + 2V R_p^2 C(e^{aE_m/vb} - 1)/[E_m(R_s + R_p)^2(e^{aE_m/vb} + 1)] \quad [4]$$

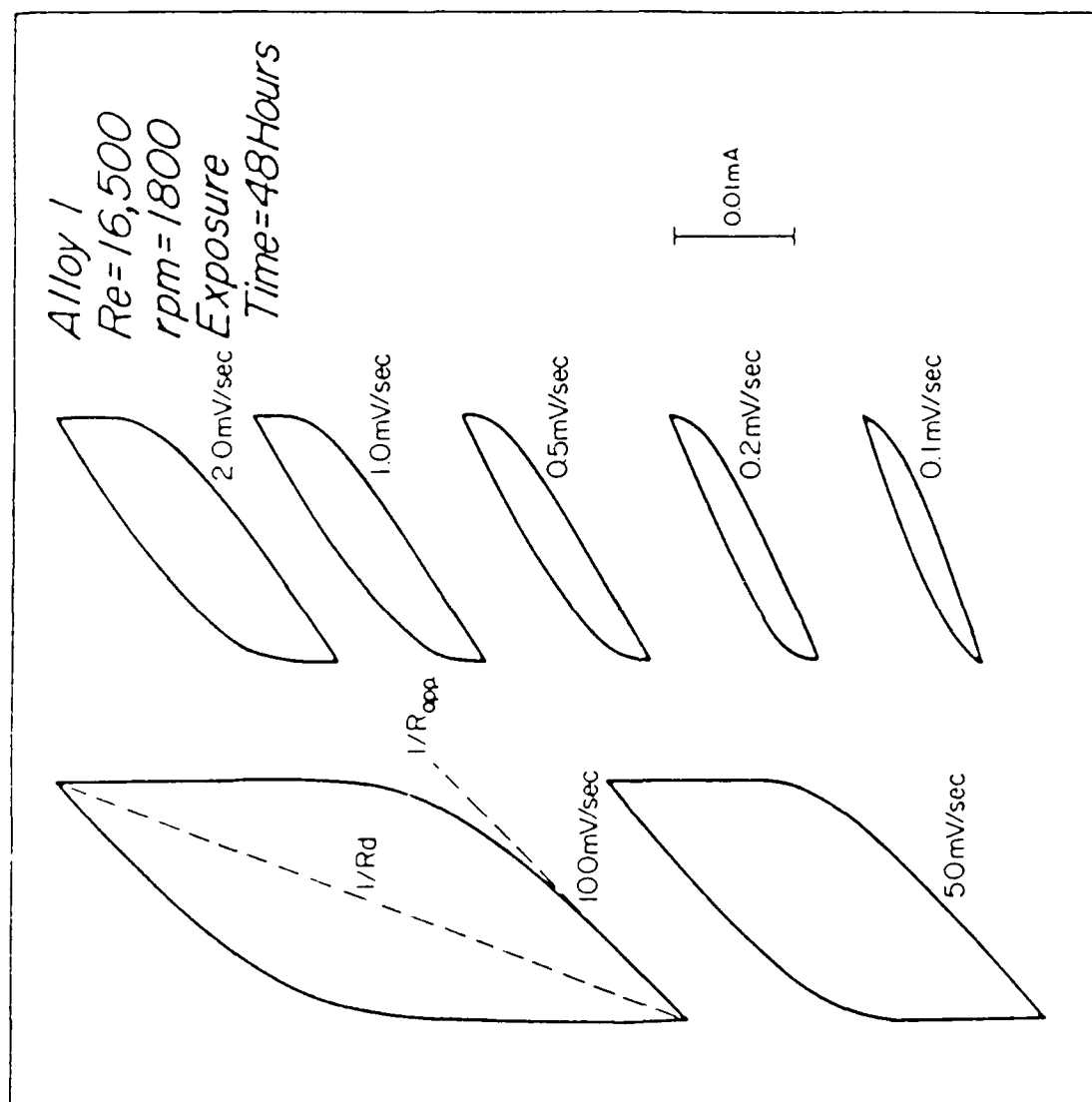


Figure 29: Typical Small Amplitude Cyclic Voltammogram

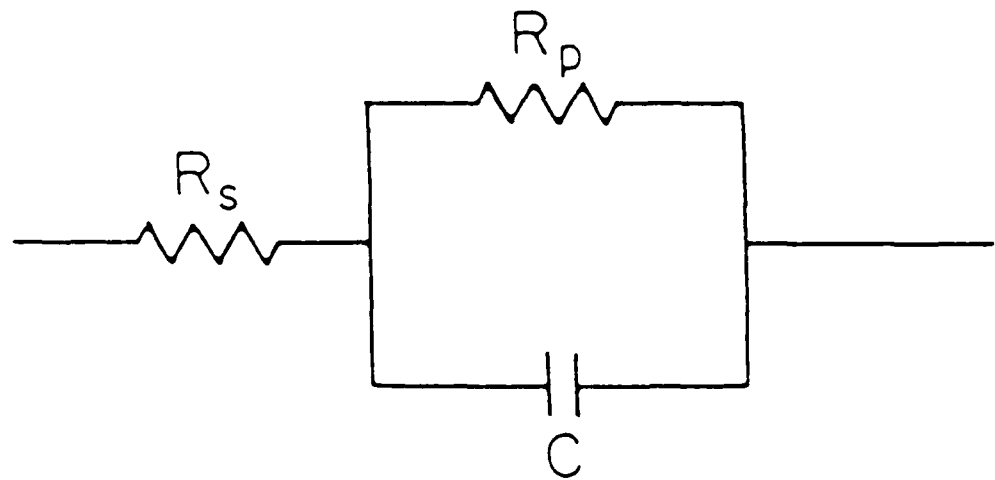


Figure 30: Equivalent circuit for the interface

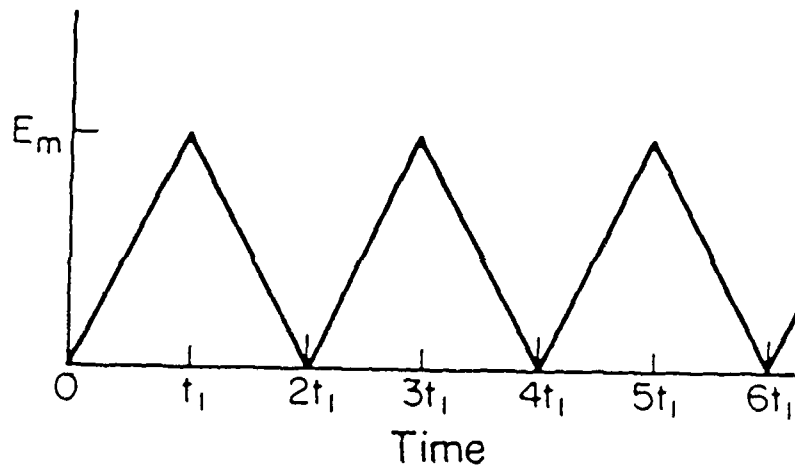


Figure 31: Triangular voltage perturbation function

where R_s is the solution resistance,

R_p is the polarization resistance,

$$a = R_s + R_p,$$

$$b = R_s R_p C,$$

E_m = amplitude of the voltage perturbation (peak-to-peak value),

v is the voltage sweep rate, and

C is the double layer capacitance.

Both $1/R_{app}$ and $1/R_d$ are dependent on the voltage sweep rate because the polarization resistance is shunted by the capacitor C . As indicated in equations [3] and [4], both $1/R_{app}$ and $1/R_d$ approach the inverse of total d-c resistance of the equivalent circuit $1/(R_s + R_p)$ at low sweep rates.

Fig. 32 shows a typical $1/R_{app}$ and $1/R_d$ versus voltage sweep rate curves. In our studies, the value of R_s is very small compared to that of R_p ; therefore, the low sweep rate limit ($v = 0$) is taken as the value of $1/R_p$ as shown in Fig. 32.

Stern and Geary (20) have shown that $1/R_p$ is directly proportional to the corrosion current (i_{corr}):

$$i_{corr} = B_a B_c / [2.303 (B_a + B_c) R_p] \quad [5]$$

where B_a and B_c are the anodic and cathodic Tafel slopes, respectively.

The corrosion rate was then plotted, in terms of $1/R_p \cdot 1/A$, as a function of exposure time in Figures 33 to 35 and Figures 36 to 38 at different rotation speeds (rpm = 600, 1200, and 1800) for Alloy 1 and Alloy 4, respectively. For each alloy at each rotation speed studied, the corrosion rate fluctuated in the first few hours of exposure (~ 10 hours) but became nearly constant after 40 hours of exposure.

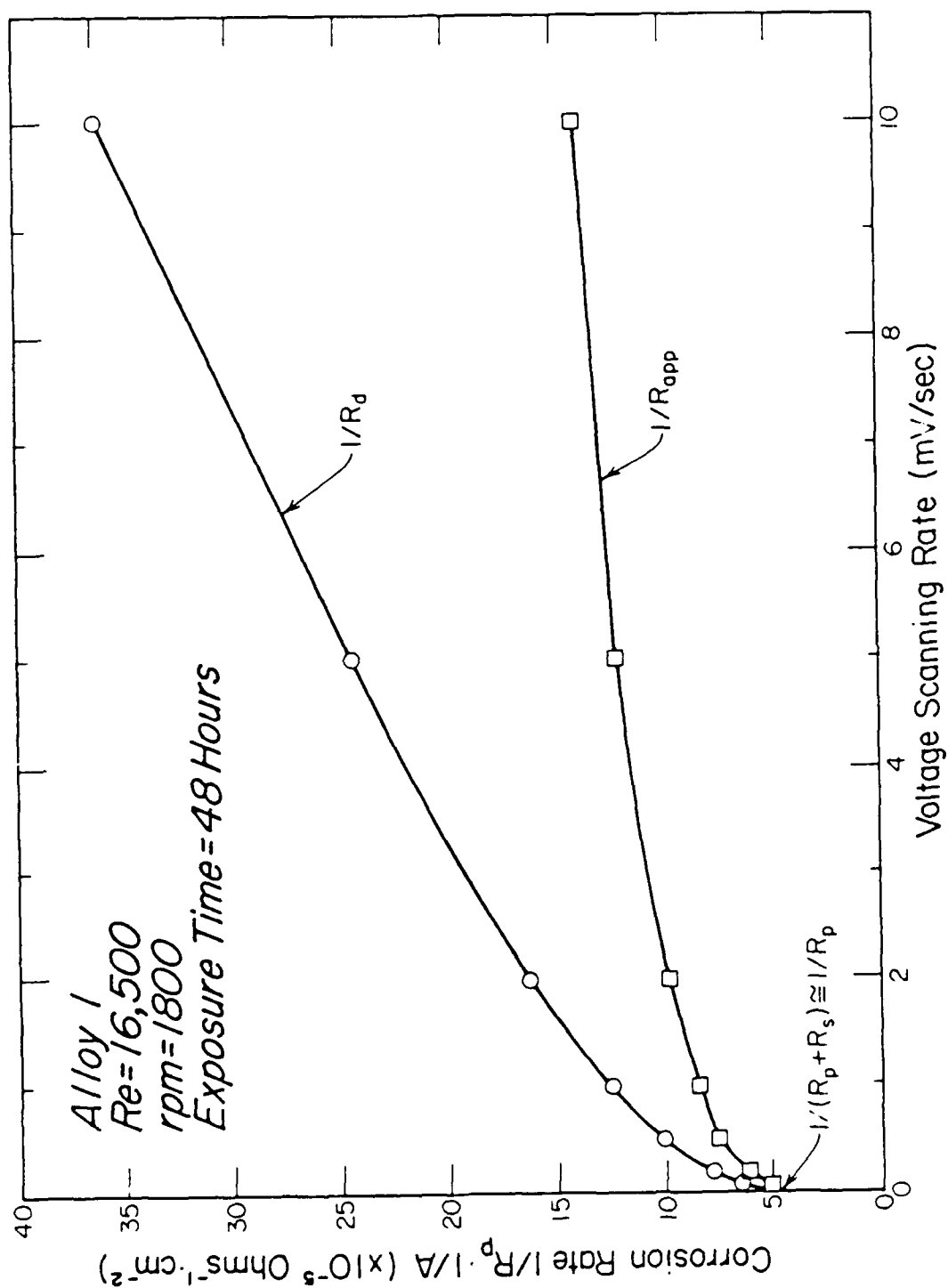


Figure 32: Typical $1/R_{app}$ and $1/R_d$ vs. Voltage scanning rate curves

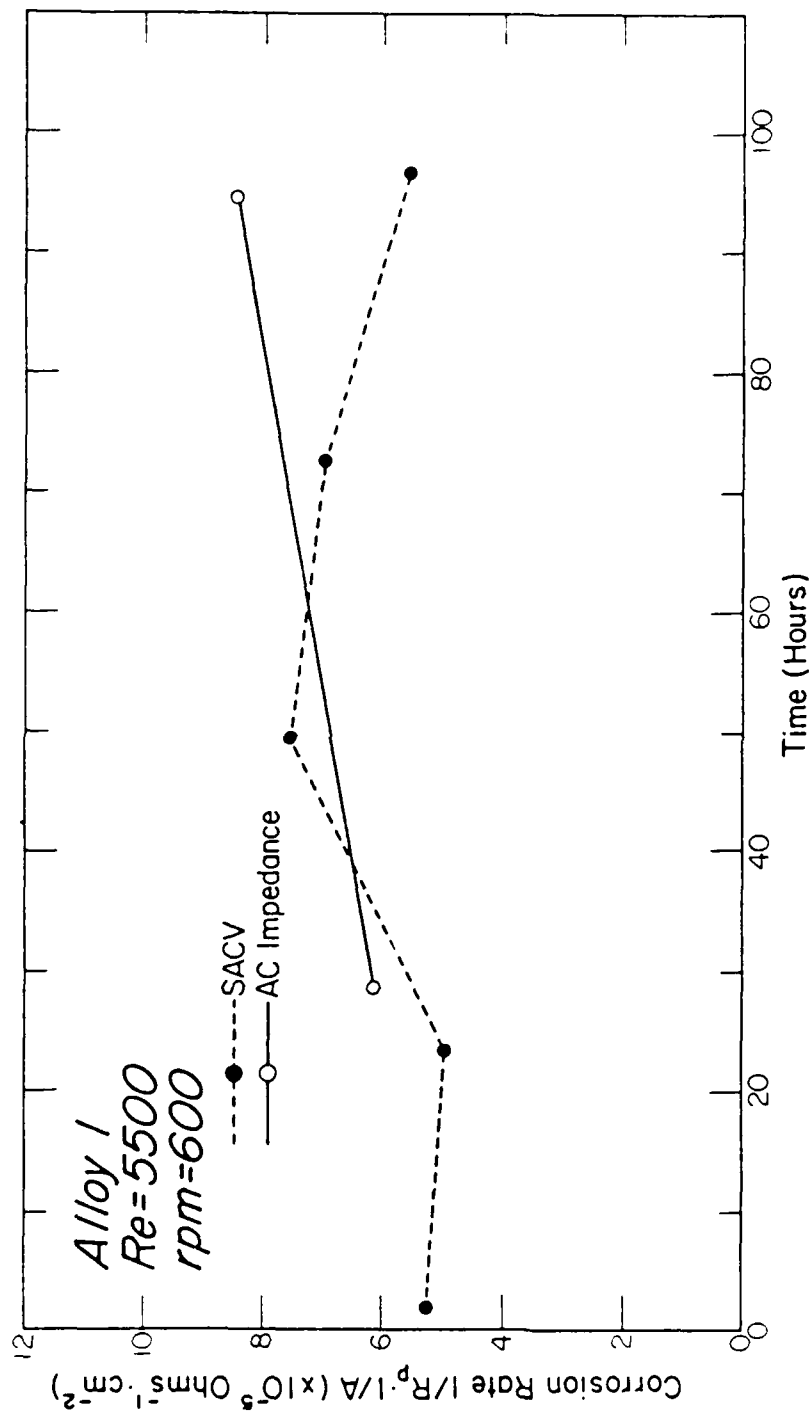


Figure 33: Corrosion rate (as $1/R_p \cdot 1/A$) vs. exposure time curves for Alloy 1 at rpm = 600.

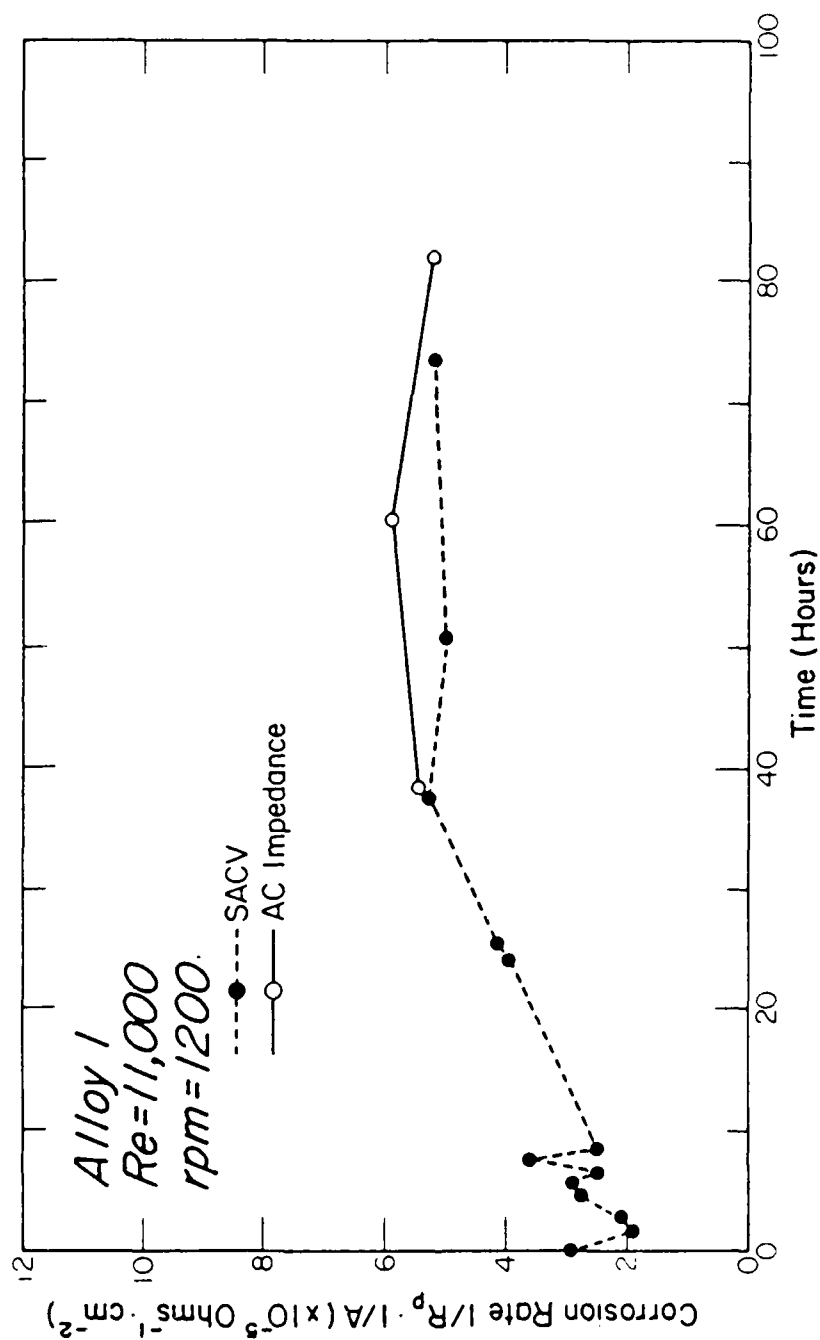


Figure 34: Corrosion rate (as $1/R_p \cdot 1/A$) vs. exposure time curves for Alloy 1 at rpm = 1200

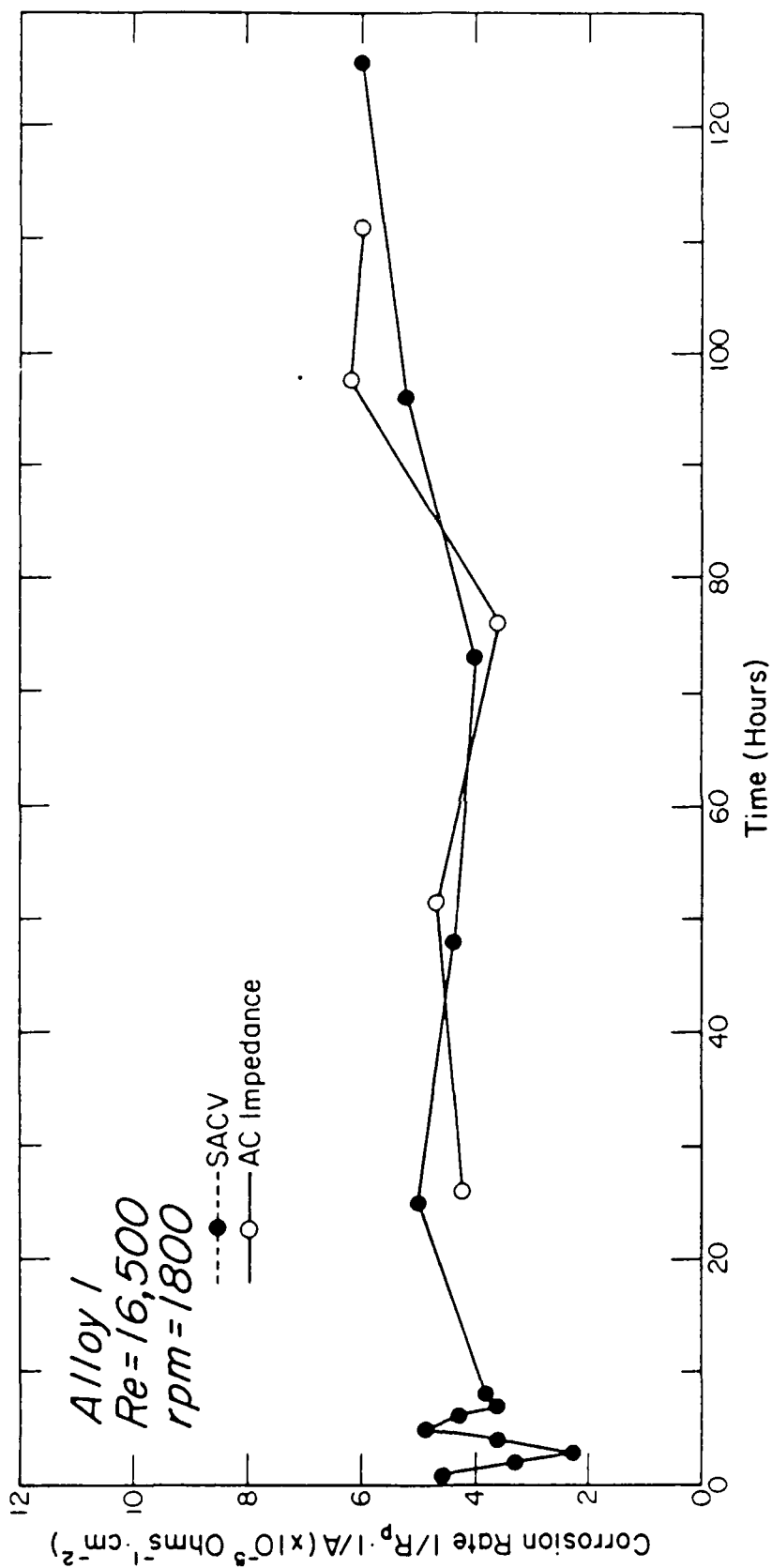


Figure 35: Corrosion rate (as $1/R_p \cdot 1/A$) vs. exposure time curves for alloy 1 at rpm = 1800

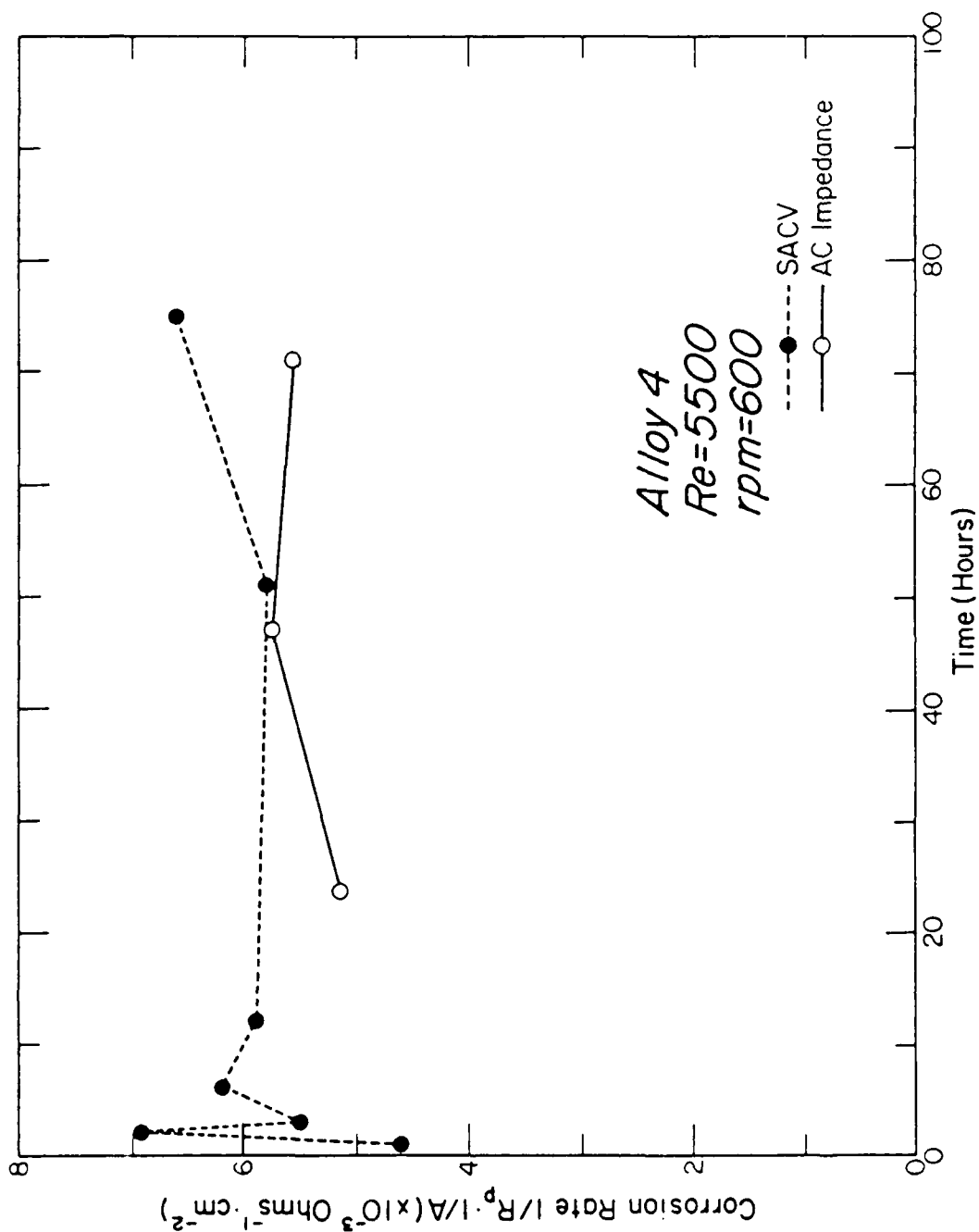


Figure 36: Corrosion rate (as $1/R_p \cdot 1/A$) vs. exposure time curves for Alloy 4 at rpm = 600.

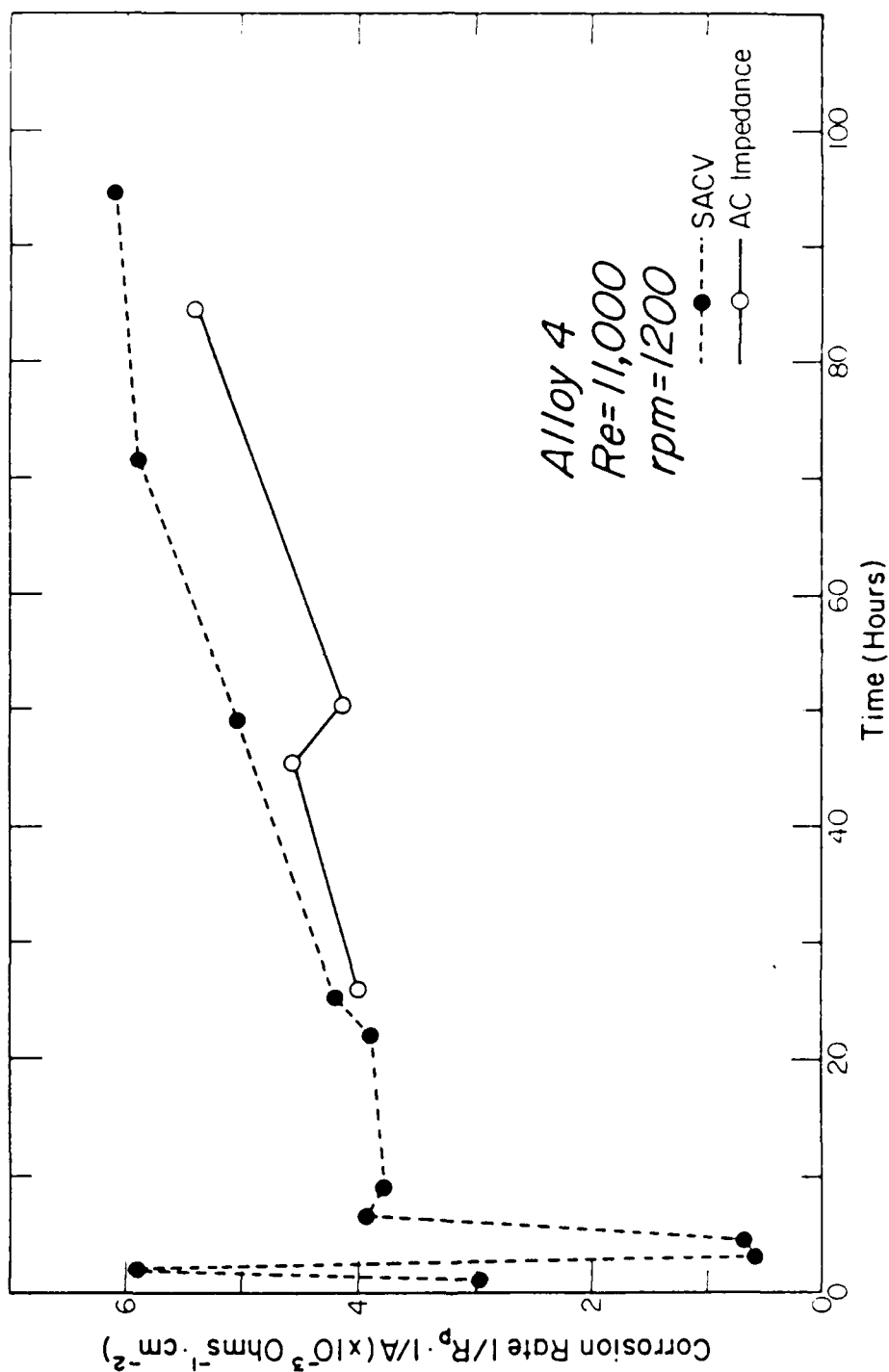


Figure 37: Corrosion rate (as $1/R_p \cdot 1/A$) vs. exposure time curves for Alloy 4 at rpm = 1200

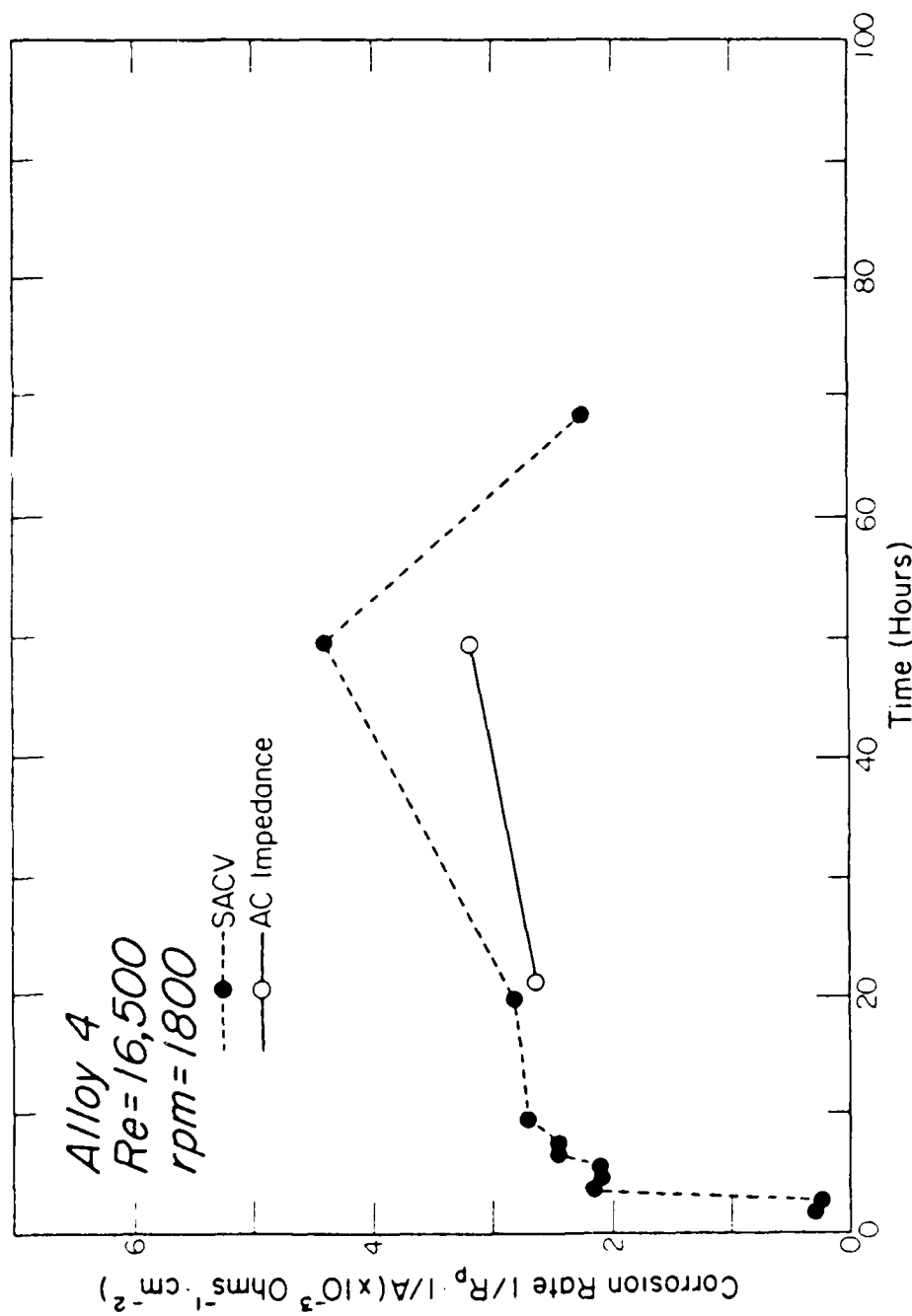


Figure 38: Corrosion rate (as $1/R_p \cdot 1/A$) vs. exposure time curves for Alloy 4 at rpm = 1800.

AC Impedance

AC impedance data was generated as a function of frequency (10^4 Hz to 10^{-3} Hz or lower) by imposing a 20 mV peak-to-peak sinusoidal voltage signal across the interface at the corrosion potential. The complex impedance data was acquired using a frequency response analyzer (Solartron Model 1172) driven by an Apple IIe microcomputer.

The total impedance of the equivalent circuit shown in Fig. 30 is:

$$Z = R_s + \frac{1}{1/R_p + 1/j\omega C} = R_s + \frac{R_p j\omega C}{R_p + j\omega C} \quad [6]$$

where $j = \sqrt{-1}$ and ω is the angular frequency of the voltage perturbation.

Equation [6] can further be simplified as

$$\begin{aligned} Z &= R_s + \frac{R_p \omega^2 C^2}{R_p^2 + \omega^2 C^2} - \frac{R_p^2 \omega C}{R_p^2 + \omega^2 C^2} j \\ &= Z' + jZ'' \end{aligned} \quad [7]$$

$$\text{where } Z' = R_s + \frac{R_p \omega^2 C^2}{R_p^2 + \omega^2 C^2} \quad [8]$$

$$Z'' = - \frac{R_p^2 \omega C}{R_p^2 + \omega^2 C^2} \quad [9]$$

From Equations [8] and [9], it can be found that

$$(Z' - R_s - \frac{R_p}{2})^2 + Z''^2 = (\frac{R_p}{2})^2 \quad [10]$$

Equation (10) represents a semicircle with center located at $(R_s + \frac{R_p}{2}, 0)$ if the real component (Z') or Z is plotted against the negative value of the imaginary component ($-Z''$) of Z on a complex impedance diagram (Fig. 39).

As indicated in Equation (7), the total impedance of the equivalent circuit Z is dependent on the frequency of the voltage excitation. While Z tends toward the total d-c impedance of the circuit ($R_s + R_p$) at low frequencies, it approaches R_s at high frequencies. This result parallels the behavior observed in SACV.

Figures 40 to 42 and Figures 43 to 45 show the complex impedance diagrams at various rotation speeds and exposure times for Alloy 1 and Alloy 4, respectively. For both alloys, at each rotation speed, the value of high frequency limit (R_s) is very small compared to the value of low frequency limit ($R_p + R_s$); therefore, the value of the low frequency limit was taken as the polarization resistance R_p . The corrosion rate obtained by AC impedance technique (as $1/R_p$ $1/A$) was then plotted against exposure time. They are included in Figures 33 to 38 for comparison. It can be seen that good agreement was obtained between SACV and AC impedance techniques for the measurement of polarization resistance.

Corrosion Potential Measurements

Figures 46 to 48 and Figures 49 to 51 show the variation of corrosion potential (E_{corr}) with exposure time at different rotation speeds for Alloy 1 and Alloy 4, respectively. For both alloys, at each rotation speed studied, the corrosion potential first decreased (more negative) with exposure time but subsequently became relatively constant after about 40 hours of exposure.

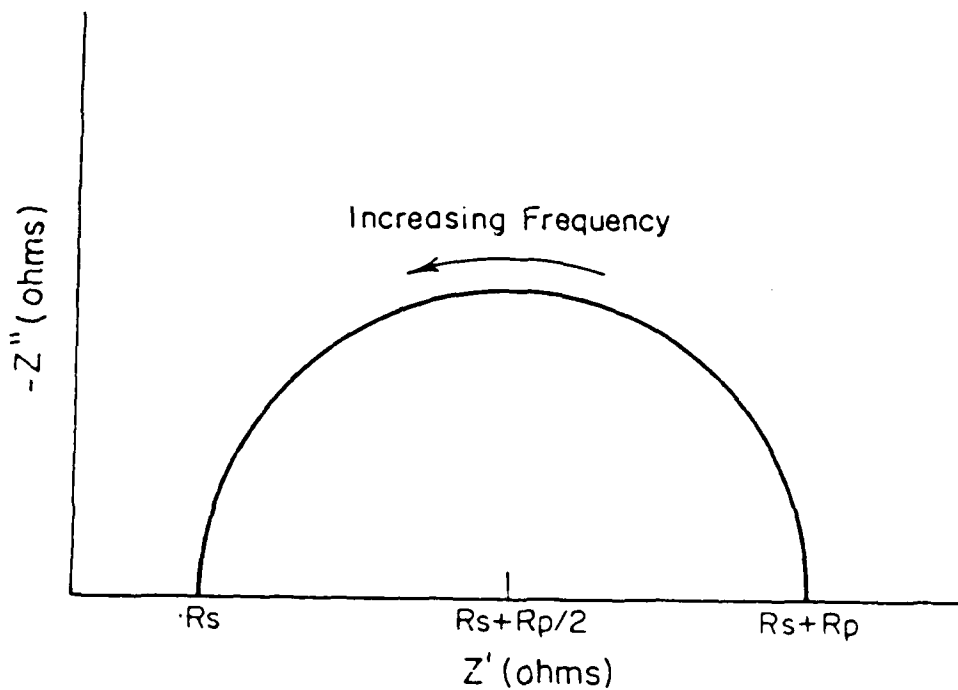


Figure 39: Complex impedance diagram for the equivalent circuit shown in Figure 32.

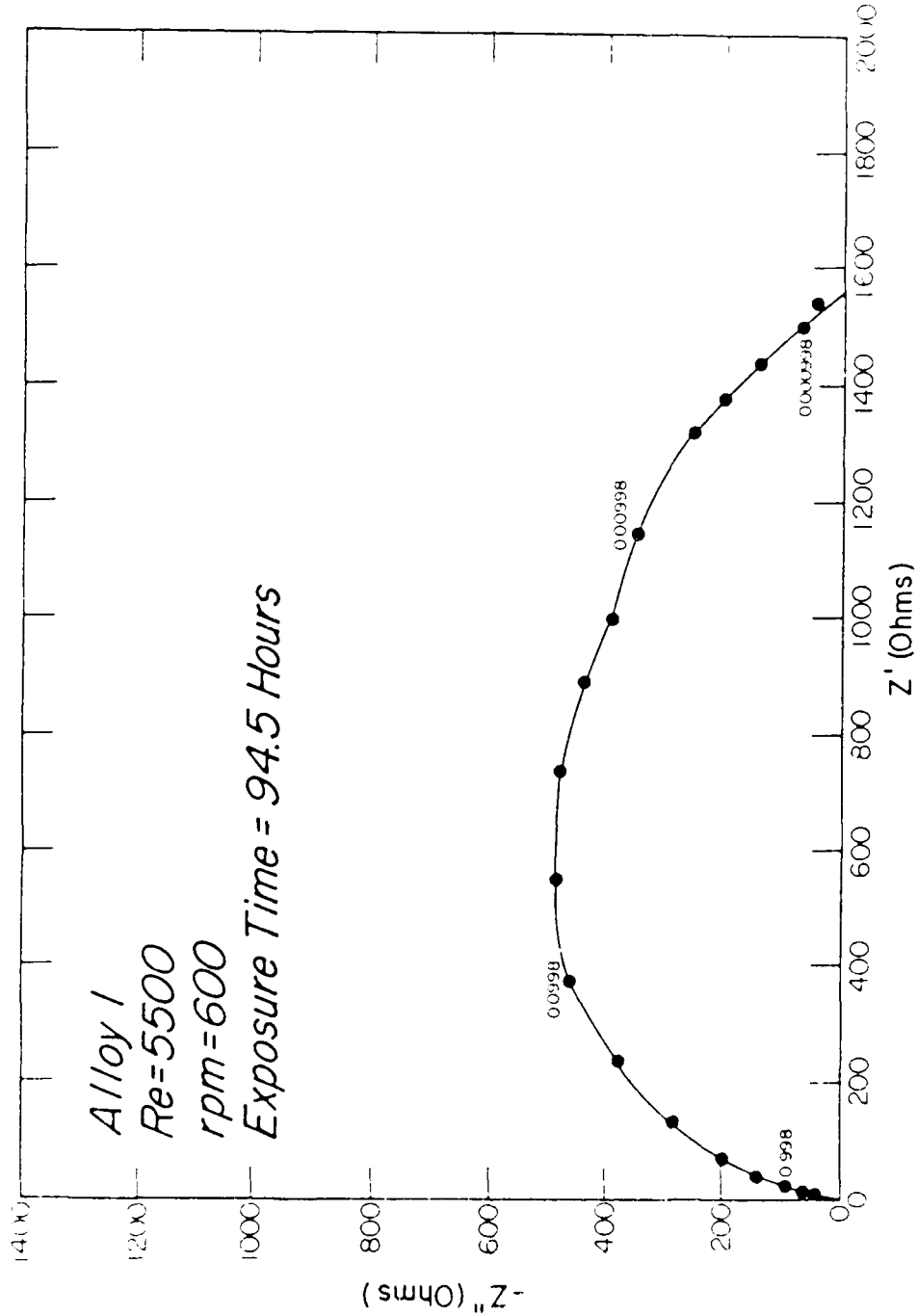
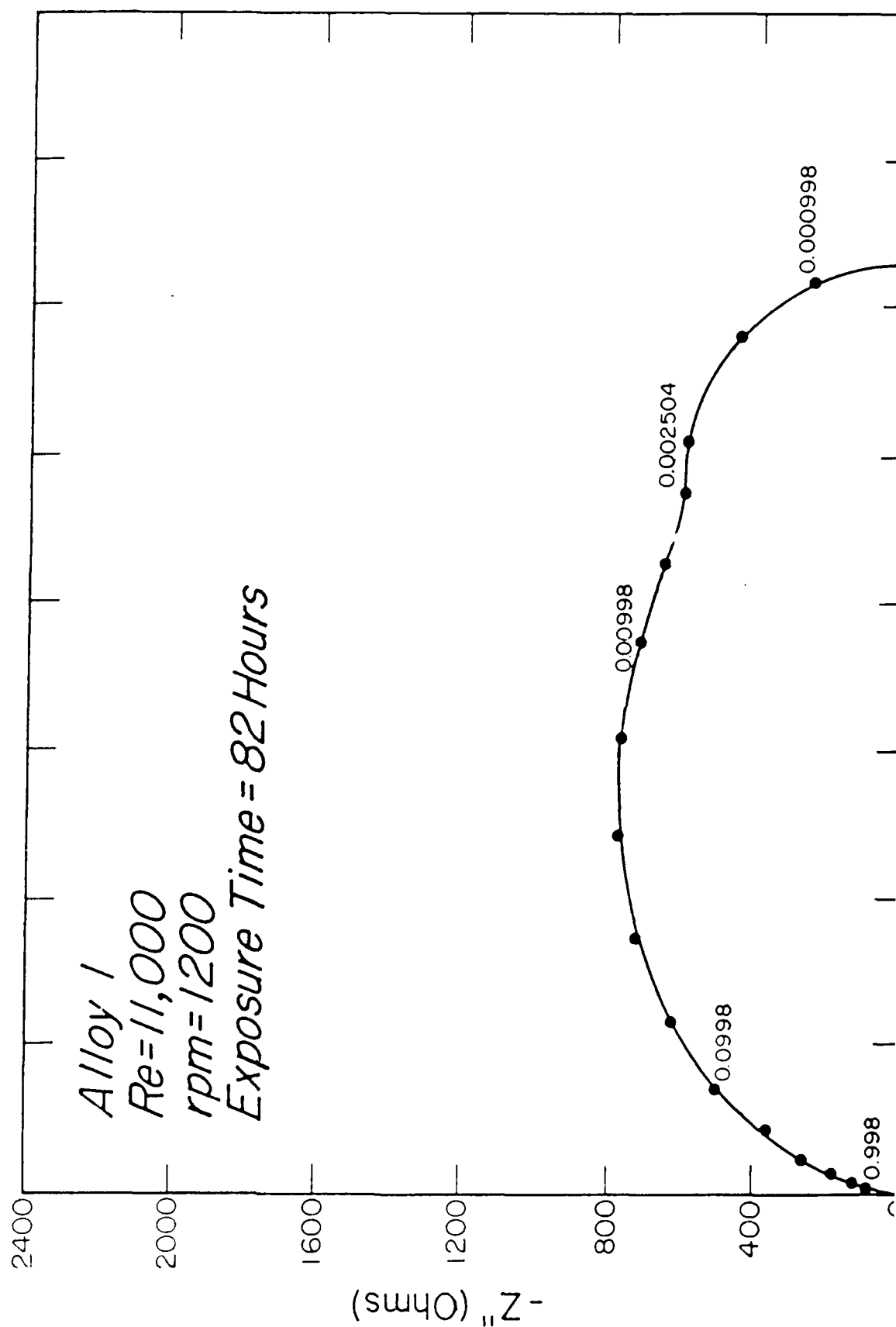


Figure 40: Complex impedance diagram for Alloy 1 at rpm = 600.
The numbers next to the points indicate the frequency in Hz.



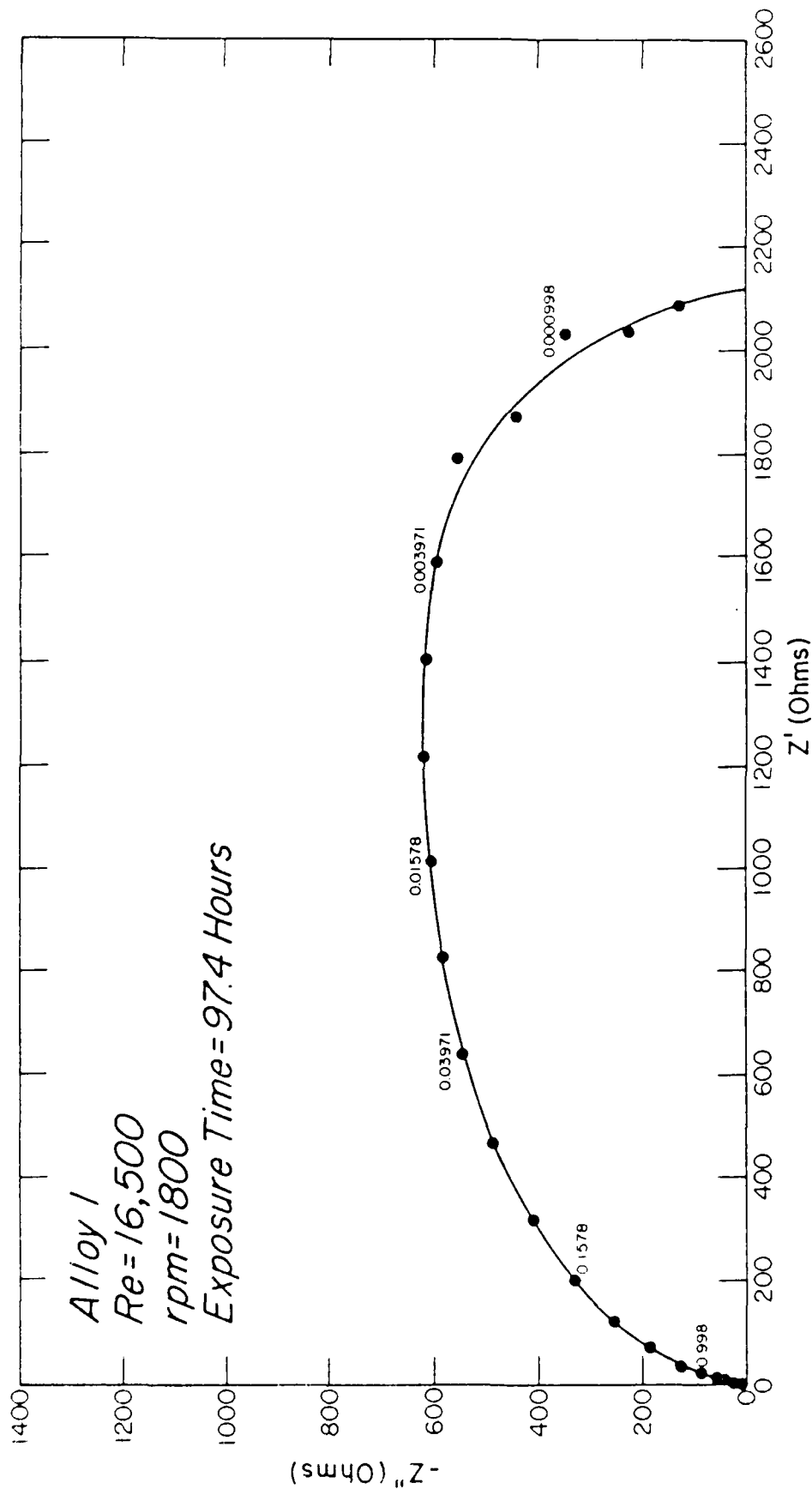


Figure 42: Complex impedance diagram for Alloy 1 at rpm = 1800.
The numbers next to the points indicate the frequency in Hz.

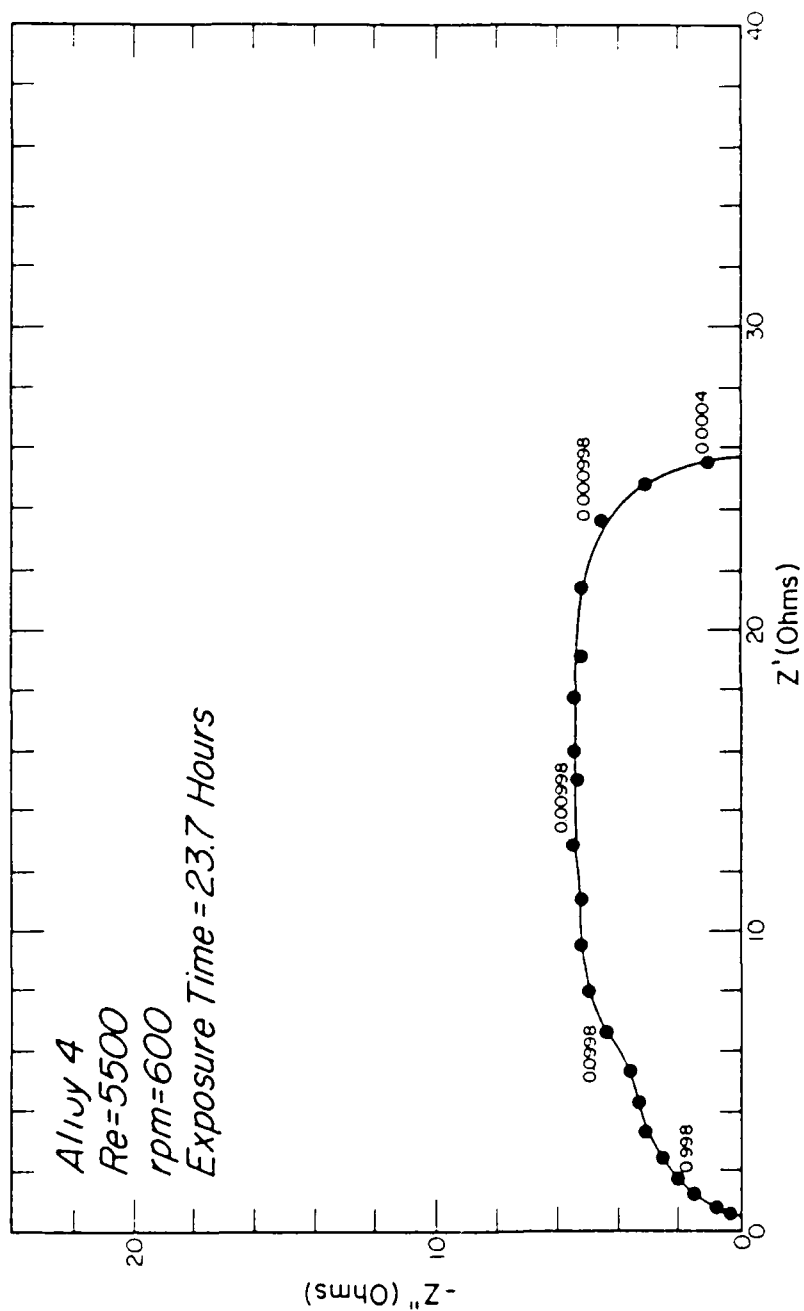


Figure 43: Complex impedance diagram for Alloy 4 at rpm = 600.
The numbers next to the points indicate the frequency in Hz.

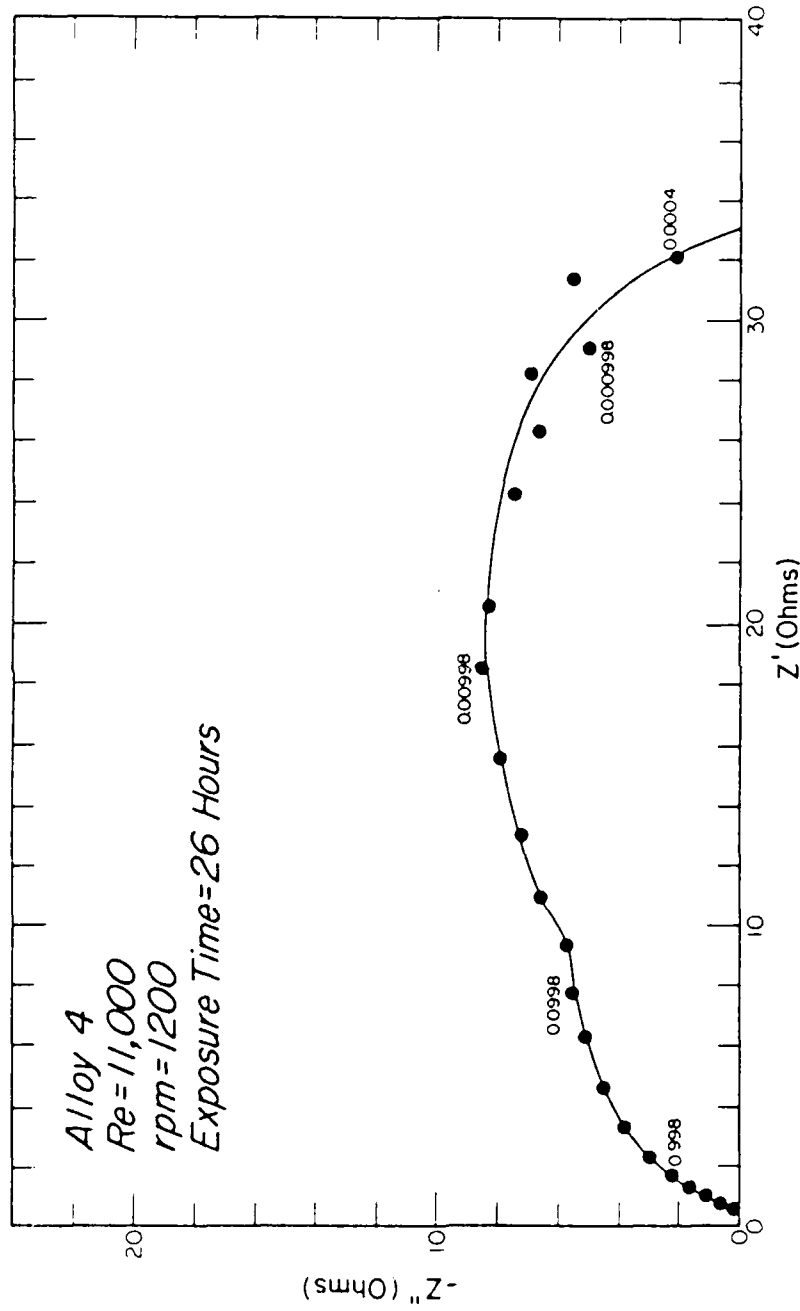


Figure 44: Complex impedance diagram for Alloy 4 at rpm = 1200.
The numbers next to the points indicate the frequency in Hz.

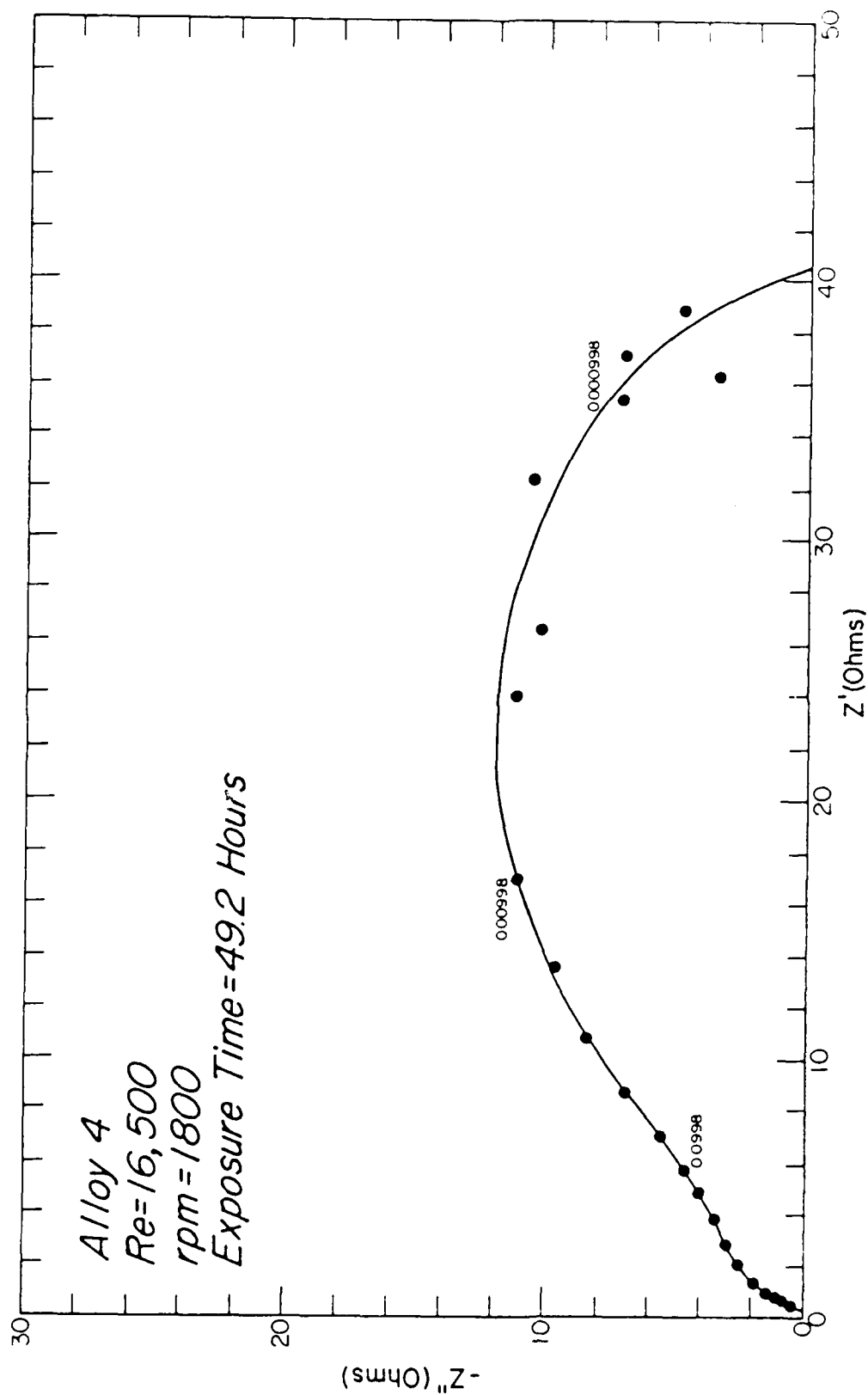


Figure 45: Complex impedance diagrams for Alloy 4 at rpm = 1800.
The numbers next to the points indicate the frequency in Hz.

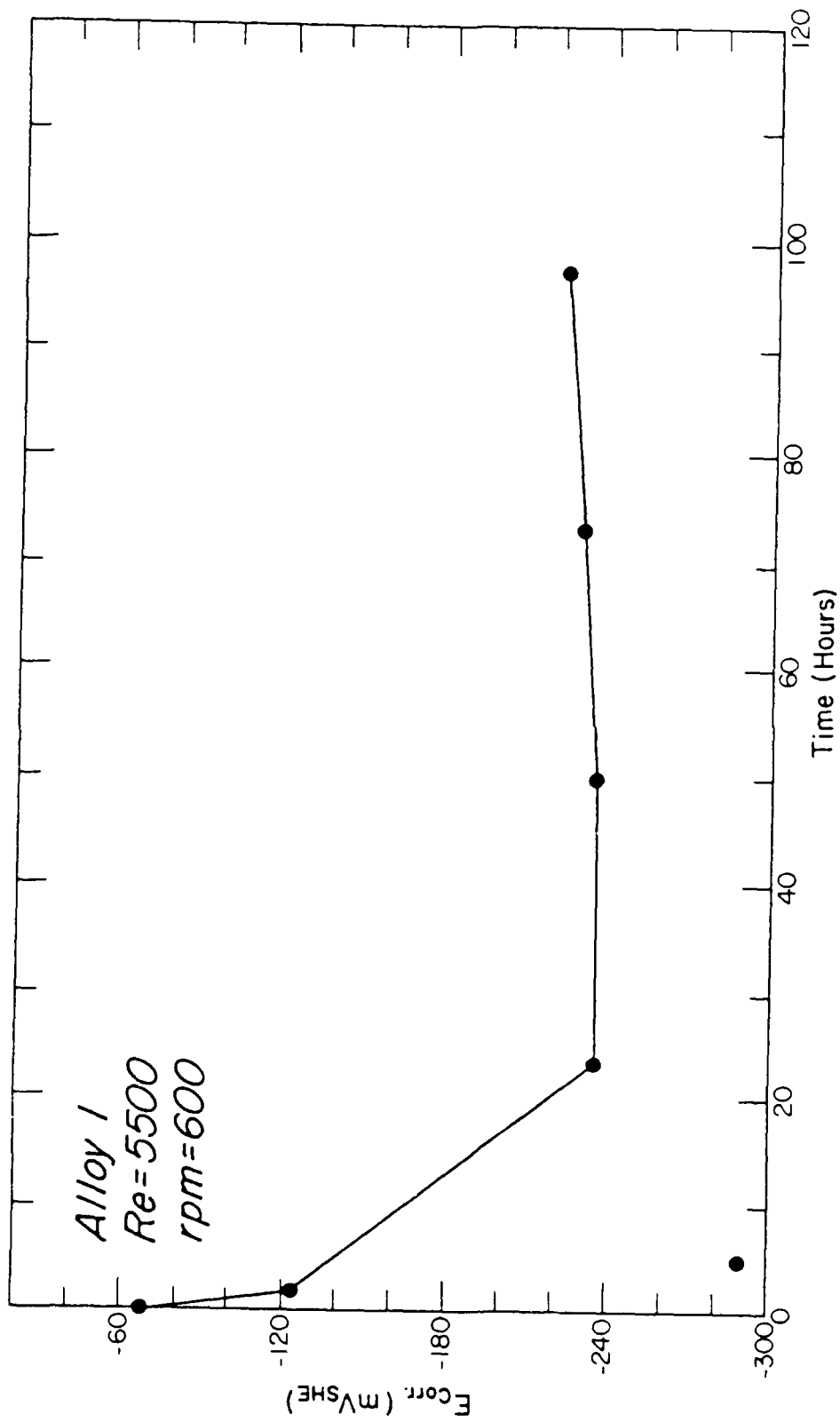


Figure 46: Variation of corrosion potential with exposure time for Alloy 1 at rpm = 600.

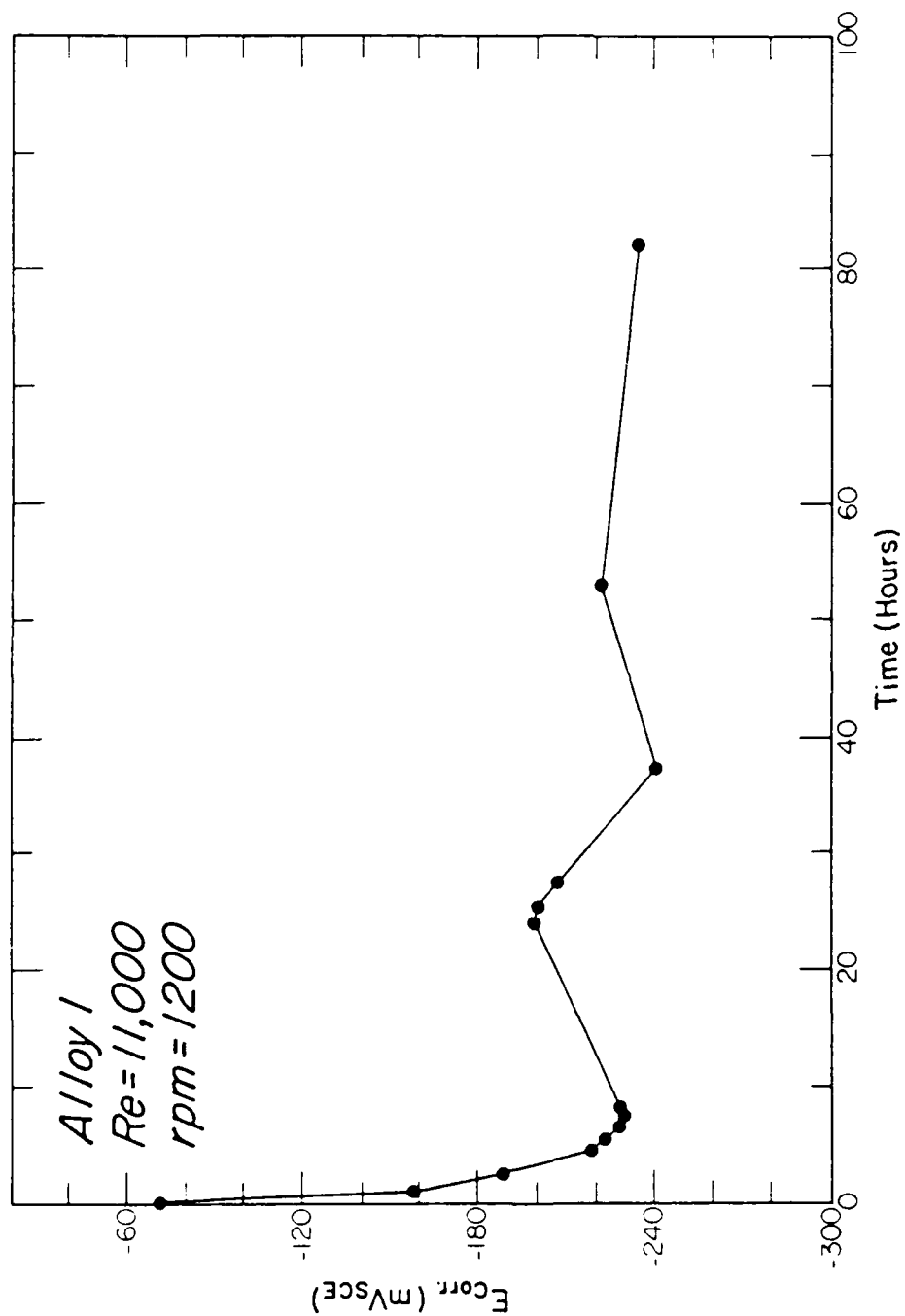


Figure 47: Variation of corrosion potential with exposure time for Alloy 1 at rpm = 1200.

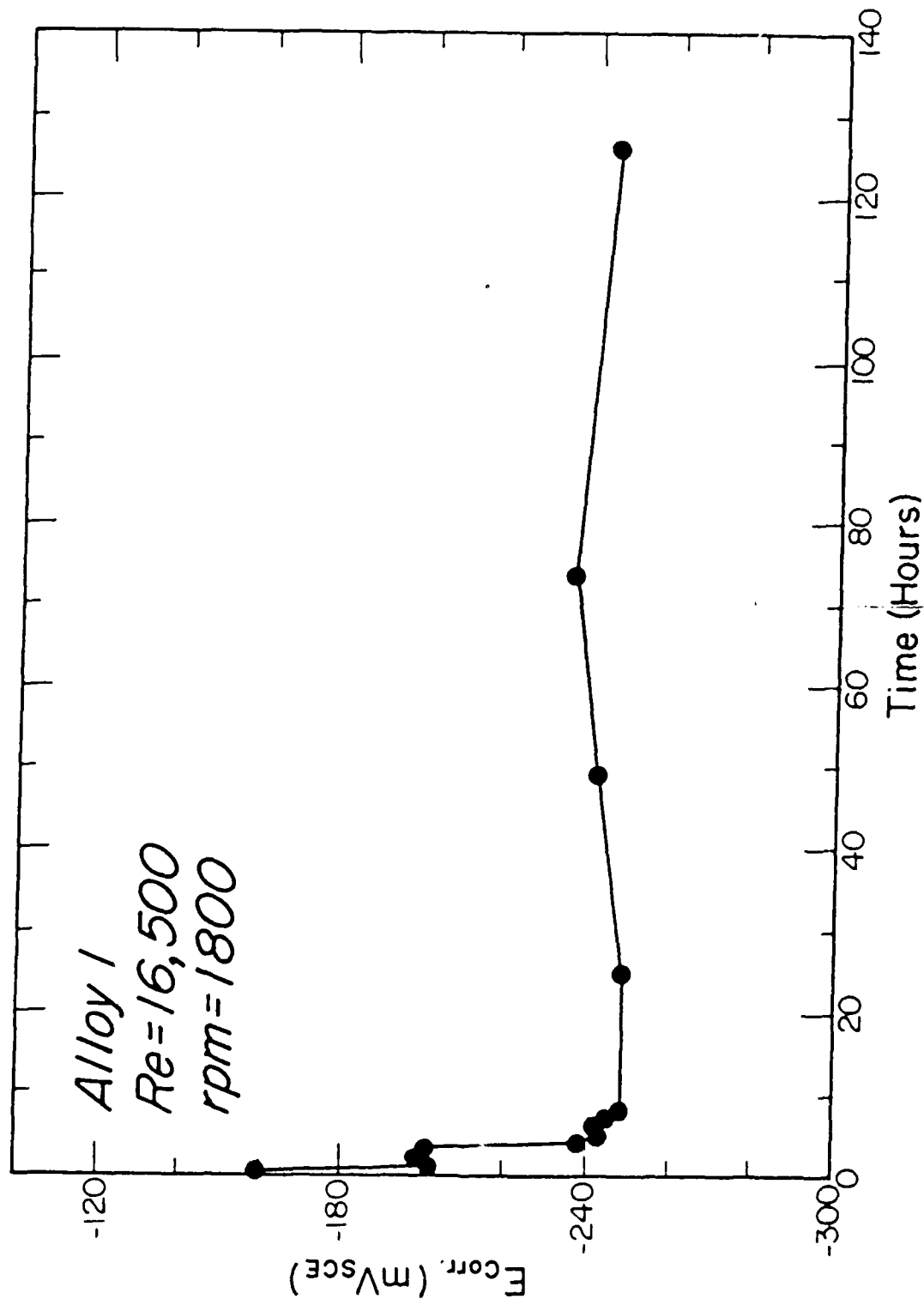


Figure 48: Variation of corrosion potential with exposure time for Alloy 1 at rpm = 1800.

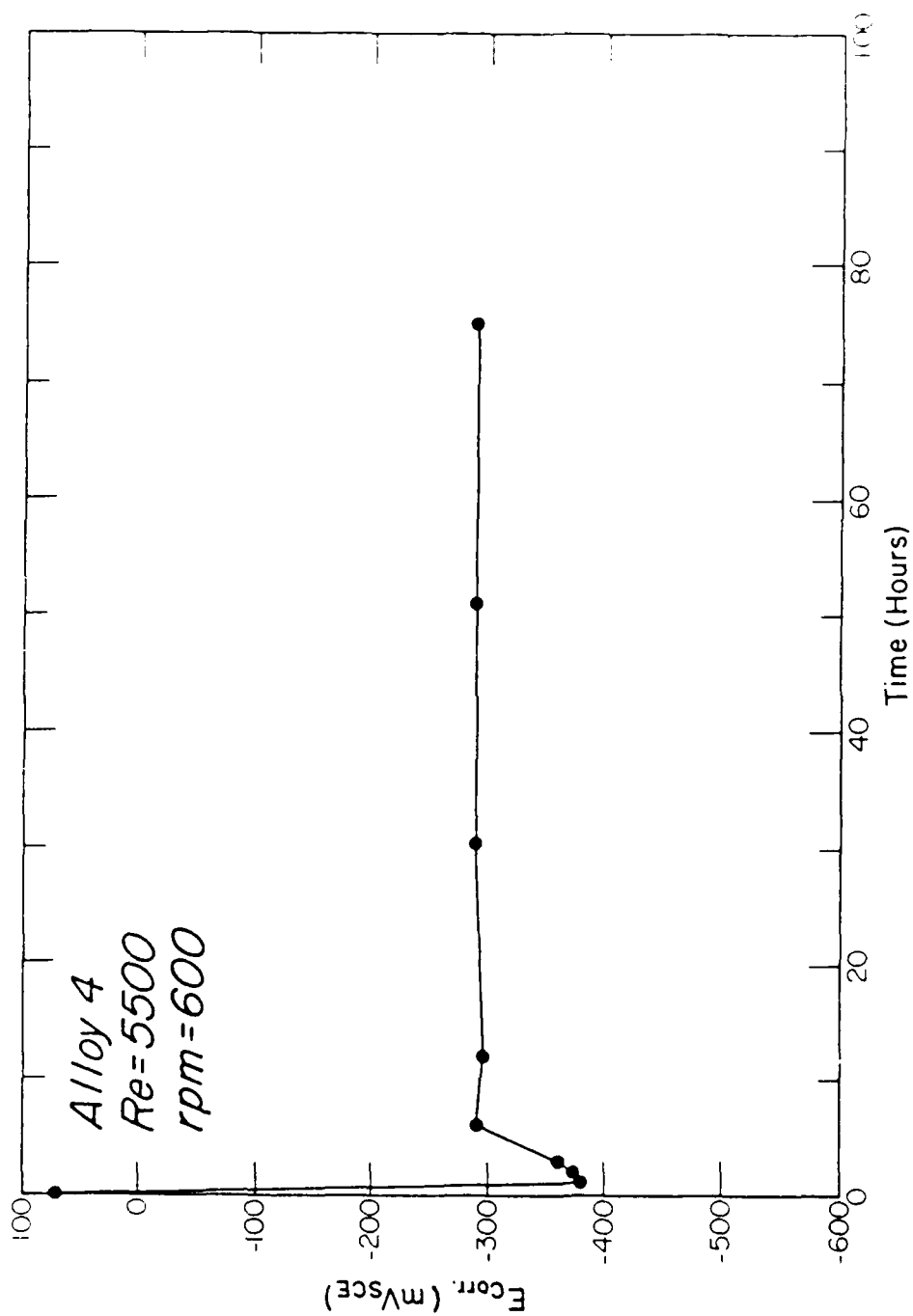


Figure 49: Variation of corrosion potential with exposure time for Alloy 4 at rpm = 600.

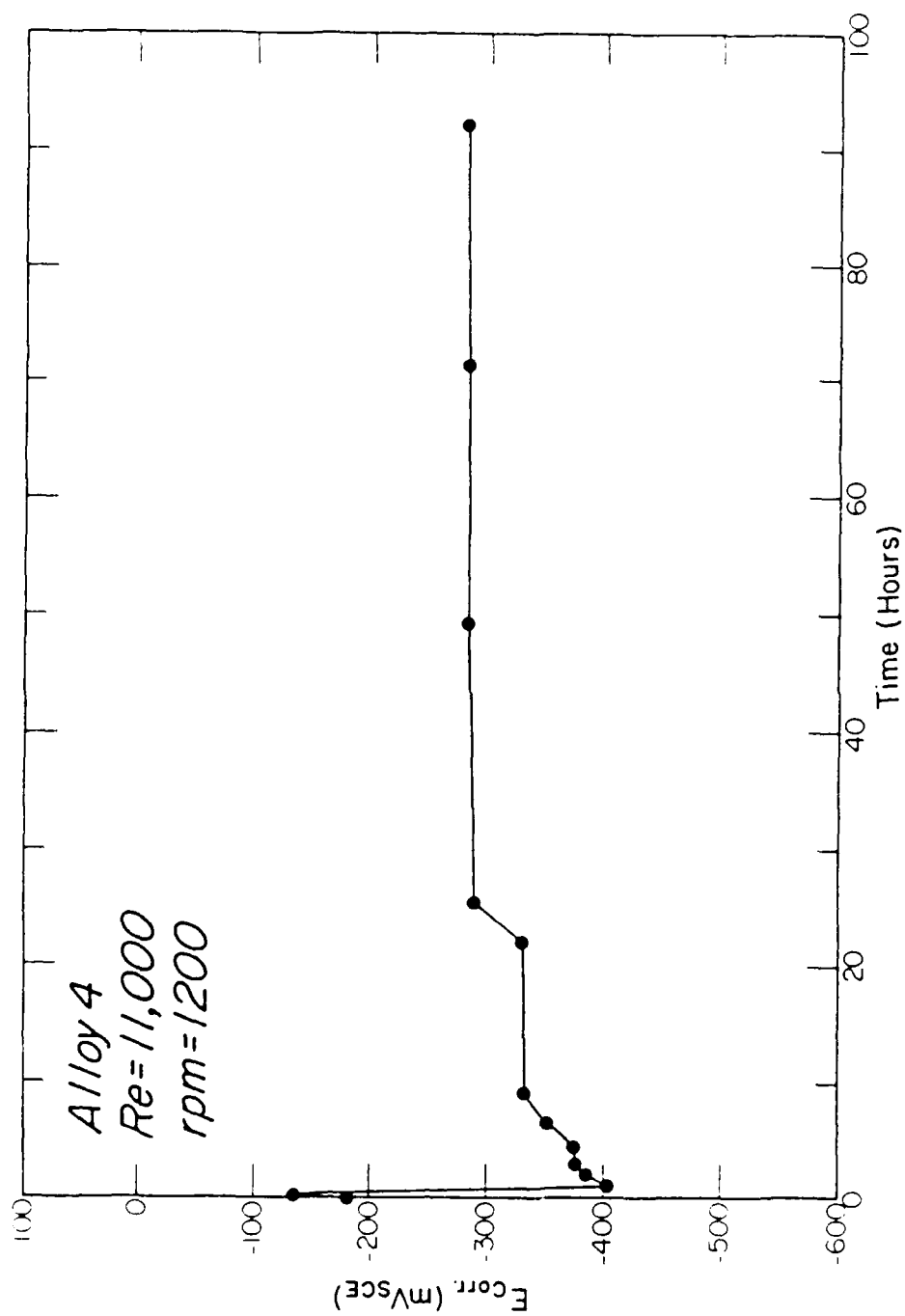


Figure 50: Variation of corrosion potential with exposure time for Alloy 4 at rpm = 1200.

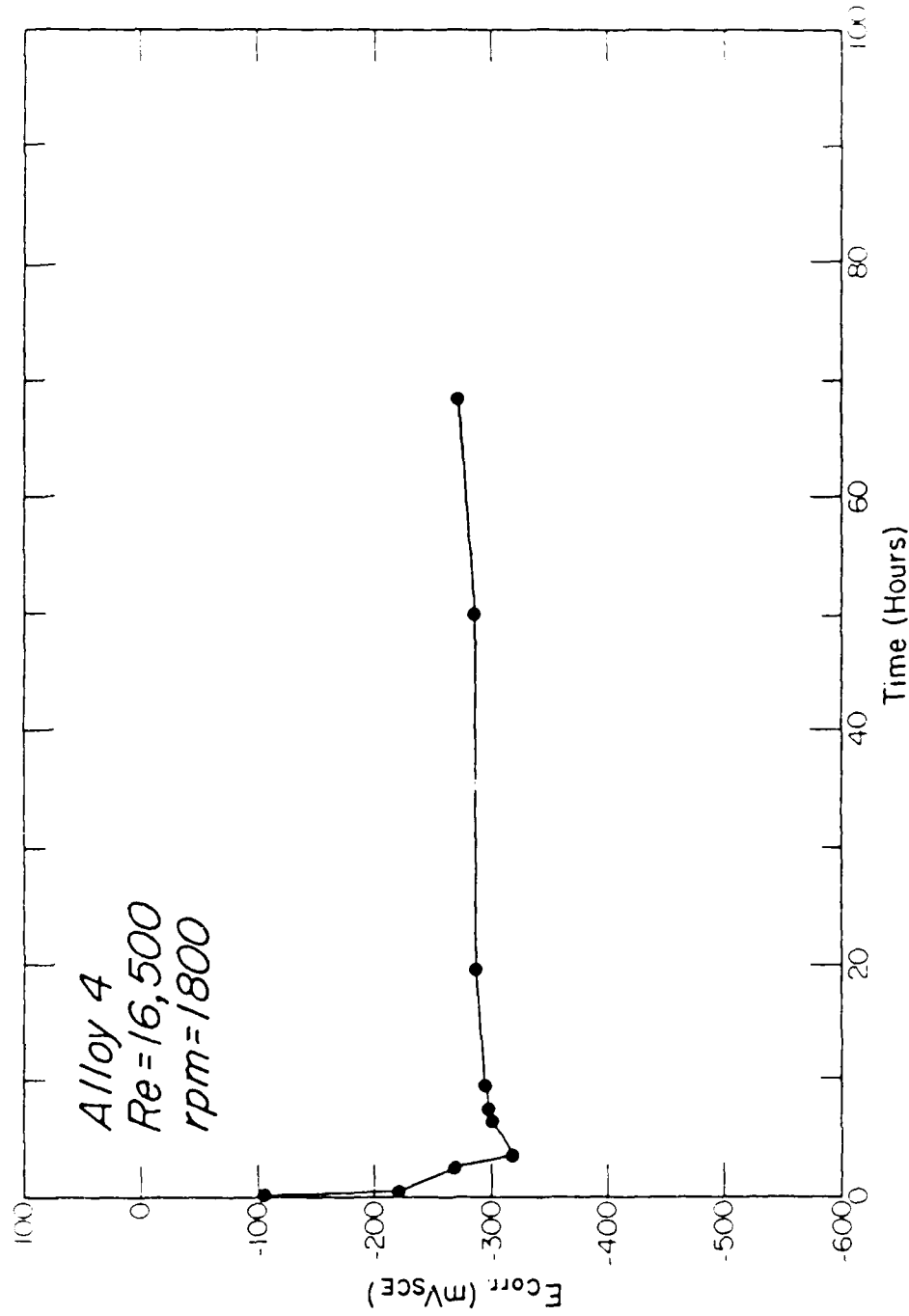


Figure 51: Variation of corrosion potential with exposure time for Alloy 4 at rpm = 1800.

Effect of Hydrodynamics on Corrosion

The effect of hydrodynamics on corrosion can be expressed using the dimensionless Reynolds number (Re) which is related to the relative fluid velocity by

$$Re = dv/\mu \quad [11]$$

where d is the outside diameter of the specimen,

v is the peripheral velocity of the rotating electrode, and

μ is the kinematic viscosity of the solution.

For d = 1.905 cm and $\mu = 1.036 \times 10^{-2} \text{ cm}^2/\text{sec}$. (1 N HCl solution), the corresponding Reynolds numbers at 600 rpm, 1200 rpm, and 1800 rpm are 5500, 11000, and 16500, respectively.

The corrosion potentials (E_{corr}) and the corrosion rates ($1/R_p \cdot 1/A$) measured by SACV and AC impedance techniques after 40 hours of exposure were averaged for each rotation speed and then plotted as a function of Reynolds number for each alloy.

For Alloy 1 (Fig. 52), both the averaged corrosion rate and the averaged corrosion potential decrease with increasing Re. However, for Alloy 4 (Fig. 53), the averaged corrosion rate decreases with increasing Re while the averaged corrosion potential increased with increasing Re.

Potentiodynamic Polarization Curves

Potentiodynamic polarization curves were obtained by changing the potential, at a voltage scan rate of 30 mV/min., from the corrosion potential into the cathodic region and the anodic region, respectively.

They were measured every 24 hours after 24 hours of exposure. Figures 54 to 56 and Figures 57 to 59 show the potentiodynamic polarization curves for

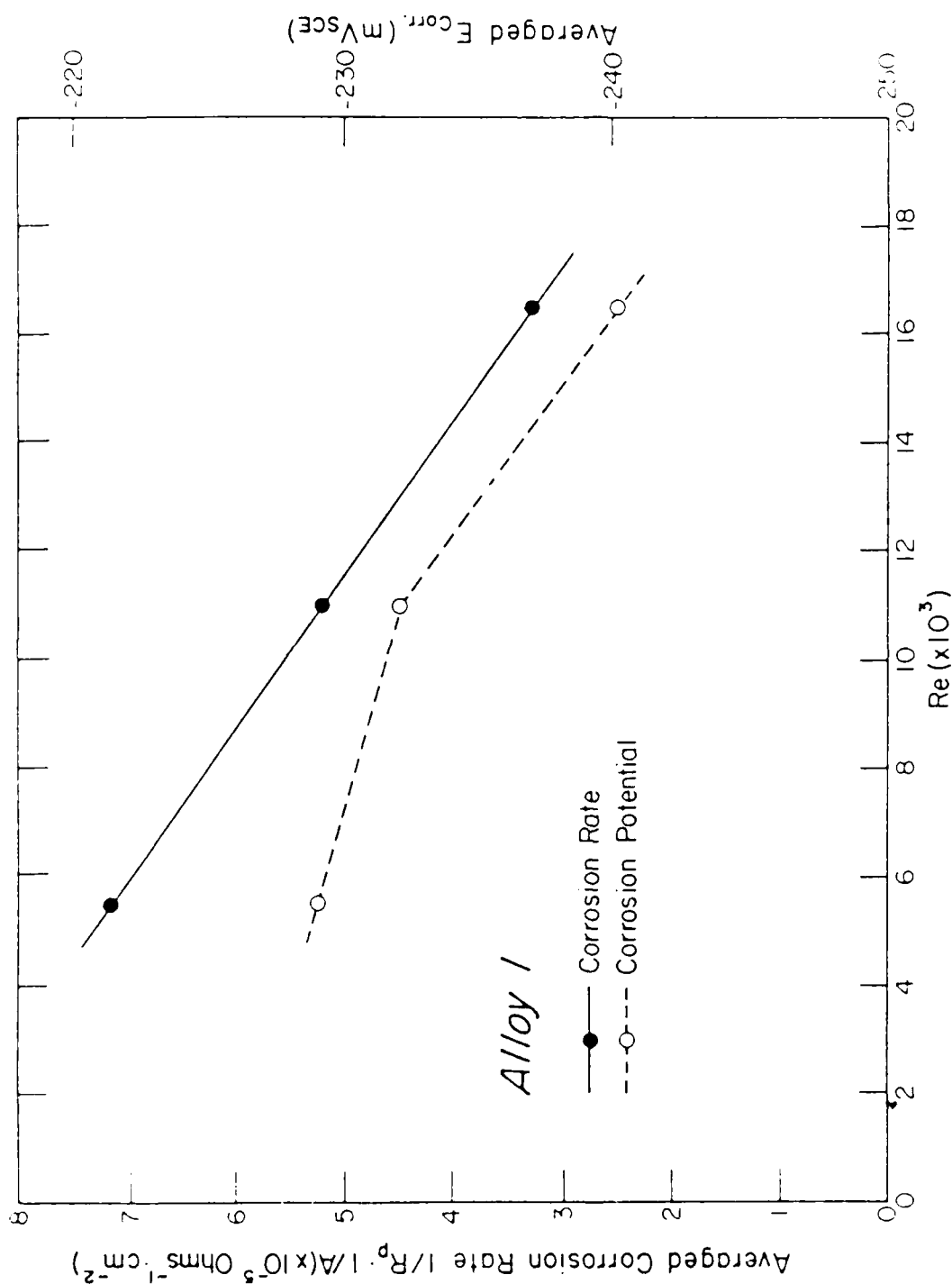


Figure 52: Averaged corrosion rate and corrosion potential vs. Re curves for Alloy 1.

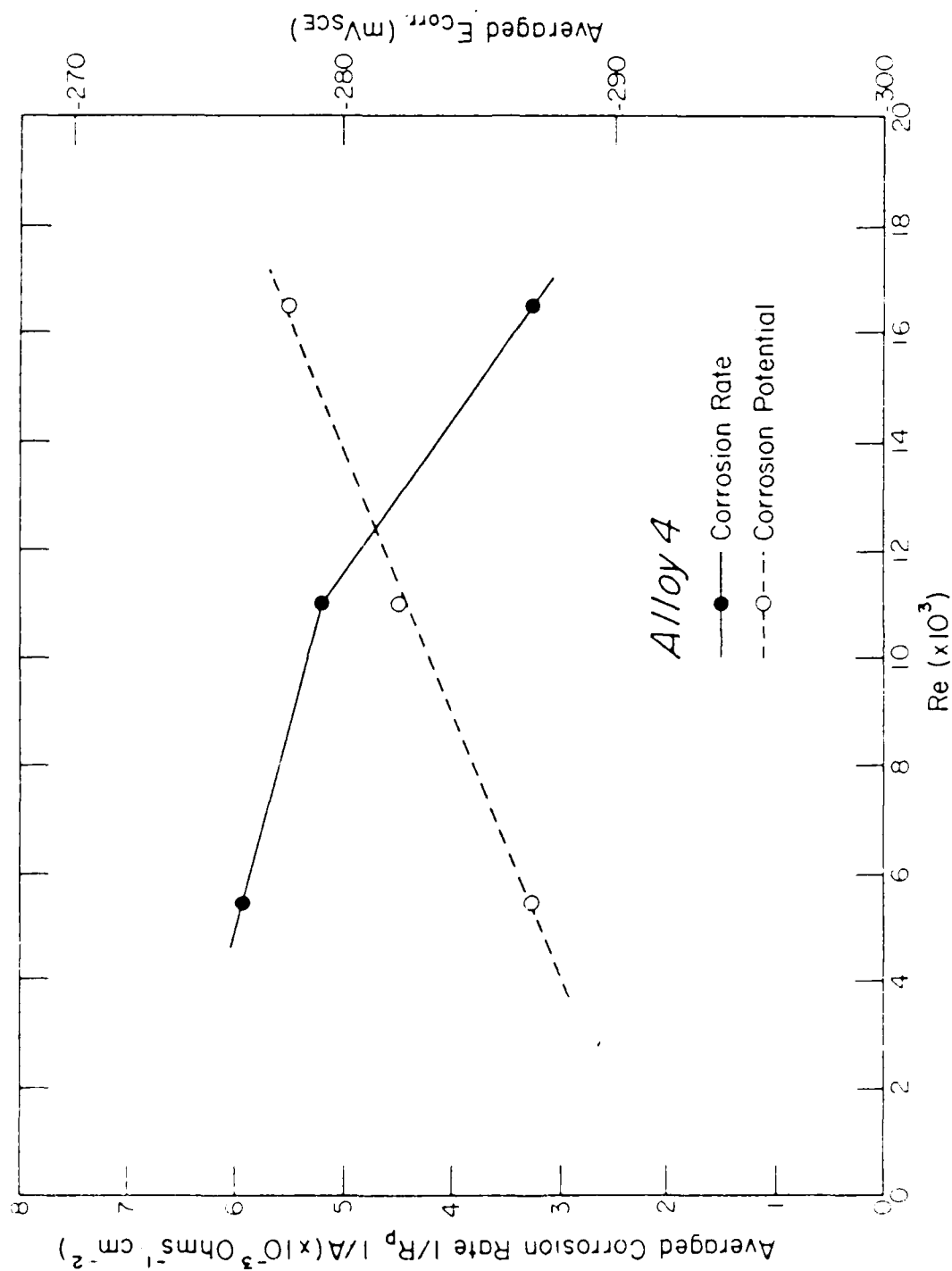


Figure 53: Averaged corrosion rate and corrosion potential vs. Re curves for Alloy 4.

AD-A149 805

STRESS CORROSION CRACKING AND OXIDATION CHARACTERISTICS
OF BORIDE-STRENGTH (U) OHIO STATE UNIV RESEARCH
FOUNDATION COLUMBUS C NOBLE ET AL. 22 OCT 84

2/1

UNCLASSIFIED

OSURF-TR-2 N00014-82-K-0485

F/G 11/6

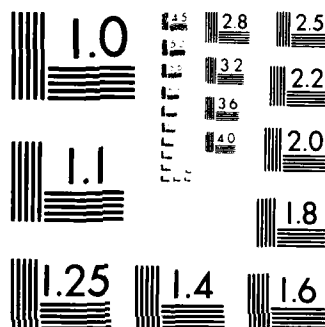
NL

END

1. 411

ENC

Cont



MICROCOPY RESOLUTION TEST CHART
NATIONAL BUREAU OF STANDARDS-1963-A

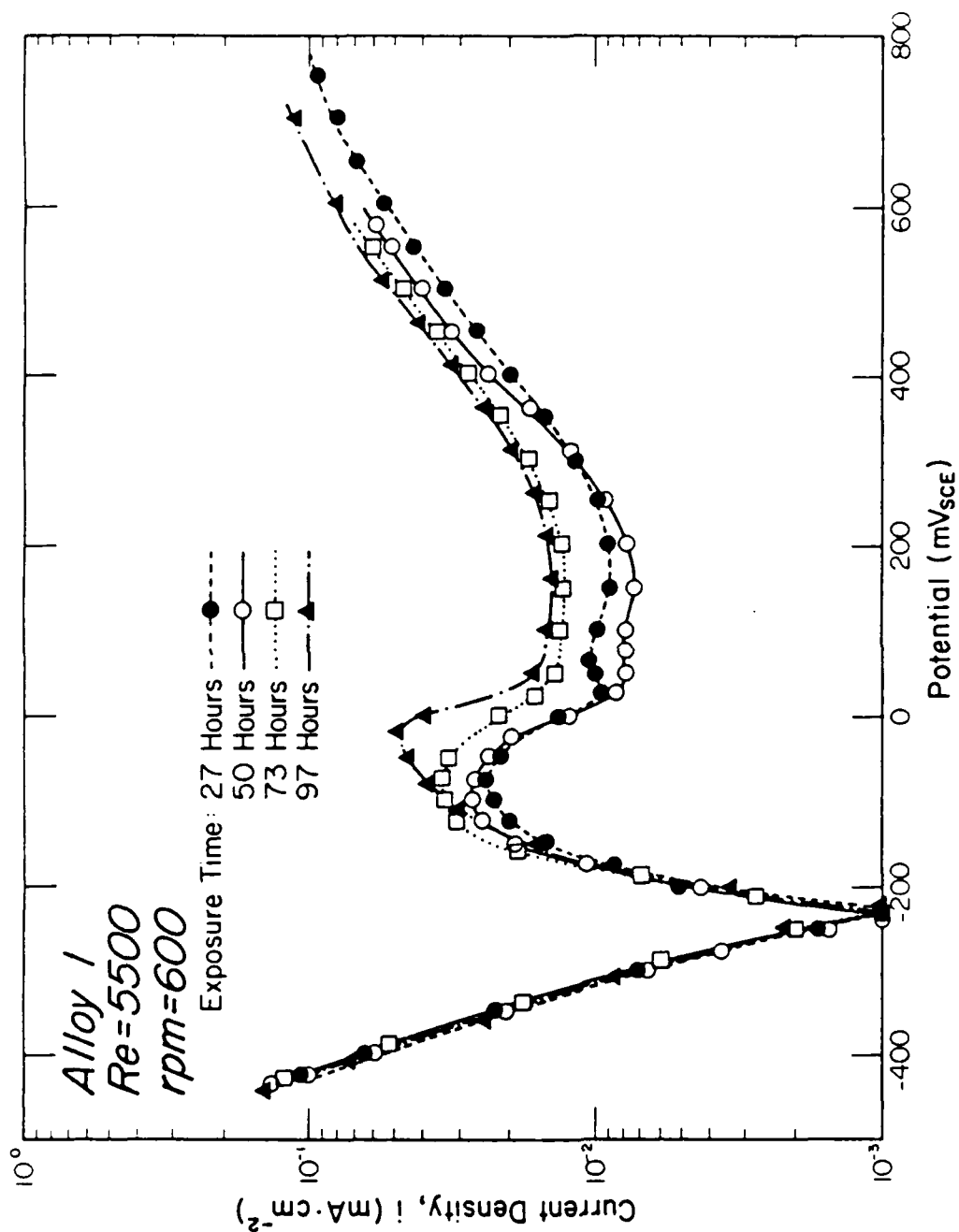


Figure 54: Potentiodynamic polarization curves for Alloy 1 at rpm = 600 at various exposure times.

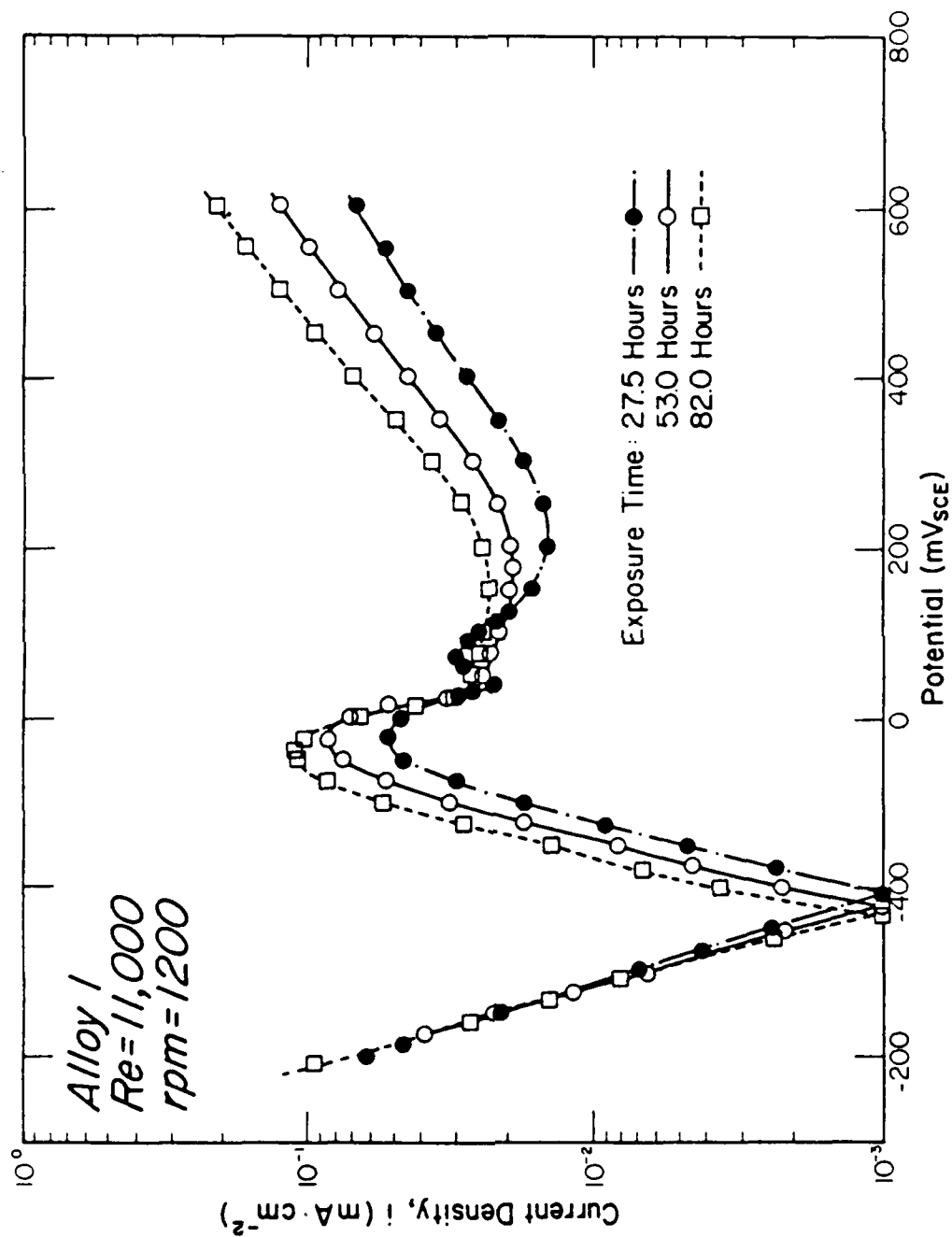


Figure 55: Potentiodynamic polarization curves for Alloy 1 at $\text{rpm} = 1200$ at various exposure times.

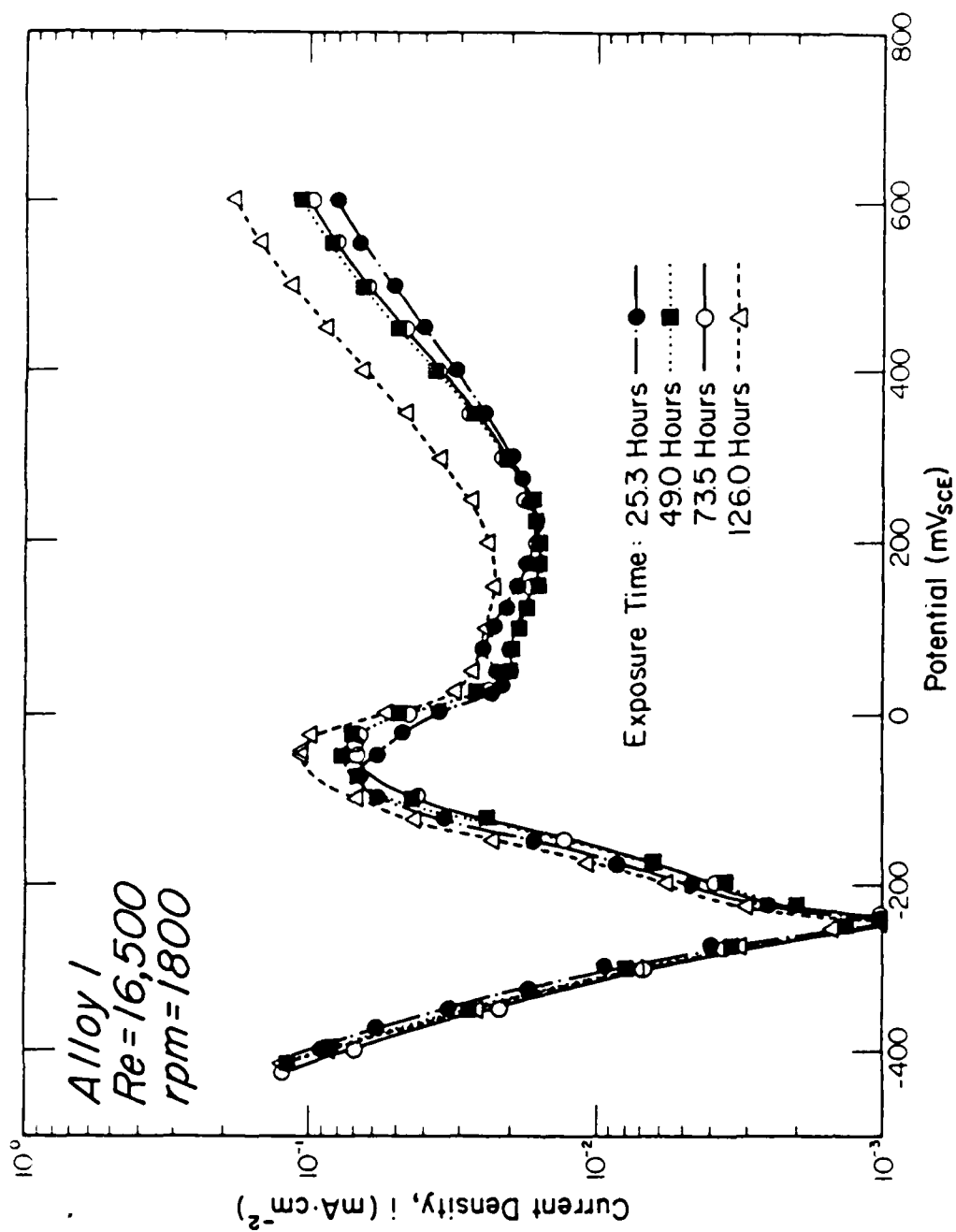


Figure 56: Potentiodynamic polarization curves for Alloy 1 at rpm = 1800 at various exposure times.

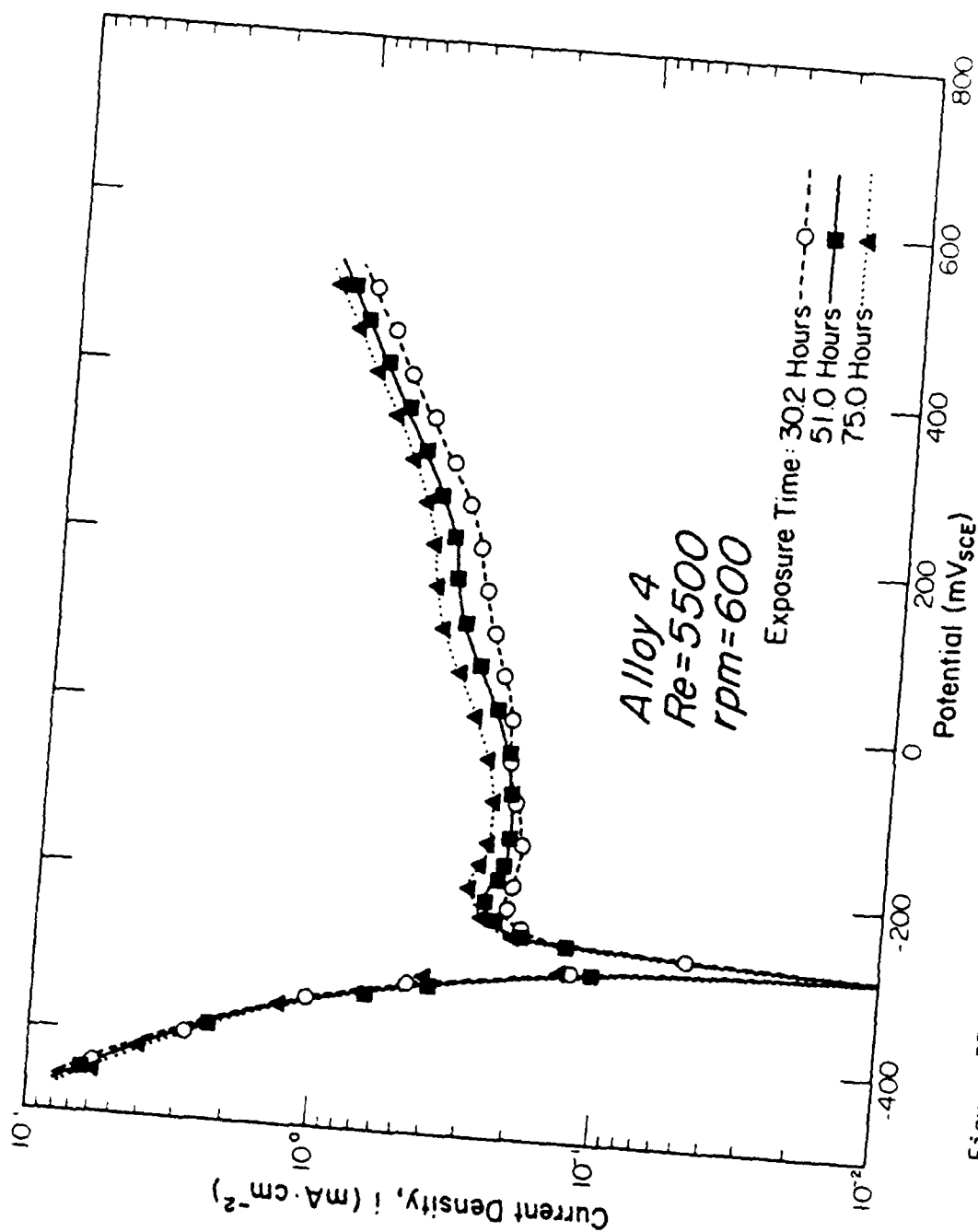


Figure 57: Potentiodynamic polarization curves for Alloy 4 at $rpm = 600$ at various exposure times.

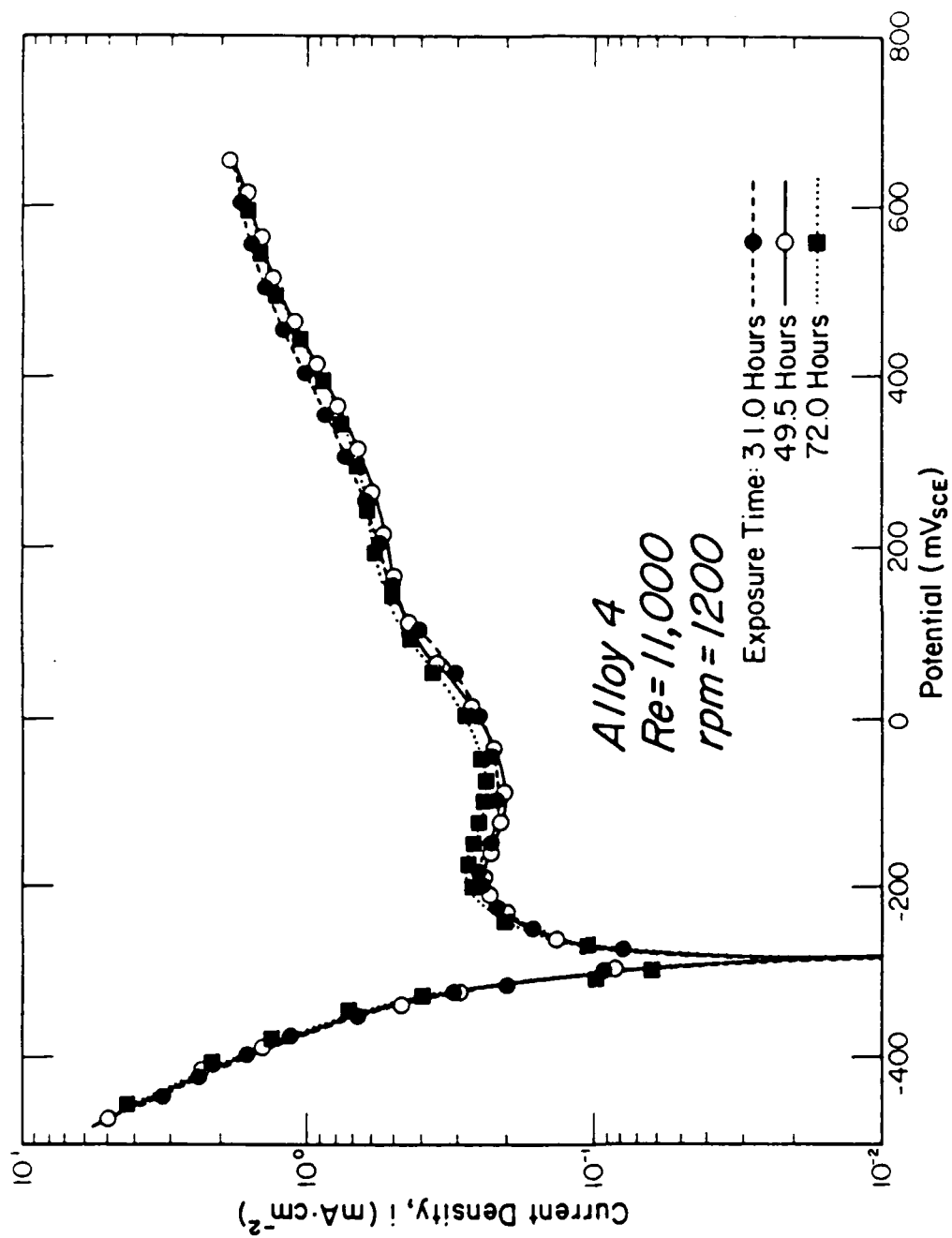


Figure 58: Potentiodynamic polarization curves for Alloy 4 at $rpm = 1200$ at various exposure times.

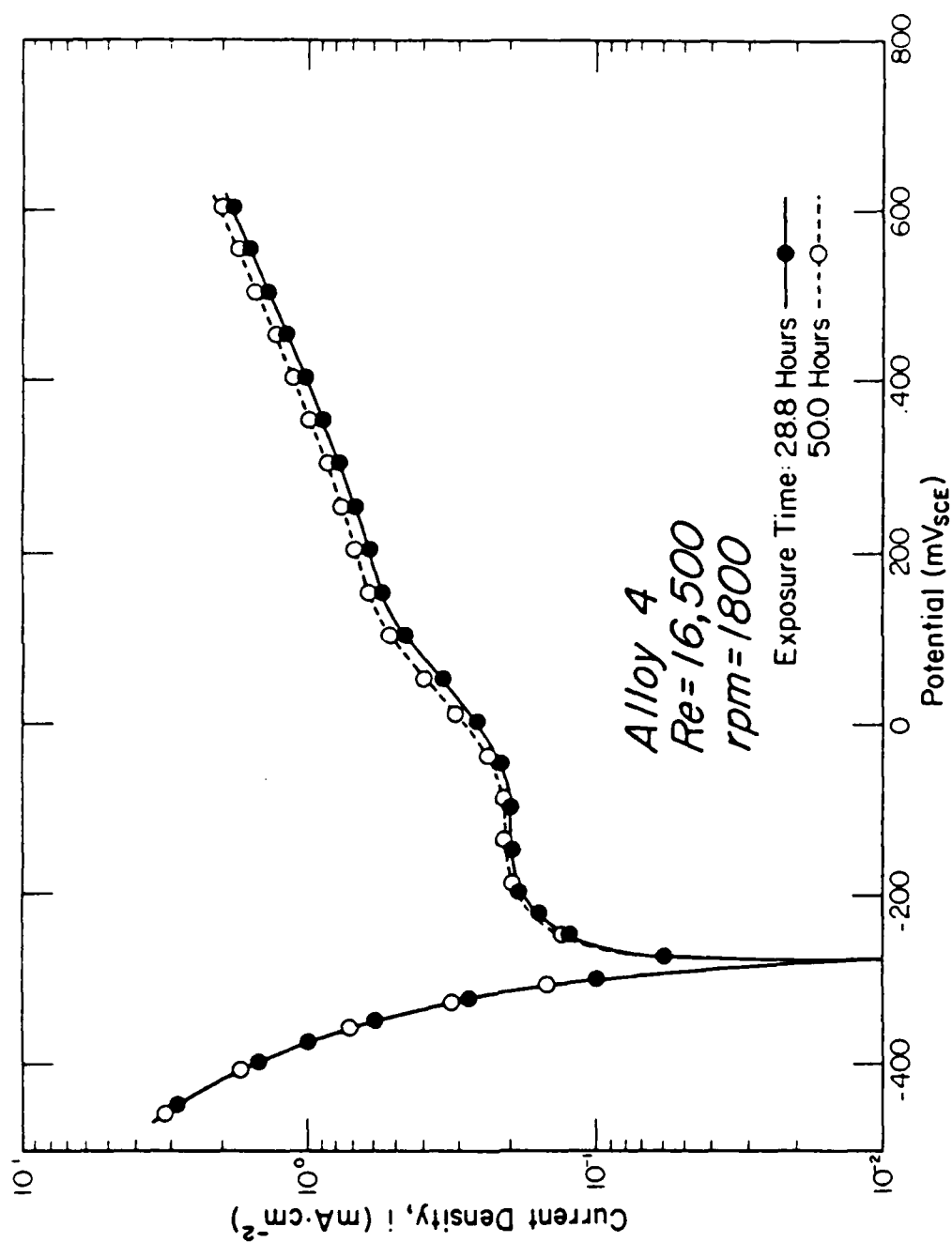


Figure 59: Potentiodynamic polarization curves for Alloy 4 at $rpm = 1800$ at various exposure times.

different exposure times at various rotation speeds for Alloy 1 and Alloy 4, respectively.

For both alloys, the cathodic polarization curves (hydrogen evolution) did not change significantly with exposure time. However, the passive current density in the anodic region increased with increasing time of exposure at all the rotation speeds studied for Alloy 1 while this behavior was observed only at rpm = 600 for Alloy 4. There were no significant changes in the anodic polarization curves with exposure time for Alloy 4 at higher rotating speeds. In addition to this, two peaks of current density in the anodic polarization curves were observed at short time of exposure (about 24 hours) for Alloy 1 at each rotation speed. The second peak (further away from the corrosion potential) disappeared after long exposure times.

It is also found that for each alloy at each rotation speed studied, there exists a critical potential, E_{crit} , beyond which passivation occurred. For Alloy 1, the value of E_{crit} and the current density at E_{crit} increased with increasing rotation speed (or Re) (Fig. 60). For Alloy 4, while the value of E_{crit} increased with increasing rotating speed, the current density at E_{crit} decreased with increasing rotating speed (Fig. 61). For both alloys, the passive current density also tend to increase with increasing Re.

Figures 62 and 63 show a detail look at the potentiodynamic polarization curves in a region of ± 30 mV around the corrosion potential for Alloy 1 and Alloy 4, respectively.

For Alloy 1 (Fig. 62), the cathodic reaction (hydrogen evolution) was depressed by increasing the rotation speed. However, the anodic reaction (alloy dissolution) was enhanced by increasing the rotation speed. This explains the result observed in Fig. 52 (i.e. both the averaged corrosion potential and the averaged corrosion rate decreased with increasing Re) if

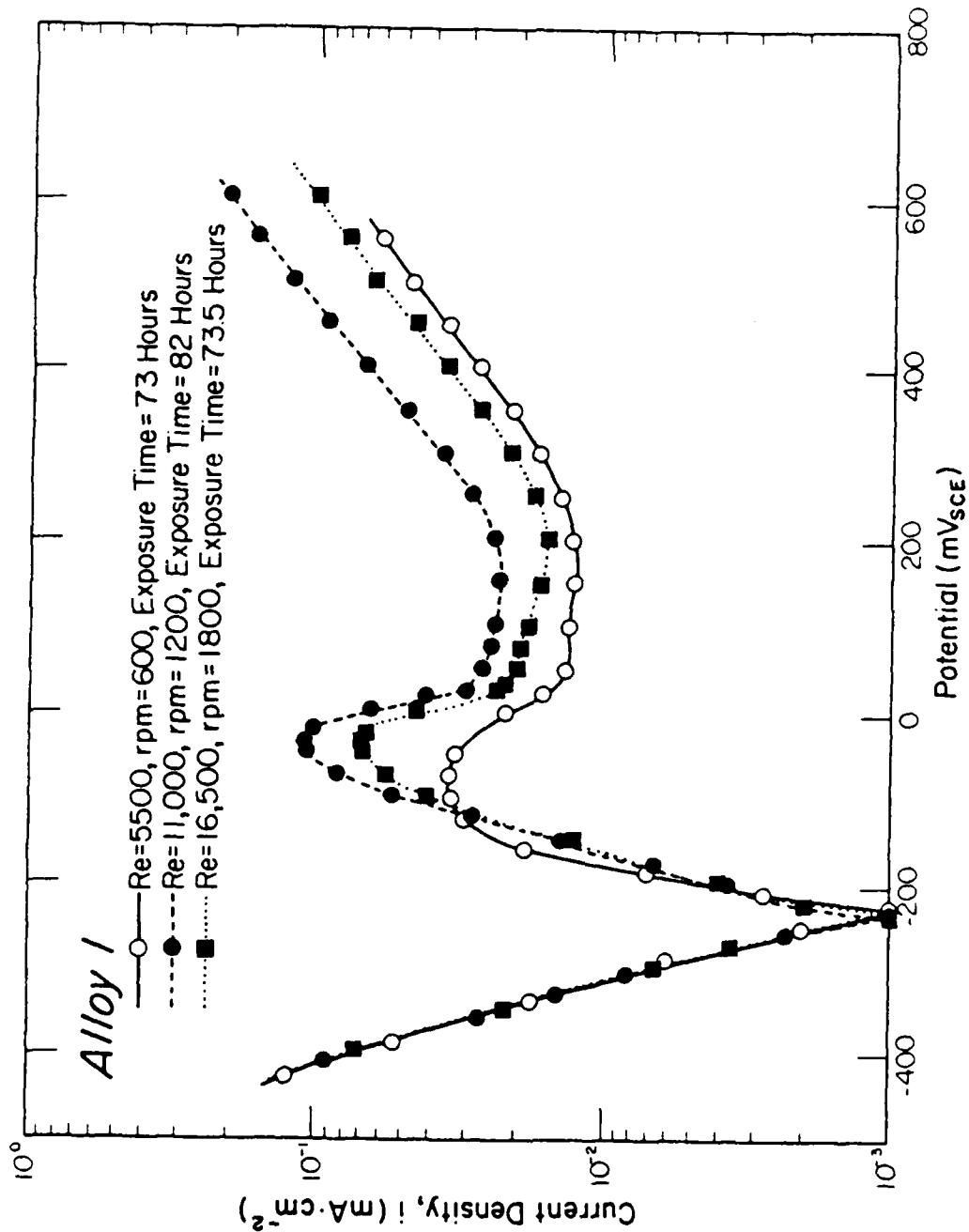


Figure 60: Potentiodynamic polarization curves for Alloy 1 at different rotation speeds.

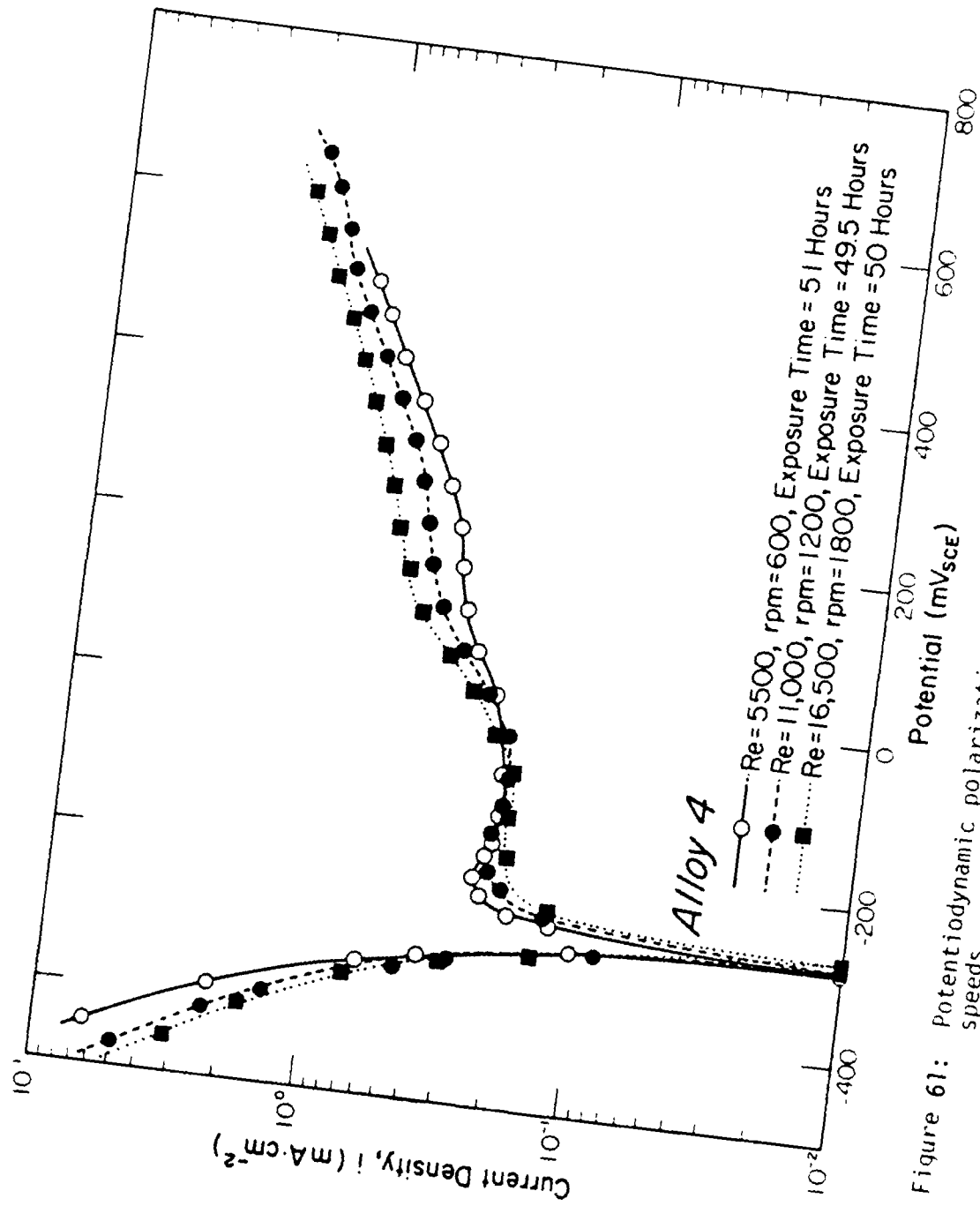


Figure 61: Potentiodynamic polarization curves for Alloy 4 at different rotation speeds.

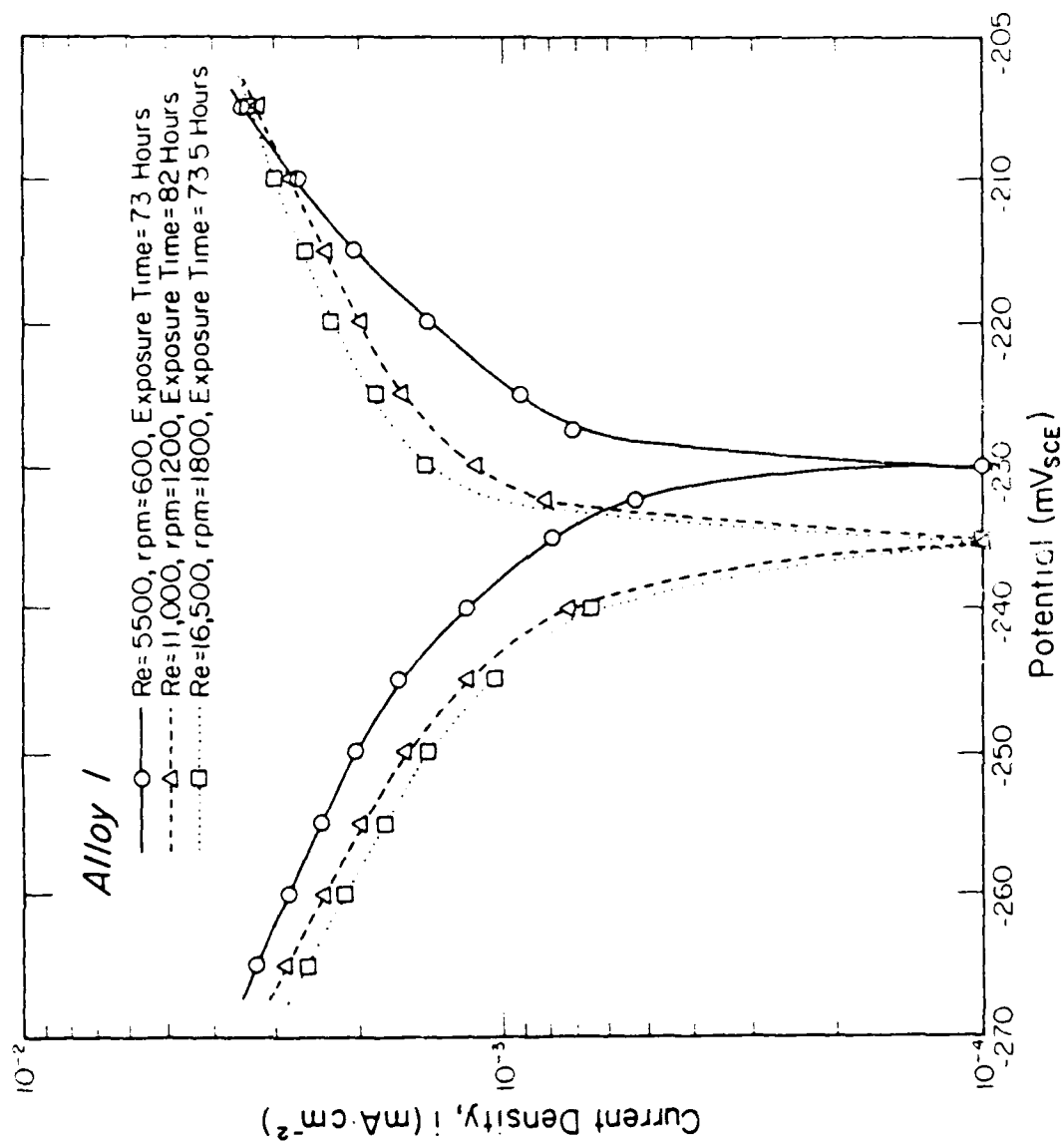


Figure 62: Potentiodynamic polarization curves close to E_{corr} for Alloy 1 at various rotation speeds.

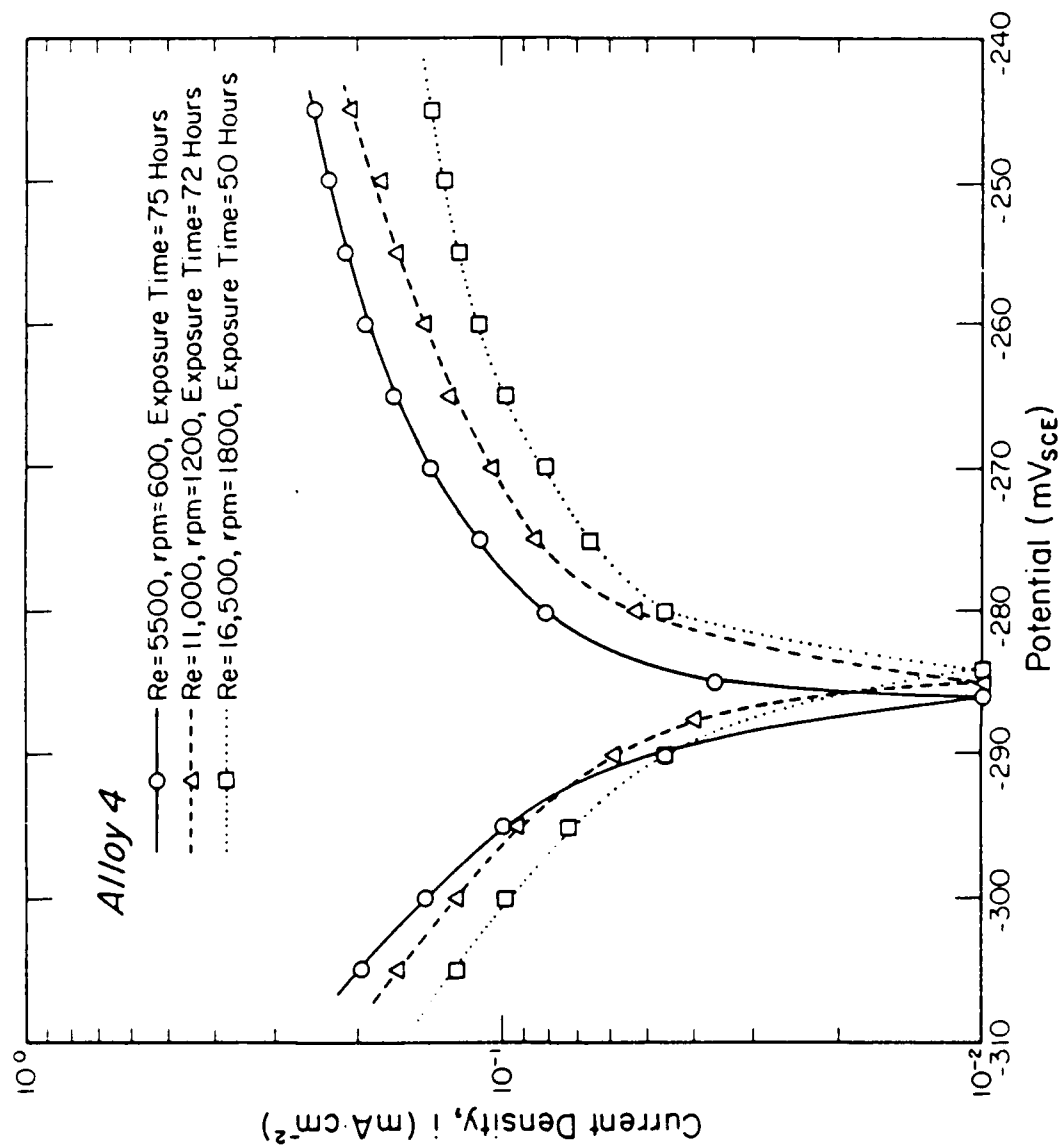


Figure 63: Potentiodynamic polarization curves close to E_{corr} for Alloy 4 at various rotation speeds.

the depression of hydrogen evolution is larger than the enhancement of anodic alloy dissolution. The depression of hydrogen evolution is probably because of the lower effective surface roughness at higher rotation speeds.

For Alloy 4, both the cathodic and the anodic reactions were depressed by increasing rotation speed with the depression higher in the anodic reaction (Fig. 63). This also explains the results observed in Fig. 53 where the averaged corrosion rate decreased and the averaged corrosion potential increased with increasing Re .

Corrosion Rate in Static Solution

An experiment was conducted to evaluate the corrosion rate of Alloy 4 in the same solution under static condition. However, it was found that both the corrosion potential and the corrosion rate increased with increasing exposure time, and no relatively stable corrosion state can be defined up to an exposure time of 72 hours. It was then decided to terminate the corrosion rate measurements under static condition.

Future Works

The Effect of Hydrodynamics on Corrosion

The corrosion rates of Alloy 2 and Alloy 3 will be evaluated in the same solution at $rpm = 600, 1200, \text{ and } 1800$ using SACV and AC impedance techniques.

Surface morphologies of the specimens after exposure will also be studied in the near future using SEM.

Localized Corrosion

Potentiodynamic polarization measurements have been conducted on Alloys 1 and 4 in deaerated 0.1 N HCl , 1.0 N HCl , 5.0 N HCl , and $1 \text{ N HCl} + 4 \text{ N NaCl}$ solutions at $T = 25^\circ\text{C}$ and 50°C . Two potentiostatic experiments were also performed at 400 mV and 650 mV (SCE) for Alloy 1 in 1 N HCl solution at 50°C .

Microscopic examination of the specimen surface showed that the alloys studied under the above conditions are very resistant to pitting corrosion but are susceptible to crevice corrosion. More aggressive solutions will be used to test the pitting corrosion susceptibilities of these microcrystalline alloys at a temperature of 25°C or higher.

Galvanic Corrosion

The susceptibilities of the microcrystalline alloys to galvanic corrosion will also be determined using the rotating cylinder apparatus. In this case, one of the specimens will be fabricated from a conventional alloy (e.g. Type 316 SS). The two specimens will then be coupled via a zero resistance ammeter to evaluate the galvanic corrosion current as a function of rotation speed in deaerated 1 N HCl solution at $T = 25^{\circ}\text{C}$.

Surface Film

In order to understand the corrosion behavior of these microcrystalline alloys, it is necessary to study the surface film formed on the specimen surface using ellipsometry methods, which are available in the department.

VI. SUMMARY AND FUTURE WORK

The mechanical property, oxidation and corrosion data collected to date characterizing the four iron and nickel-based microcrystalline alloys considered in this program support the supposition that these materials offer good combinations of strength and oxidation and corrosion resistance, which should make them attractive materials for a number of intermediate temperature (i.e., 500 to 700°C) applications. Research and characterization work is to continue to more fully characterize the corrosion properties and to evaluate the stress-corrosion cracking tendencies of these materials in aggressive environments.

VII. REFERENCES

1. Bement, A.L. and van Reuth, E.C., "Quo Vadis - RSR", Rapid Solidification Processing, Principles and Technologies, II, Second International Conference on Rapid Solidification, Claitor's Publishing Div., 1980.
2. Tsuru, T. and Latanision, R.M., "Corrosion Resistance of Microcrystalline Stainless Steels", Journal of the Electrochemical Society, Vol 129, No. 7, July 1982, pp. 1402-1408.
3. Ray, R., "Improved Iron-Base Alloys Made Using A Rapid Solidification Process", Third Semi-Annual Report, Contract No. DAAG46-81-C-0062, AMMRC TR 83-16, 1983.
4. Ray, R., Panchanathan, V. and Isserow, S., "Microcrystalline Iron-Base Alloys Made Using a Rapid Solidification Technology", Journal of Metals, Vol 35, No 6., June 1983, pp. 30-36.
5. Ray, R., "Crystallization of Low Metalloid Metallic Glasses - A New Route to Form High Strength Microcrystalline Alloys", Res Mechanica Letters, Vol 1, 1981, pp 261-265.
6. Ray, R., "Bulk Microcrystalline Alloys Prepared from Metallic Glasses - A Novel Materials Technology", Materials Science and Engineering, Vol 52, 1982, p. 85.
7. ASTM Specification E-399, American Society for Testing of Materials, Annual Book of ASTM Standards, 1982, pp. 593-611 and pp. 822-841.
8. Yurek, G.L., Eisen, D., and Garratt-Reed, A., Metall. Trans. A, Vol 13, 1982, p.473.
9. Kofstad, P. and Lillerud, K.P., Journal of the Electrochemical Society, Vol 127, 1980, p. 459.
10. Lillerud, K.P. and Kofstad, P.J., High Temperature Corrosion, R.A. Rapp editor, NACE, Houston, 1983, p. 155.
11. Rizzo, H.F., Boron, J. Kohn, W.F. Nye, and G.K. Gaule, editors, Plenum Press, New York, 1960.
12. Brenner, S.S., Journal of the Electrochemical Society, Vol 102, 1955, p. 16.

13. Caplan, D. and Sproule, G.I., Oxidation of Metals, Vol 9, 1975, p. 459.
14. Lea, C., Metal Science, Vol 35, 1979, p. 301.
15. Lloyd, G.O., Kent, B., Saunders, S.R.J., and Lea, C., Phil. Trans. Roy. Soc., A, 1980, p. 295.
16. Barrett, C.H. and Lowell, C.E., Oxidation of Metals, 11, 1977 p. 199.
17. Rapp, R.A., High Temperature Corrosion, Audio Course, Am. Chem. Soc., Washington, 1980, p. 117.
18. Hoagland, R., Smialowska, S., Rapp, R. and Mobley, C., Stress Corrosion Cracking and Oxidation Characteristics of Boride-Strengthened Microcrystalline Iron and Nickel-Based Alloys", Technical Report No. 1, ONR Report, March 1984.
19. MacDonald, D.D., Journal of the Electrochemical Society, Vol 125, 1978, p.1443.
20. Stern, M. and Geary, A.L., Journal of the Electrochemical Society, Vol 104, 1957, p. 56.

END

FILMED

3-84

DTIC

Cont

AD-A149 805

STRESS CORROSION CRACKING AND OXIDATION CHARACTERISTICS
OF BORIDE-STRENGTH (U) OHIO STATE UNIV RESEARCH
FOUNDATION COLUMBUS C MOBLEY ET AL. 22 OCT 84

9.9

UNCLASSIFIED

OSURF-TR-2 N00014-82-K-0485

F/G 11/6

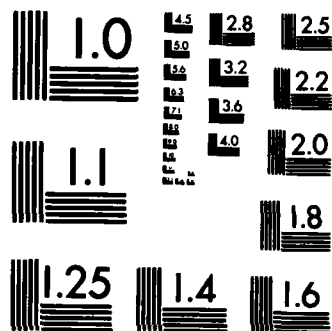
NL

END

FORM

OTK





SUPPLEMENTARY

INFORMATION

Corrected page

AD-A149805

PREFACE

This is the second annual report prepared on Contract Number N00014-82-K-0485, NR-653-014/4-13-82 (430) covering the period or work from July 1, 1983 to June 30, 1984. The program is sponsored by the Department of the Navy, Office of Naval Research. Dr. P. A. Clarkin is the ONR Technical Representative monitoring the program and Morris S. Soloman is the Contracting Officer.

Dr. Carroll Mobley is the Principal Investigator on this study with major research inputs from Drs. Robert Rapp (high temperature oxidation), Richard Hoagland (fracture characteristics and stress corrosion cracking) and Susan Smialowska (corrosion). The Graduate Research Assistants on this program were Mark Straszheim (oxidation), Scott Wade (mechanical properties and fracture characteristics), Hyun-Gyoon Park (mechanical properties and stress-corrosion cracking) and Liberty Chen (corrosion properties). The program is administered and monitored by the Ohio State University Research Foundation and is identified as OSURF Project Number 714640. Dr. Tom Miller was the OSURF Development Officer and Mr. Les Stout is the Principal Administrator on this program.

END

FILMED

9-85

DTIC

